ANALYTICAL APPLICATIONS OF NANOSTRUCTURED PLASMONIC CRYSTALS

BY

AN-PHONG LE

DISSERTATION

Submitted in partial fulfillment of the requirements
for the degree of Doctor of Philosophy in Chemistry
in the Graduate College of the
University of Illinois at Urbana-Champaign, 2011

Urbana, Illinois

Doctoral Committee:

Professor Ralph G. Nuzzo, Chair
Professor Catherine J. Murphy
Professor John A. Rogers
Professor Jonathan V. Sweedler

ABSTRACT

Surface plasmon resonances (SPR) have been exploited through various means for the realization of label-free, surface-sensitive chemical analysis and imaging, all of which rely on the interactions between the local environment and the evanescent electric fields generated by the surface plasmons at the metal-dielectric interface. Plasmonic crystals are a versatile platform for the tunable coupling of light into surface plasmon modes, and soft nanoimprint lithography represents a class of fabrication techniques capable of inexpensive, high fidelity replication of nanoscale features over large areas; these methods are well-matched for surface-enhanced sensing applications whose performance depends strongly on these fabrication characteristics. The work presented in this dissertation focused on the development of new surface-enhanced Raman spectroscopy and surface plasmon resonance imaging modalities based on this nanostructured plasmonic crystal platform. Nanostructured plasmonic crystals were patterned onto the tips of silica optical fibers using a soft embossing method for use as single-fiber SERS optrodes, and enhanced Raman scattering was observed for benzenethiol monolayers adsorbed onto the structured fiber tip as well as for Rhodamine 6G dissolved in aqueous solution. The inherent versatility of this plasmonic platform for SERS-based sensing was demonstrated through the effective Raman enhancements obtained in markedly different refractive index environments. Nanoimprinted plasmonic crystals were also adapted for reflection imaging studies of thin films deposited onto the metal surface. Normalized contrast metrics were developed based on reflection images of polyelectrolyte layer-by-layer assemblies acquired using bandpass filters to restrict the accessible wavelength ranges and quantitatively calibrated to the surface film thickness. As a model system, *Aplysia* pedal neurons were cultured on the

plasmonic crystal surface, and the thicknesses of neuronal processes were quantitated using the calibrations derived for this reflection imaging protocol using common laboratory equipment: a reflection microscope, commercially available bandpass filters, and a digital camera. The imaging-based measurements of neuronal process thickness were verified independently using atomic force microscopy with excellent agreement between the two methods. The applications explored in this dissertation demonstrate the broader utility of nanoimprinted plasmonic crystals for chemical sensing and imaging.

For my grandparents

ACKNOWLEDGMENTS

I would like to begin by thanking my thesis adviser, Prof. Ralph Nuzzo, for his support and guidance during my transformation as a scholar. Perhaps the most sincere gratitude I can offer is that as a result of his guidance, influence, and encouragement, I move forward now with an interest in continuing 'hard' scientific research as part of my future career. The trust he has placed in me has given me confidence to try new, interesting ideas; the expectations and standards that he has held me to have made me a better scientist.

I would also like to thank Prof. John Rogers for his guidance and support, especially during the early stages of my graduate work, and I would like to express my appreciation to Prof. Jonathan Sweedler, Prof. Andrew Gewirth, and Prof. Catherine Murphy for serving on my preliminary examination and final defense committees and for their guidance, input, and encouragement.

I would know nothing right now were it not for the help and the patience of Jimin Yao, Tu Truong, Joana Maria, Alfred Baca, Matthew Stewart, Matthew Schulmerich, Lucas Thompson, and Stanislav Rubakhin. Their support and friendship cannot be adequately described in words, and I am grateful to all of them for their contributions to these projects and to my own success. I would also like to thank the other members of the Nuzzo group, both past and present, for their support and generosity. Their senses of humor helped buoy my spirits through periods of frustration, and it has been a delight to watch their accomplishments and their successes. I wish them all the very best of luck in all of their future endeavors, but their talents will assuredly lead them to great accomplishments.

I would like to thank Dr. Stephen Gray at Argonne National Laboratory and Dr.Tae-Woo Lee at Louisiana State University for their guidance and assistance with the computational simulations of these plasmonic crystals. I am also grateful for the assistance provided by the staff of the MRL Central Facilities, and Julio Soares and Bharat Sankaran in particular, for the fabrication and characterization of the plasmonic devices in this work as well as for their guidance when things went awry.

I am indebted to Dr. Steven Zumdahl for the chance to teach introductory chemistry students as an undergraduate, an experience that ultimately set me on my current path. I have had the unbelievably good fortune to work with Prof. Paul Kelter, Dr. Don DeCoste, and the other faculty and staff in General Chemistry at the University of Illinois, If others judge us by the company we keep, then I have certainly chosen that company wisely; they all embody a passion and a talent for teaching that is continuously demonstrated, and I am grateful to have had the opportunity to see them in action. Someday, I hope to someday be as good a teacher as they have been to me.

Last on this list, but first among equals: I am eternally grateful to my parents, my sister, and Kaitlin for their love and support throughout my studies and for their understanding when things sometimes took longer than I had anticipated. I love them all dearly, and without them, I would be but a shell of who I am today. I hope that what little I have accomplished here and what I may achieve in the future is worthy of their affection and confidence in me.

It has been said (by individuals of much greater renown than me) that if we have succeeded at seeing a bit further, it is the result of standing on the shoulders of giants. With regards to the work presented in this dissertation and to my graduate school experiences in general, no statement could be more fitting. To a large extent, my accomplishments are not truly

my own; they are the result of what little I have been able to see a bit further while supported by the assistance and guidance that I have received along the way. Without the patience, wisdom, and guidance of my mentors, collaborators, coworkers, family, and friends, none of this would have been possible. A few sentences on a sheet of paper are woefully inadequate to truly express my heartfelt gratitude for their generosity of time, spirit, and understanding.

TABLE OF CONTENTS

CHAPTER 1

Functional Nanoimprinted Plasmonic Crystals for Chemical Sensing and Imaging

Note: The majority of the text and figures in this chapter are reproduced with permission from the previously published paper: J. Yao, A.-P. Le, S. K. Gray, J. S. Moore, J. A. Rogers, and R. G. Nuzzo, "Functional Nanostructured Plasmonic Materials", *Adv. Mater*. 2010, 22, 1102-1110 (Copyright 2010, WILEY-VCH Verlag GmbH & Co. KGaA) and from a chapter co-authored by S. K. Gray, R. G. Nuzzo, and J. A. Rogers and accepted for publication in a book entitled *Nanoplasmonic Sensors*, edited by Alexander Dmitriev, to be published by Springer.

1.1 Overview of Dissertation

This dissertation describes sensing and imaging applications for nanostructured plasmonic crystals consisting of square arrays of nanoholes fabricated using a soft nanoimprint lithography technique. This technique is capable of rapidly and inexpensively replicating nanoscale features over large areas with high fidelity, all of which are important considerations for future sensing applications. The grating structure formed by the nanoholes allows for the coupling of light to surface plasmon modes, both surface plasmon polariton modes which propagate along the gold film as well as localized surface plasmon resonances around the rims of the nanoholes. The sensing and imaging applications described in this work both exploit the

evanescent electric fields generated by these surface plasmon modes, albeit in two different contexts.

Chapter 2 describes work on integrating nanoimprinted plasmonic crystals on the tips of silica optical fibers for use as surface-enhanced Raman scattering probes. The advantages of optical fiber based probes for SERS include simplified optical and instrumental configurations as well as versatility in sampling arrangements. Soft embossing provides an inexpensive and versatile method to pattern deterministic nanostructures on the tips of optical fibers, especially compared to alternative methods such as electron-beam lithography or focused ion beam milling. The integration of these plasmonic crystals with optical fibers creates a probe capable of enhancing the Raman signal of analytes in both air and in water, with benezenethiol monolayers and aqueous Rhodamine 6G solutions examined as test cases. These probes exhibit sufficient Raman enhancements as to overcome the inherent Raman scattering from the optical fiber substrate; this background scattering has previously been an impediment to the development of optical fiber based Raman systems and has driven the incorporation of significant engineering workarounds to mitigate its impact. Alternative methods to remove the silica Raman background as well as to incorporate it as an internal standard for comparisons between spectra were introduced in order to demonstrate both the feasibility as well as the simplicity of this single SERS fiber arrangement. The results from this work demonstrate the versatility of nanostructured optical fiber probes fabricated by soft lithography as a general platform for SERS-based sensing.

Chapter 3 describes the development of a reflection imaging technique capable of quantitatively determining the thickness of thin films present on the surface of a nanostructured plasmonic crystal. Systematically grown thin films of polyelectrolytes imaged through bandpass

filters were used as a model system for a normalized reflection contrast which was developed as part of this work with specific surface film thicknesses. Refractive index corrected layer thicknesses were derived from the polyelectrolyte thicknesses using ellipsometric modeling and verified computationally using an implementation of the finite-difference time-domain method. As a test system, *Aplysia californica* pedal neurons were cultured directly on the plasmonic crystal surface, and the index corrected thicknesses for the neuronal processes extended by the cultured neurons were quantitated from the image contrasts. Use of bandpass filters allowed for wavelength dependent optical phenomena to be explicitly incorporated into the imaging calibrations, resulting in greater imaging contrast and sensitivity. Imaging-based thickness estimates were verified independently using atomic force microscopy with excellent agreement between the two methods. Using a plasmonic crystal, a basic optical microscope, commercially available bandpass filters, and a digital camera, this reflection imaging technique is capable of quantitative thickness measurements in near-real time with sufficient precision to complement the use of atomic force microscopes for surface profiling within the plasmonic sensing volume (up to ~100 nm from the plasmonic crystal surface).

1.2 Introduction to Surface Plasmon Resonance and Plasmonic Nanostructure Fabrication

Surface plasmons are resonant oscillations of conduction electrons at the metal-dielectric interface excited by the coupling of incoming electromagnetic radiation to the metal surface which gives rise to an evanescent electric field that extends from the metal surface a few hundreds of nanometers into the surrounding medium.[1-4] Even small changes in the dielectric material's refractive index can generate large changes in the resonance conditions of these

surface plasmons. This combination of refractive index sensitivity and a small sensing volume has attracted great interest in the application of surface plasmon resonance for label-free chemical sensing applications.[5,6] Indeed, surface plasmon resonance sensors are commonly used to quantitatively detect both chemical and biological analytes in their native state, side-stepping potential concerns related to the inclusion of fluorescent or radioactive labels.

Traditional surface plasmon resonance (SPR) sensors use flat metal films (typically gold) to generate surface plasmon polaritons which can propagate tens to hundreds of microns along the metal-dielectric interface.[7-9] The surface plasmon polaritons can be excited by the coupling of light into the metal film, but this coupling is subject to momentum-matching conditions between the photon and surface plasmon polariton mode. The dispersion relation for a surface plasmon polariton (k_{SP}) propagating along a planar metal-dielectric interface is given by Equation 1 below:

$$k_{SP} = \frac{\omega}{c}\sqrt{\frac{\varepsilon_M \cdot \varepsilon_D}{\varepsilon_M + \varepsilon_D}} \qquad (1)$$

where ω is the frequency of the surface plasmon polariton, c is the speed of light, ε_M is the dielectric constant of the metal, and ε_D is the dielectric constant of the surrounding dielectric environment.[3] The momentum of a photon in air is generally less than that of the surface plasmon polariton, and an external mechanism is required to compensate for this momentum mismatch.

One method to compensate for the mismatch between the momentum of a photon and that of the surface plasmon polariton is to couple light into the metal film at an angle using a prism in the Kretschmann configuration, which excites a single surface plasmon resonance in the metal film based on the principle of total internal reflection.[10-12] This resonance is identified by a

minimum in the spectrum of light reflected from the metal film, and changes in the refractive index of the local environment result in changes in the position and magnitude of this reflectance minimum; these changes in resonance conditions can thus be used for refractive index sensing at the metal-dielectric interface. Although the resulting data are relatively easy to interpret, the physical equipment can be cumbersome (with Kretschmann configuration systems generally requiring a prism, polarizers, lenses, and rotation stages capable of precise alignment) and difficult to integrate with other systems for low-cost or high-throughput detection schemes.[13]

The diffraction of light in one-dimensional or two-dimensional metal grating structures can also be used to compensate for the momentum mismatch between the surface plasmon polariton and the photon.[14,15] These diffraction effects result in the addition of multiples of the grating momentum to that of the incident photon and can couple a photon into a surface plasmon polariton mode provided the momentum conservation relation is satisfied:

$$k_{SP} = k_P \pm iG_x (\pm jG_y) \qquad (2)$$

where k_{SP} is the wave vector of the surface plasmon polariton mode, k_P is the wave vector of the incident photon, G_x (and G_y) are the Bragg vectors associated with the periodicity of the grating in one (or two) dimensions, and i and j represent the scattering event order. This momentum conservation relation potentially allows for the coupling of photons to several different surface plasmon polariton modes (with the appropriate grating spacings and scattering orders), and the surface plasmon polariton behavior in grating-based systems is indeed more complex than that found using prism-coupling systems.

Metal grating-based and metal nanoparticle-based systems can give rise to localized surface plasmon resonances (LSPRs) in which the surface plasmon is confined within or around the nanostructure.[4,15-18] In contrast to propagating surface plasmon polaritons, these LSPRs can

be used to make measurements of the local refractive index with higher spatial resolution. These nanostructured metals can efficiently couple light into surface plasmons with simpler optics, making them more amenable for lower cost devices. The electric field intensity of LSPRs can be higher than that of SPPs and can be tuned through control of the nanostructure shape, size, composition, and assembly; these characteristics have generated interest in the use of these substrates for other surface-enhanced spectroscopy techniques such as surface-enhanced Raman scattering (SERS) and surface-enhanced fluorescence.[19-29] Raman signal enhancements upwards of 10^{10} for a single molecule have been reported, providing chemically specific information without the need for additional labels with great sensitivity.[20,30-35]

The widespread application of surface-enhanced spectroscopies in general has been limited by the poor reproducibility of the substrates that give rise to the surface enhancement itself.[20] Production techniques for these substrates would ideally generate highly uniform structures over large areas at low cost. Photolithography and thin-film processing techniques can be used to fabricate large areas of high quality nanostructures but at relatively high cost. Electron beam lithography and focused ion beam lithography are capable of creating a diverse array of nanostructures including holes[36,37], grooves[38], slits[39], and nanoparticles[40,41] with high reproducibility and fine control over structures' dimensions, but they are not easily scaled to large areas or high production rates.

Recent reports describe the use of soft interference lithography to create plasmonic nanostructures over large areas.[42-45] An elastomeric stamp is cast from a lithographically defined master and is used as a phase mask for phase-shifting photolithography. Subsequent metal deposition and etching steps can create both nanoparticles and free-standing nanostructured

metal films with centimeter-scale areas. However, these substrates come at come at the expense of higher cost and processing complexity.

The use of close-packed nanospheres as a deposition template allows the formation of continuously structured metal-film-over-nanosphere structures which have generated very high SERS enhancement factors.[46-48] The close-packed nanosphere layer can also be used as a deposition mask to selectively allow metal nanoparticles to be deposited onto a substrate with high size and spatial control. These surface-assembled dielectric nanosphere arrays have also been combined with electrochemical metal deposition (such as gold, palladium, or platinum) to create structured plasmonic films of controlled thickness and feature sizes for use as SERS substrates.[49-51] These nanosphere lithography techniques can generate defect-free nanostructures over areas of 10-100 μm^2.[52] The use of larger colloidal spheres adsorbed onto a surface has been used to generate different structures including rings and crescents, but these nanostructures are generally more randomly distributed.[53-55]

Soft nanoimprint lithography addresses the need for a relatively low cost fabrication technique that can generate high quality, high resolution, uniform nanostructures over large areas.[4,56-58] Relatively simple changes in the fabrication process of these nanoimprinted plasmonic crystals can greatly shift the spectral sensitivity of the devices which can be harnessed for surface plasmon resonance spectroscopy and imaging. These plasmonic crystals can quantitatively detect binding events at even submonolayer levels, comparable to the sensitivity of more conventional SPR devices.[4] Their applications extend from bulk refractive index sensing via SPR spectroscopy to thin film imaging using SPR and SERS with micrometer-scale lateral resolution over square millimeter areas. [4,24,59-62] The fabrication and demonstrated applications of these nanoimprinted plasmonic crystals are herein discussed.

1.3 Soft Nanoimprint Lithography for the Facile Production of Plasmonic Crystals

A generalized summary of nanoimprint lithography for the production of plasmonic crystals is depicted in Figure 1.1.[4,24,57,59,60] A master consisting of a square array of holes is created in a photoresist (PR) layer on silicon from which an elastomeric stamp is cast. To replicate the nanohole array, a composite poly(dimethylsiloxane) (PDMS) stamp is cast,[63-66] resulting in a stamp with the inverse of the original hole structure. To create a nanopost array from the nanohole master, an intermediate casting step is used where an acryloxy perfluoropolyether (a-PFPE) stamp is cast from the lithographically defined master. The a-PFPE layer is backed by a poly(ethylene terephthalate) film for mechanical support and is then used to cast a PDMS stamp which has the same nanohole structure as the photoresist master.[60,67] The stamp material is not limited to PDMS – as evidenced in the production of the nanopost array stamp, other materials with low surface energy and good chemical compatibility can be used.[67-70]

The PDMS stamp is then pressed into a layer of photocurable polyurethane cast onto a glass slide and exposed to ultraviolet light to generate either a nanohole or nanopost array, depending on the particular stamp used. This technique is not limited to polyurethanes - other molding materials are possible (such as an epoxy-type SU-8 photoresist precursor).[24,60,67] After curing, the nanoimprinted array is metalized (typically with gold) to complete the plasmonic crystal. Although the original photoresist master is initially produced via a photolithography process, the expense of initial fabrication is mitigated by the PDMS stamp production itself. Several PDMS stamps can be cast from the same photoresist master, and each PDMS stamp can then be reused to produce many replicas.

Figure 1.2a and Figure 1.2b show scanning electron microscope (SEM) images and cross-section insets for the nanopost and nanohole arrays respectively, and Figure 1.2c and Figure 1.2d show atomic force microscope (AFM) maps and line cuts for the same nanopost and nanohole arrays respectively.[60] Both the SEM and AFM images show that the nanoimprinted features are precisely replicated across lengths of tens of microns with high spatial uniformity. Figure 1.3a shows an optical image of a nanohole plasmonic crystal with 16 arrays (4 mm on a side) varying in periodicity from 0.5 μm (hole diameter = 0.24 μm) to 1.74 μm (hole diameter = 1.06 μm). Diffraction of light from the grating arrays gives rise to the different colorations, and the uniform color across each array shows that the nanostructure pattern is in fact highly uniform across the entire millimeter-scale area. Spectroscopic measurements confirm this uniformity:[71] Figure 1.3b shows transmission spectra collected at five different areas within a single nanohole array, and the nearly identical spectra demonstrate the high nanostructure fidelity across the entire plasmonic crystal. Figure 1.3c shows transmission spectra for four different plasmonic crystal samples and shows that the optical properties remain consistent between samples.

Although the feature sizes replicated in these plasmonic crystals are relatively large, the ultimate resolution of soft nanoimprint lithography can be much smaller with the proper choice of stamp and molding materials. An a-PFPE stamp cast from a master consisting of single walled carbon nanotubes on a silicon substrate successfully replicated those features in a layer of photocurable polyurethane with lateral resolutions approaching ~1 nm.[64,67] Moreover, the fabrication steps required to achieve this resolution were not markedly different from the procedure described above, demonstrating that soft nanoimprint lithography is indeed capable of high resolution feature replication over large areas.

The design rules for these plasmonic crystals include not only the geometry (post or well) and nanostructure dimensions (diameter, depth or height, and spacing between the holes or posts) but also the thickness and distribution of the gold layer that supports the surface plasmons. Electron-beam evaporation of gold onto the plasmonic crystal results in a directional coating of gold on the top surface of the plasmonic crystal as well as the formation of gold disks at the bottom of the nanowells.[4] The gold distribution in these devices is discontinuous (although small grains of gold may appear on the sidewalls of the nanoholes) and have been termed a "quasi-3D" plasmonic crystal. Figure 1.4a shows a SEM image of a quasi-3D nanohole plasmonic crystal, and the inset image shows a lack of metal on the nanohole sidewall. In contrast, sputtering of gold onto the plasmonic crystal results in a continuous, conformal coating of gold along the top, bottom, and sidewall surfaces which are referred to as "full 3D" plasmonic crystals.[59,61] Figure 1.4b shows a SEM image of one of these structures along with a cross-section inset showing the continuous gold layer on all of the nanohole surfaces. The distribution of gold in these plasmonic crystals exerts great influence over their optical properties and sensitivities for sensing applications.

1.4 Bulk Refractive Index Sensing Using Quasi-3D and Full-3D Plasmonic Crystals

The surface plasmon resonance modes supported by these nanoimprinted plasmonic crystals exhibit great sensitivity to changes in the local refractive index and have been applied as refractive index sensors. The plasmonic crystals are mounted in a flow cell through which aqueous solutions of poly(ethylene glycol) (PEG) of varying concentration and refractive index are introduced.[4,59,60] The flow cell itself is mounted in a spectrophotometer, allowing the time resolved measurement of transmission through the plasmonic crystal.

Figure 1.5a shows a map of the change in transmission as a function of wavelength and time as aqueous solutions of poly(ethylene glycol) (PEG) with different refractive indices are flowed past a quasi 3D plasmonic crystal.[4] The reference condition in these experiments was the initial transmission when water is flowed past the plasmonic crystal. Figure 1.5b shows a simplified version of the data presented in Figure 1.5a where the time resolved transmission change is plotted for four individual wavelengths. The data clearly show a change in transmission when the refractive index of the solution is changed as well as a return to the initial transmission when the aqueous PEG solution is replaced with water.

SPR refractive index measurements often report the change in wavelength or intensity for a single surface plasmon resonance supported by the plasmonic device. However, the data in Figure 1.5 and Figure 1.5b clearly show wavelengths where the transmission increases (1033 and 1187 nm) while other wavelengths show decreases (1071 and 1126 nm). Furthermore, Figure 1.5a reveals transmission changes that vary across different wavelengths. We have developed a multispectral analysis to account for these changes in transmission over all wavelengths. The absolute value of the change in transmission relative to the reference transmission at time t=0 is calculated at each wavelength. These absolute changes are then integrated across the entire wavelength range to determine an integrated response. The integrated response is then plotted against the change in refractive index, and the slope of the regression line is used as the figure of merit for this multispectral analysis. A larger figure of merit corresponds to a larger change in the integrated response for a given refractive index change, akin to the peak wavelength shift or reflectance change reported in conventional single resonance SPR measurements.[7]

Figure 1.6a and Figure 1.6b show transmission difference maps for a quasi 3D plasmonic crystal and a full 3D plasmonic crystal respectively.[4,59,71] The quasi 3D difference map shows

the grates changes at near-infrared wavelengths, while the full 3D difference map shows larger transmission changes throughout the measured spectrum. This is borne out in the integrated response and figure of merit calculations shown in Figure 1.6c and Figure 1.6d for the quasi 3D and full 3D cases respectively. The integrated responses of the full 3D plasmonic crystal are approximately twice as large as those of the quasi 3D plasmonic crystal with a figure of merit also approximately twice as large. Furthermore, the sensitivity of the full 3D plasmonic crystal is more than three times greater than that of the quasi 3D system when the analysis is restricted to wavelengths between 350 – 1000 nm (as shown in red in Figure 1.6c and Figure 1.6d).

We have conducted bulk refractive index sensitivity measurements using the nanopost arrays in a similar manner.[60] Gold was sputtered onto both the nanopost and nanowell, yielding continuous conformal metal films on the relief structures. In calculating the integrated responses for the nanopost and the full 3D nanohole arrays in this experiment, an additional step was introduced to normalize the absolute transmission change at each wavelength to the initial transmission at time t=0. This change has the effect of giving greater weight to changes where the initial transmission is smaller. Figure 1.7 presents these normalized transmission differences for a nanopost (Figure 1.7a and Figure 1.7c) and a full 3D nanohole (Figure 1.7b and Figure 1.7d) array. The nanopost array exhibited ~70% greater sensitivity to bulk refractive index changes than the nanowell array, with much of the increase in sensitivity coming at wavelengths between 700 – 800 nm.

The linear change in integrated response to refractive index change of these plasmonic crystals is advantageous for their use in quantitative sensing and imaging. Each structure demonstrated sensitivity at different wavelengths spanning the visible and near-infrared wavelengths. Furthermore, the signal-to-noise ratio of the integrated response is greater than that

associated with examinations of single wavelengths, improving the precision of these plasmonic crystals compared to other SPR based measurements.[4,59]

1.5 Theoretical Modeling of Plasmonic Crystal Resonances

The design rules of these nanoimprinted nanohole and nanopost plasmonic crystals undoubtedly control not only the overall sensitivity of the devices but the spectral regions in which that sensitivity is greatest. Thus, a rational approach to altering those design rules must include the ability to understand and to model the underlying physics present. The plasmonic Brillouin zone of a quasi 3D nanohole array has been mapped using angle dependent transmission measurements.[57] Additionally, the highly uniform nanostructures make these plasmonic crystals amenable to computational modeling using the finite-difference time-domain method.[4,59-61,72]

1.5.1 Plasmonic Brillouin Zone Mapping

Surface plasmon polaritons can be considered as propagating oscillations of the conduction electrons at the metal-dielectric interface. Because these oscillations travel across the periodic nanohole or nanopost arrays in these plasmonic crystals, a plasmonic Brillouin zone (PBZ) should exist that fully characterizes their behavior across the entire surface. Zero-order transmission data were collected for a quasi 3D nanohole plasmonic crystal as it was rotated around two axes, and the appropriate mathematical transformations result in the plasmonic Brillouin zone map presented in Figure 1.8a.[15,57,73,74] The flat blue regions in the lower corners of Figure 1.8a correspond to angles that were not accessible in this experimental setup.

To provide insight into the PBZ, lines have been overlaid on the diagram using the surface plasmon polaritons dispersion relation for a flat metal-dielectric interface:

$$k_{SPP} = \frac{\omega}{c}\sqrt{\frac{\varepsilon_d \cdot \varepsilon_m}{\varepsilon_d + \varepsilon_m}}$$

where k_{SPP} and ω are the respective momentum and frequency of the surface plasmon polaritons, c is the speed of light, and ε_d and ε_m are the respective dielectric constants of the dielectric and metal. The plotted SPP dispersion curves overlay well with some ridges of higher transmission in the PBZ map, although other areas of increased transmission are not fully described by this simpler model.

Following the initial PBZ mapping of the quasi 3D nanohole array, a self-assembled monolayer (SAM) of 1-hexadecanethiol was formed on the gold surface and similar angle dependent transmission measurements were carried out. Figure 1.8b shows an absolute sensitivity map for the quasi 3D nanohole array obtained by taking the absolute value of the difference in the PBZ before and after formation of the SAM. Interestingly, regions of higher sensitivity in the map lie close to areas where several SPP dispersion curves intersect, suggesting that the coupling of SPP modes may be responsible for the increased sensitivity. Although these simple SPP dispersion relations explain some of the behavior observed in the PBZ, other regions of higher sensitivity are found away from the plotted dispersion curves. Additional work is needed to fully characterize the PBZ of both the quasi 3D and full 3D nanohole arrays and the nanopost arrays.

1.5.2 Finite-Difference Time-Domain Computational Modeling and Optimization of Plasmonic Crystals

Although a more thorough understanding of the underlying physics of these devices is of interest, there is also a need to predict the optical properties of devices with arbitrary design rules without the expense of physical fabrication. While the PBZ maps clearly show the presence of propagating SPP modes, other plasmonic features are also supported by these plasmonic crystals. The periodic grating structure generates counterpropagating SPPs, giving rise to Bloch wave SPPs.[75] Additionally, the grating structure itself creates Wood anomalies, although these are diffractive phenomena rather than plasmonic ones.[4,16,75] The individual nanoholes and nanoposts can also support localized SPRs.[19,76,77] In lieu of a comprehensive physical modeling accounting for the presence and interaction between these features, we have extensively modeled these structures computationally using an implementation of the finite-difference time-domain method.[75,78]

A unit cell containing a single nanostructure (hole or post) with the appropriate dimensions and metal distribution is considered with appropriate boundary conditions to model an infinite square planar array. The unit cell itself is subdivided into a number of grid points with an arbitrary spacing in the *x*, *y*, and *z* dimensions. (A smaller grid spacing results in a more accurate description of the optical properties of the device but comes at a large computational cost.) The interaction between the nanostructure and the electric and magnetic fields of propagating light are evaluated according to Maxwell's equations at each point in the unit cell for a predetermined length of time (on the order of 100 femtoseconds), and quantities such as the zero-order transmission of light are derived from these results.

Figure 1.9 shows a comparison between experimental transmission spectra and those calculated from the FDTD modeling for the nanopost (Figure 1.9a) and full 3D nanohole (Figure 1.9b) systems in air, and the correspondence between the experimental and modeled spectra is quite good for both systems.[60] Discrepancies may arise from a combination of effects, such as a physical geometry that differs slightly from that modeled, an incomplete approximation of the wavelength-dependent refractive indices of the metal and dielectrics, and nanoscale defects or variations in the actual metal layer thicknesses. Figure 1.10a shows a comparison between the experimental and modeled transmission spectra for a quasi 3D nanohole array.[4] Although the ideal crystal modeled spectrum correlates fairly well with the experimental transmission spectrum, the idealized crystal model does not include small gold grains (~20-30 nm in size) along the edge of the gold disc at the bottom of the nanohole which were experimentally observed. Inclusion of these features in the modeled structure gives the "real crystal" modeled spectrum and further improves the fit to the experimental data. Indeed, the optical properties of these nanoimprinted plasmonic crystals are well characterized by the FDTD method.

FDTD calculations of these structures can also reveal the electric fields associated with the active plasmonic resonances in these devices. Figure 1.10b shows the electric field distributions associated with the features marked "B" and "C" in the transmission spectra shown in Figure 1.10a for a quasi 3D nanohole array.[4] The feature marked "B" shows a localized surface plasmon resonance mode that is tightly confined around the top rim of the nanohole. The feature marked "C" corresponds to overlapping Bloch wave SPP and Wood anomaly excitation at the interface between the gold film and the molded polymer that shows strong coupling between the gold disc at the bottom of the hole and the upper rim. The intensities and locations of these electric fields are of significant importance in applications such as surface-enhanced

Raman scattering,[24] and the ability to computationally model those fields makes possible the rational design and optimization of these nanostructures.

Further FDTD calculations were performed to optimize the figure of merit of full 3D nanohole plasmonic crystals for bulk refractive index sensing between 400 – 1000 nm.[72] The parameters tuned were the relief depth, periodicity and diameter of the nanoholes as well as the metal thicknesses on the top surface, on the sidewalls, and on the bottom surface of the nanohole. By simulating the transmission spectra for a series of bulk refractive indices, integrated responses and figures of merit can be computed and compared. Figure 1.11a shows the results of varying the periodicity of the nanohole array (nanohole diameter scaled as 60% of the periodicity) with a constant relief depth of 350 nm and constant gold thicknesses. The calculations clearly show a peak in the sensitivity of this configuration for a periodicity of 524 nm (and hole diameter of ~314 nm). Although not all of the periodicity and hole diameter combinations were experimentally available, experimental results do support the trend revealed by the FDTD calculations.

Figure 1.11b and Figure 1.11c show similar optimization calculations in which the gold thickness (assumed to be uniform on the tops, bottoms, and sidewalls of the nanohole arrays) was varied for two different sets of relief depths, hole diameters, and periodicities. Although the figure of merit peaks at approximately the same gold thickness (~96 nm) in both systems, the behavior of the figure of merit is markedly different. Further experimental work is needed to verify these trends as well as to explore other nanostructure architectures, but these results serve to emphasize the intricate interdependencies between the design rule parameters. Additionally, while the sensitivity optimized here (over wavelengths between 400 – 1000 nm) may not be

appropriate for all possible uses, similar calculations can be carried out to optimize the performance of these devices as dictated by the application.

1.6 One-Dimensional Sensing Applications of Nanoimprinted Plasmonic Crystals

Despite the high sensitivity of these plasmonic crystals to bulk refractive index changes at visible and near-infrared wavelengths, their application in thin film sensing may be more analytically relevant. The evanescent nature of the electric field associated with surface plasmon resonances affords these devices high sensitivity to refractive index changes at distances on the order of hundreds of nanometers from the metal-dielectric interface. The small sampling volume probed by these plasmonic crystals makes them inherently sensitive to thin film changes, and they have been used to measure the dynamic adsorption of biomolecules on the plasmonic crystal surface.[4,61] Additionally, by coupling the plasmonic crystal with a pH sensitive hydrogel, these plasmonic crystals can optically measure chemomechanical forces.[79]

1.6.1 Antibody Assays Using Plasmonic Crystals

Antibody/antigen assays have been performed using full 3D nanohole plasmonic crystals with excellent quantitative results.[61] Antigoat IgG was immobilized on the plasmonic crystal surface and exposed to solutions of goat IgG of varying concentrations through a flow cell. The transmission changes (and thus the change in the integrated response) was measured as a function of the goat IgG concentration in the surrounding medium corresponding to surface coverage of goat IgG on the plasmonic crystal. The data presented in Figure 1.12a show a change in the normalized integrated response that is well described by a Langmuir adsorption

model. Fitting the data to a Langmuir isotherm results in an estimate of the surface confined affinity constant of approximately 7×10^{7} M^{-1}, consistent with previously reported results for other IgG/anti-IgG systems.

Figure 1.12b shows the results of a biotin-avidin sandwich assay carried out using a quasi 3D nanohole plasmonic crystal.[4] A biotinylated bovine serum albumin (bBSA) monolayer was nonspecifically adsorbed onto the plasmonic crystal using a flow cell, leading to the first plateau in the integrated response seen in Figure 1.12b. Subsequent introduction of both phosphate buffered saline (PBS) and unmodified bovine serum albumin (BSA) resulted in no significant change in the integrated response, confirming that no additional material had adsorbed onto the plasmonic crystal surface. Injection of avidin led to a further increase in the integrated response as expected from the binding of an additional layer of material on the plasmonic crystal surface. Injection of a second bBSA layer did not generate as large a change in the integrated response as the first, although this is consistent with other experimental observations of layer-dependent mass coverage in similar assays.[80,81]

1.6.2 Thickness Measurements of Polyelectrolyte Thin Film Assemblies

Although the diminishing change in integrated response demonstrated in the biotin-avidin assay agrees with previous reports in the literature, it presents an opportunity to further investigate the impacts of the exponential decay of the electric field from the plasmonic crystal surface. Polyelectrolyte thin films were deposited on the surface of a full 3D nanohole plasmonic crystal via layer-by-layer assembly, and the change in transmission of the assembly in water was investigated as a function of the layer thickness.[61] Figure 1.13a presents a normalized transmission change map (normalized to the initial transmission when no polyelectrolyte layer

was present) over wavelengths between 350 – 1050 nm, and Figure 1.13b presents the normalized transmission change for four selected wavelengths. The multiple SPP and LSPR modes supported by these plasmonic crystals gives rise to complex interactions between them and the surrounding environment, and this can be seen by the nonlinear behavior in the single wavelength transmission changes.

Integrated responses were calculated from the transmission data as a function of polyelectrolyte layer thickness and are presented in the Figure 1.13c. The integrated response clearly increases with the polyelectrolyte layer thickness. However, the integrated response does not increase linearly *ad infinitum* and appears to saturate at polyelectrolyte thicknesses greater than ~95 nm, representing an upper film thickness limit to the use of the integrated response as an analytical measure for this particular plasmonic crystal. Single wavelength responses do continue to change at larger layer thicknesses and can be used for measurements past this limit. Despite this, the integrated response still responds linearly for layer thicknesses up to ~70 nm, and the continued use of the integrated response of these plasmonic crystals as an analytical metric still bears merit since the film thicknesses involved in most bioassays lie within this linear response regime.

1.6.3 Optical Measurement of pH Change Through Chemomechanical Forces

These nanoimprinted plasmonic crystals have demonstrated great sensitivity to changes in the bulk refractive index as well as to thin film changes at the plasmonic crystal surface. However, their utility is ultimately limited by the refractive index contrast present in the application. While numerous methods exist to measure pH colorimetrically and electrochemically, direct measurement of pH using only the refractive index contrast is

extremely difficult. The refractive index change between buffered solutions of pH = 1.44 and 7.86 is extremely small, less than 1×10^{-4} refractive index units.[79] By instead modifying the plasmonic crystal with a hydroxyethyl methacrylate hydrogel sensitized to pH by a small amount of crosslinked acrylic acid, a change in the pH of the bulk environment results in changes in the protonation state of the acrylic acid, generating electrostatic interactions that swell or collapse the hydrogel. This pH change in the bulk results in a mechanical change in the hydrogel at the plasmonic crystal surface.

The data presented in Figure 1.14 show the optical response of the hydrogel modified plasmonic crystal with changes in pH. The spectral difference map presented in Figure 1.14a clearly shows a change in transmission as the system is cycled between pH = 7.86 and pH = 1.44. Additionally, the changes are clearly reversible with the transmission returning to its original state, even after several cycles of pH changes. The relative integrated response changes are presented in Figure 1.14b for three different sets of pH changes – 7.86 to 1.44 (blue), 6.42 to 5.13 (red), and 5.76 to 5.66 (black). Larger pH changes show correspondingly larger changes in the relative integrated response as a result of a greater change in hydrogel osmotic pressure and swelling. Impressively, even a change of only 0.10 pH units is clearly distinguishable as seen in the magnified inset.

Interestingly, the hydrogel layer is thicker than the distance penetrated by the evanescent electric field of the plasmonic crystal.[4] Because of the hydrogel thickness and the extremely small refractive index differences in the solutions used, the changes in optical response must have been the result of the change in hydrogel volume and the associated mechanical forces exerted electrostatically by the acrylic acid moieties in their different protonation states. By transducing chemical changes in the environment to mechanical forces at the plasmonic crystal

surface, introduction of an appropriate sensing element in the hydrogel network can enable the direct measurement of analytes where the inherent refractive index contrast would otherwise be too small to measure.

1.7 Two-Dimensional Chemical Imaging Applications of Plasmonic Crystals

Besides their demonstrated utility in spectroscopic sensing, nanoimprinted plasmonic crystals offer great potential for applications in chemical imaging. The highly uniform patterning over millimeter scale areas offers a large sensing area, and their demonstrated performance and sensitivity permit fully quantitative imaging. We have demonstrated the utility of these plasmonic crystals for high performance imaging at both near infrared and visible wavelengths with exceptional sensitivity for surface-bound species.[4,59-61]

1.7.1 Protein Thin Film Imaging

Thin film imaging experiments complementary to the spectroscopic measurements previously described were performed using all of the nanoimprinted structure geometries previously described (quasi 3D and full 3D nanoholes, nanopost). The structures' complementary wavelength characteristics allow for their use in the near infrared and the visible spectrum to image protein thin films. In these examples, fibrinogen was nonspecifically adsorbed onto the plasmonic crystal surface through a microfluidic channel to generate line patterns.[60,62] Figure 1.15a presents of the near-infrared transmission imaging of a single sample of nonspecifically adsorbed fibrinogen thin films onto the surface of a quasi 3D nanohole

plasmonic crystal under white light illumination.[62] Even under white light, these 8 nm thick protein films are readily distinguished from the surrounding areas.

Spectrally resolved imaging of the fibrinogen layers demonstrate the previously observed response of the underlying surface plasmon resonances to refractive index changes at the metal-dielectric interface. Spectroscopic bulk refractive index measurements in Figure 1.5b revealed wavelength where the transmission increased with a change in refractive index while the opposite behavior was observed at other wavelengths. This contrast inversion is plainly evident in the single wavelength imaging presented in Figure 1.15b (1090 nm) and Figure 1.15c (1200 nm). Because the protein lines in Figure 1.15a appear darker than the surrounding areas, the overall change in transmission across the entire wavelength range captured must be lower where the protein is adsorbed on the plasmonic crystal. However, the wavelengths at which the transmission actually increases when the protein is absorbed will effectively reduce the observed image contrast under white light illumination, and spectrally resolved imaging that accounts for this factor can be exploited to increase the contrast. Despite this caveat, the high performance and sensitivity of the quasi 3D nanohole geometry in the near infrared allows for larger-area imaging of thin films at near-infrared wavelengths.

Fibrinogen layers were also imaged on full 3D nanohole and nanopost plasmonic crystals, and the imaging performance is compared between the nanopost crystal (Figure 1.15d) and a full 3D nanohole crystal (Figure 1.15e).[60] Although the nanopost plasmonic crystal showed greater bulk refractive index sensitivity, the opposite appears to be true in this thin film imaging experiment – the nanohole plasmonic crystal shows a larger difference in image intensity between the fibrinogen line and the surrounding area. An important distinction to be made is that the bulk refractive index measurements were made in water, while the thin film

images were captured in air. The complexity of the SPR behavior in different environments results in this seemingly paradoxical behavior is in fact confirmed by FDTD simulations of both systems under both conditions. The complexity of the SPR behavior in different environments results in performances of the different nanostructures (nanopost, quasi 3D nanohole, full 3D nanohole) that are, in practice, complementary to each other – the optimal device architecture is ultimately application-specific.

1.7.2 Molecular Rulers and Film Thickness Calibration of Plasmonic Crystals

The analytical power of these nanoimprinted plasmonic crystals has been demonstrated in molecular ruler imaging experiments carried out on full 3D nanohole arrays.[61] Thin films of proteins of known thickness were microfluidically deposited to establish a calibration between the observed imaging response and surface coverage. Figure 1.16a shows an optical image of three proteins adsorbed onto the plasmonic crystal (from left to right: fibrinogen, γ-globulins, and myoglobin), while Figure 1.16b gives an average thickness profile. Once again, the protein lines are clearly visible because of the refractive index contrast with the protein-free regions, and estimates of the protein film thicknesses based on a calibration using a self-assembled monolayer were in good agreement with ellipsometric thickness measurements.[82] These visible spectrum measurements were made using white light illumination and a common silicon-based charge-coupled device (CCD) camera mated to a common optical microscope, demonstrating the practical sensitivity of the full 3D nanohole plasmonic crystal at visible wavelengths.

The analytical sensitivity of the full 3D nanohole plasmonic crystals is demonstrated in Figure 1.17. A self-assembled monolayer of 1-octadecanethiol (ODT) was patterned on the metal surface, and a visible light image of the pattern is shown in Figure 1.17a.[59] The rest of the

surface was backfilled with a layer of 1-hexadecanethiol (HDT), and the resulting image is shown in Figure 1.17b. Although the ODT pattern is somewhat degraded as a result of infilling of HDT into defect areas in the ODT monolayer as well as dynamic exchange between the ODT on the surface and HDT in solution, the ODT pattern is still readily visible. Compared to the initial contrast between the ODT monolayer and the surroundings, the addition of HDT reduces the contrast to ~10% of its original value. This corresponds strikingly well with the ~11% difference in chain length between 1-octadecanethiol and 1-hexadecanethiol. Indeed, the use of these full 3D plasmonic crystals enables visible light imaging of high sensitivity (down to a difference of two methylene groups) using an inexpensive substrate and common laboratory equipment (optical microscope and CCD camera).

1.8 Surface-Enhanced Raman Scattering on Nanoimprinted Plasmonic Crystals

Raman spectroscopy is a non-destructive vibrational spectroscopy technique in which photons interacting with a molecule are instantaneously scattered, but these scattered photons are shifted in frequency relative to the original.[83] In Stokes Raman scattering, the scattered photon has less energy than the incident photon and is the result of an interaction between the molecule and the photon that leaves the molecule in an excited vibrational state. An analogous process takes place in anti-Stokes Raman scattering, where the scattered photon has greater energy than the incident photon – the molecule ends in a lower (less excited) vibrational state than where it started. In both cases, the energy difference between the incident and the scattered photons is the same as the energy of the particular vibrational mode that was excited (Stokes scattering) or relaxed (anti-Stokes scattering).

A major limitation of Raman scattering is its inefficiency; Raman scattering has an inherently small scattering cross-section. As a comparison, the fluorescence cross section of Rhodamine 6G is on the order of ~10^{-16} cm^2,[84] while its Raman scattering cross section is around *eleven* orders of magnitude smaller (~10^{-27} cm^2), [85] and the cross-section other analytes can be even smaller. Because of this small scattering cross section, Raman spectroscopy is almost exclusively performed using lasers to illuminate the sample; the monochromatic light and high photon flux achievable using lasers can help to increase the Raman signal from the analyte.

The underlying physics and evanescent electric fields associated with these nanostructured plasmonic crystals are responsible for their utility as surface plasmon resonance sensors, but these same phenomena are responsible, in large part, for surface-enhanced Raman scattering (SERS).[19-24] The use of plasmonic substrates, especially those capable of supporting localized surface plasmon resonances, can greatly enhance the Raman scattering from a molecule. Because Raman scattering is a second order process (the result of interactions between an incident photon and phonon modes unique to the molecule), enhancements of the electric field intensity |E| (as a result of the surface plasmon modes supported by the substrate) lead to enhancements of the Raman scattering proportional to $|E|^2$ at the incident photon wavelength as well as the scattered photon wavelength.[86] All told, the evanescent electric fields associated with these plasmonic substrates can yield Raman enhancements proportional to $|E|^4$. Despite the rich vibrational data obtained using Raman-related techniques, the lack of reproducible SERS substrates with large signal enhancements has significantly hampered the widespread adoption of SERS as an analytical tool.[48] To this end, soft nanoimprint lithography allows us to replicate nanostructures over large areas with high fidelity which we have shown to generate uniform SERS enhancements across the entire plasmonic crystal surface.[24]

Benzenethiol (BT) was chosen as the SERS reporter molecule in these experiments, and a BT monolayer was formed on the surface of a quasi 3D nanohole plasmonic crystal.[24] The Raman spectra shown in Figure 1.18a are in good agreement with previous reports from the literature,[87] and subsequent analysis focused on the peak at ~1073 cm^{-1}. The overlaid spectra in Figure 1.18a show the spectra collected for nanohole arrays with three different sets of hole diameters and periodicities and show a dependence of the SERS signal enhancement on the design rules of the substrate, a reasonable expectation considering the dependence of the individual plasmonic modes on the device geometry. Analytical SERS enhancement factors from 10^4 to 10^5 were obtained on these substrates without further optimization, on par with other SERS substrates fabricated using serial processing procedures.

The Raman signal enhancement observed in these devices is attributed to a localized surface plasmon resonance that establishes the enhanced electric field from which the SERS enhancement is derived. A maximum enhancement is expected when the spectral position of this LSPR is halfway between the laser excitation wavelength (785 nm in this work) and the wavelength of the Raman scattered photon (857 nm in this work, corresponding to a Raman shift of 1073 cm^{-1}),[88] corresponding to a LSPR wavelength of 826 nm in this work. In fact, the transmission intensity at 826 nm for the 16 different nanohole arrays (of varying hole diameter and periodicity) is strongly correlated to the corresponding Raman signal intensity as shown in Figure 1.18b.

Considering the LSPR wavelength as a design criterion leads to two conclusions: First, no single design rule can generate equivalent enhancements at all Raman shifts. Instead, an optimal design rule depends on both the excitation wavelength and the Raman shift desired. This could be exploited to preferentially enhance certain Raman bands over others, possibly reducing

the complexity of the Raman data when multiple Raman-active analytes are present. Second, the strong correlation between the Raman intensity and the transmission intensity offers a ready metric for computational optimization of the Raman enhancement. Multiple design rules and nanostructure geometries can be investigated *in silico* to maximize transmission at the LSPR wavelength to optimize the Raman enhancement without the expense associated with physical fabrication of the nanostructures themselves. Figure 1.18c shows that the electric field from the LSPR in this experiment is localized at the upper rim of the nanohole. Knowledge of the electric field distribution offers the potential for further device optimization by designing modifications that may trap analytes of interest at locations where the electric field is strongest, further enhancing the analytical sensitivity.

The large area, highly uniform nanostructures produced by the nanoimprinting process makes these substrates attractive for use in SERS imaging. The top image in Figure 1.18d shows a plasmonic crystal that was molded in previously photodefined SU8, resulting in a structure in which the nanohole array is only embossed in the areas making up the letters "UIUC." Benzenethiol was adsorbed across the entire surface, but the Raman map (for the signal at 1073 cm^{-1}) shown in the bottom panel of Figure 10.18d shows that a Raman signal is only observed at areas where the nanohole array is present. Furthermore, the Raman intensity is uniform across the entire nanostructured surface. The inexpensive fabrication and uniform performance of these nanoimprinted plasmonic crystals make them promising substrates for further application in SERS sensing and imaging.

1.9 Figures

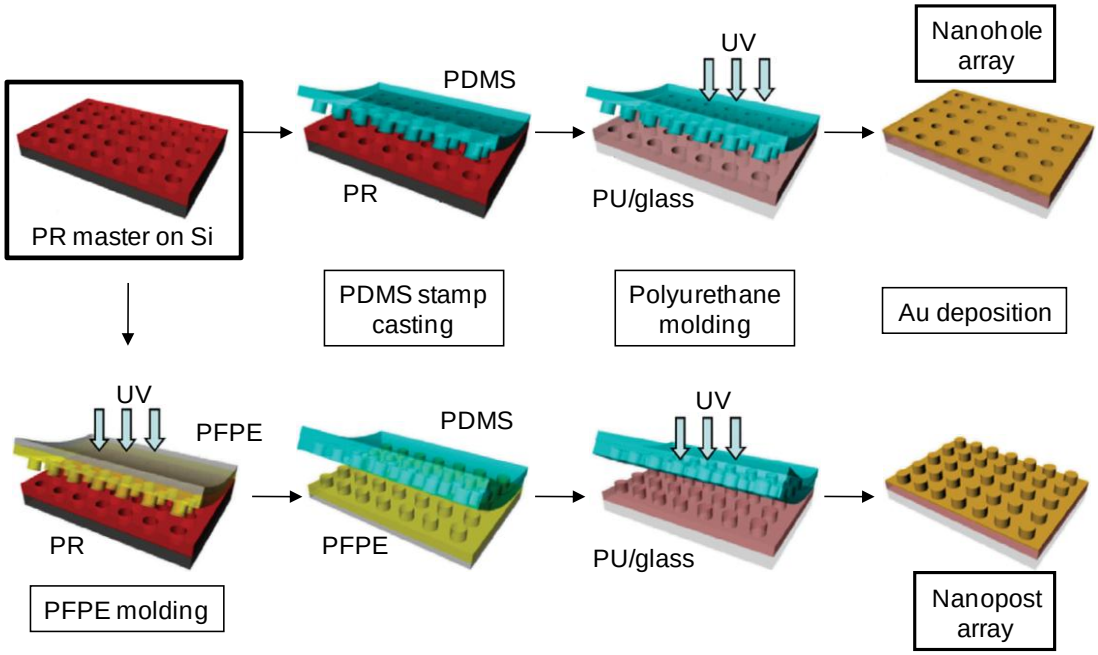

Figure 1.1 Generalized procedure for nanoimprint lithography fabrication of nanohole (top) and nanopost (bottom) plasmonic crystals. A photolithographically defined layer of photoresist on silicon is used as a master. To create a nanohole array stamp, a polydimethylsiloxane (PDMS) stamp is cast directly from the master. A nanopost array stamp is fabricated by first casting and curing an acryloxy perfluoropolyether (PFPE) intermediate under ultraviolet (UV) light. This PFPE intermediate is then used to cast a PDMS stamp. The stamp is then used to mold a layer of photocurable polyurethane on a glass slide. Removal of the stamp leaves a nanohole or nanopost array which is then metalized to complete the plasmonic crystal. Reprinted and adapted with permission from [60]; copyright 2009 IOP Publishing Ltd

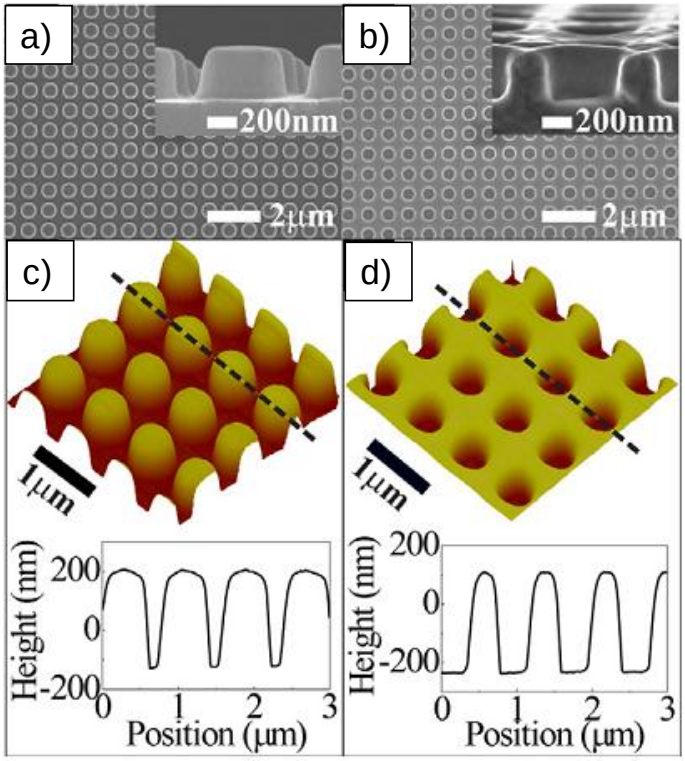

Figure 1.2 a) and b) SEM images of nanopost (a) and nanohole (b) plasmonic crystals with cross-section insets. c) and d) AFM mappings of nanopost (c) and nanohole (d) plasmonic crystals with height profile line cuts. Reprinted and adapted with permission from [60]; copyright 2009 IOP Publishing Ltd

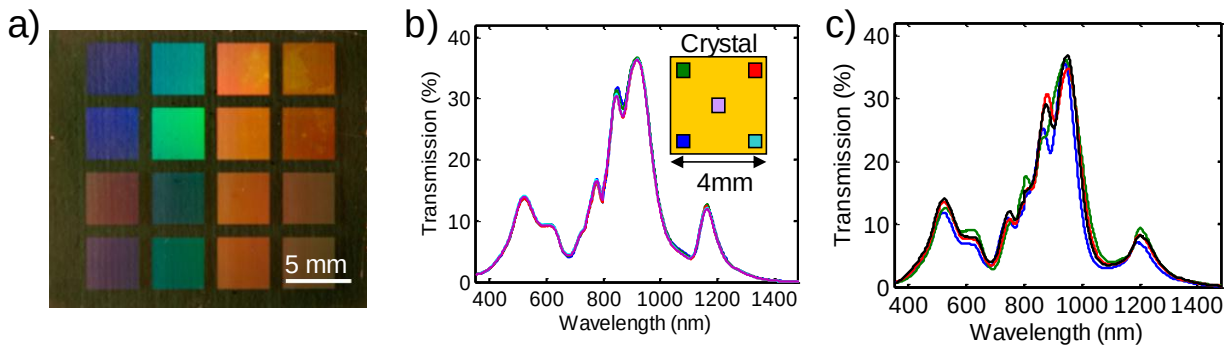

Figure 1.3 a) Optical image of a completed full 3D nanohole plasmonic crystal. b) Transmission spectra overlay for four different full 3D nanohole plasmonic crystals illustrating similar optical responses between samples. c) Transmission spectra overlay for five points within the same full 3D nanohole plasmonic crystal illustrating highly reproducible optical response within a single sample over large areas. (b) and (c) were collected on a plasmonic crystal with a periodicity of 748 nm, a hole diameter of 456 nm, and a relief depth of 350 nm. (b) and (c) reprinted with permission from [71]; copyright 2010 Wiley-VCH Verlag GmbH & Co.

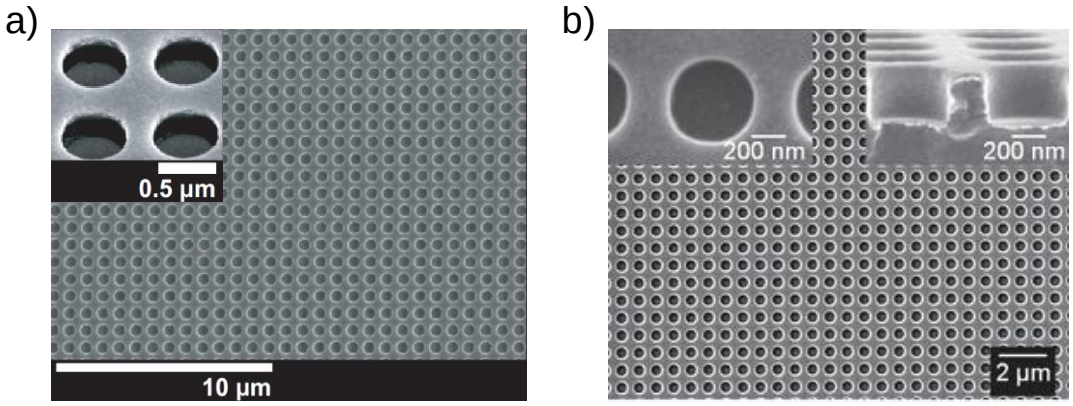

Figure 1.4 a) SEM image of a quasi 3D nanohole array with angled SEM image (inset) showing no gold on nanohole sidewalls. Reprinted and adapted with permission from [4]; copyright 2006 National Academy of Sciences, U.S.A. b) SEM image of full 3D nanohole array with magnified view of a single nanohole (left inset) and cross section SEM image (right inset) showing continuous metal layer on top and bottom surfaces and on sidewalls of nanohole. Reprinted with permission from [59]; copyright 2008 Wiley-VCH Verlag GmbH & Co.

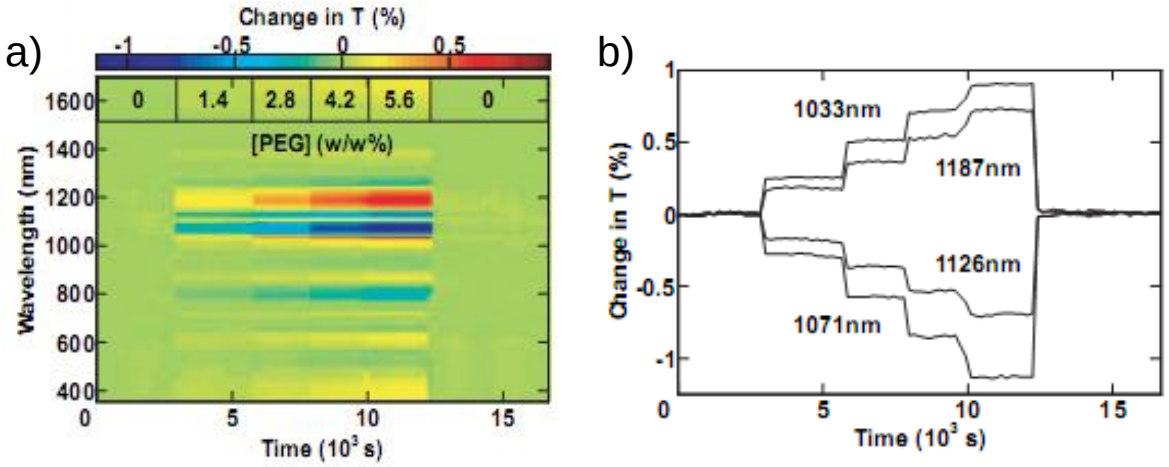

Figure 1.5 a) Time-resolved transmission difference map for a quasi 3D nanohole plasmonic crystal corresponding to serial injections of aqueous poly(ethylene glycol) (overlaid). b) Time resolved transmission differences for serial injections of aqueous poly(ethylene glycol) at four selected wavelengths. Reprinted with permission from [4]; copyright 2006 National Academy of Sciences, U.S.A.

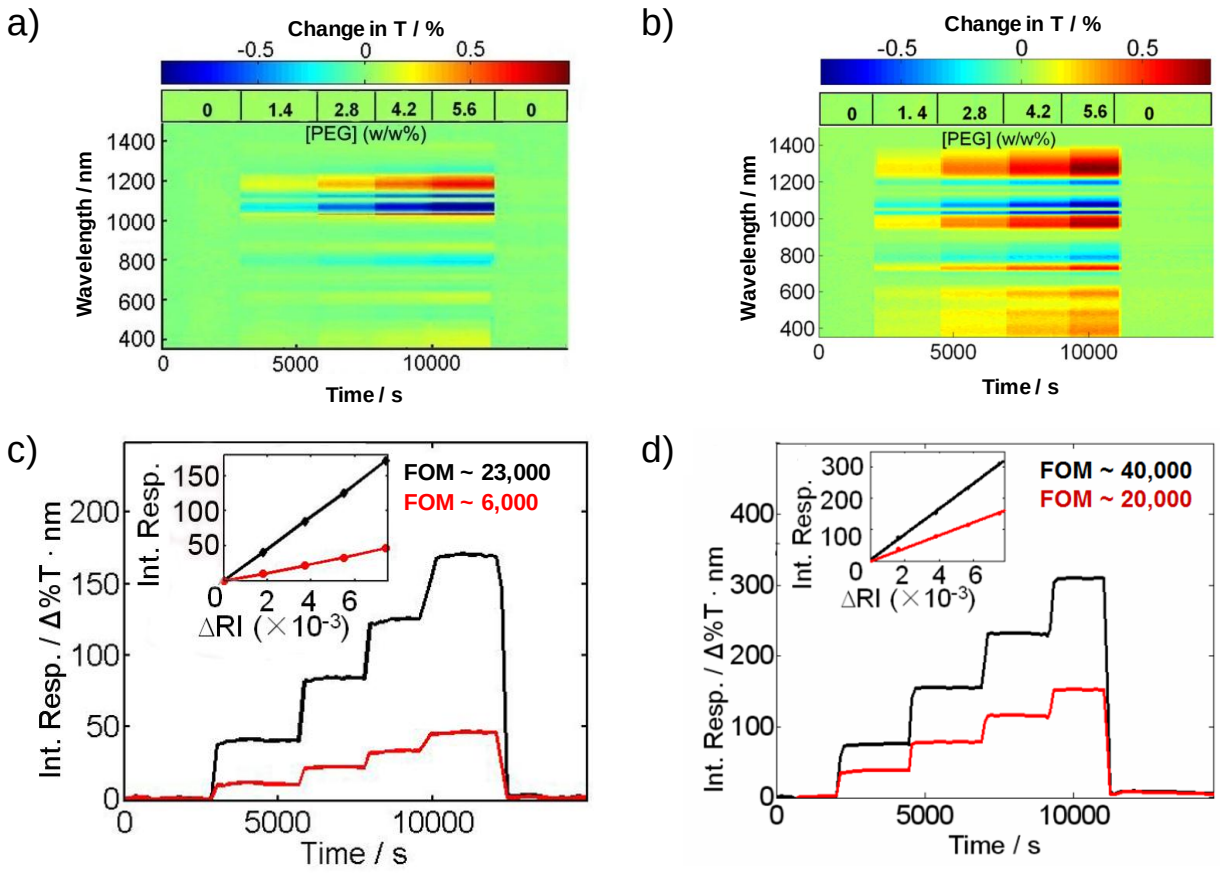

Figure 1.6 a) and b) Transmission difference maps for bulk refractive index sensitivity of quasi 3D nanohole (a) and full 3D nanohole (b) plasmonic crystals. C) and d) Integrated response calculations and figure of merit calculations (insets) for bulk refractive index sensitivity of quasi 3D (c) and full 3D (d) nanohole plasmonic crystals. Black curves in (c) and (d) correspond to integration from 355-1500 nm. Red curves in (c) and (d) correspond to integration from 355-1000 nm. Reprinted with permission from [71]; Copyright 2010 Wiley-VCH Verlag GmbH & Co.

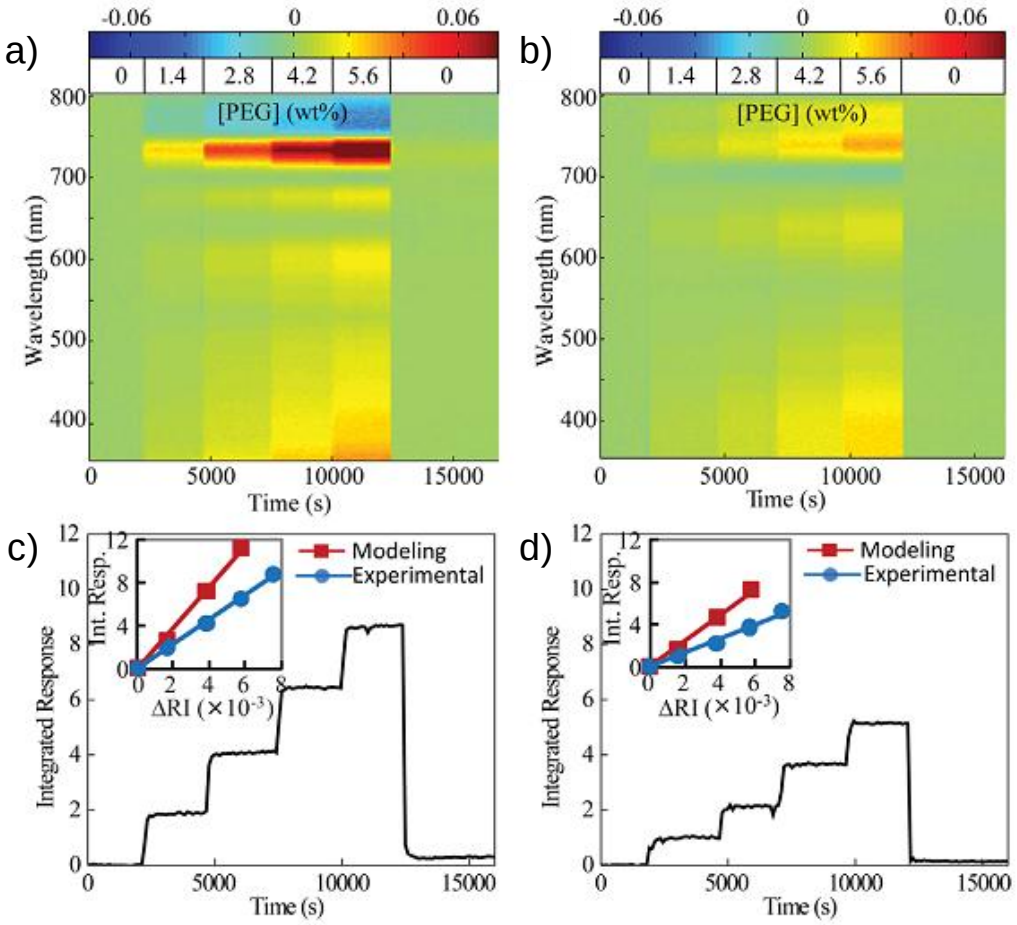

Figure 1.7 a) and b) Normalized transmission difference maps for bulk refractive index sensitivity of nanopost (a) and full 3D nanohole (b) plasmonic crystals. c) and d) Integrated response calculations and figure of merit calculations (insets) for bulk refractive index sensitivity of nanopost (c) and full 3D nanohole (d) plasmonic crystals. Insets of (c) and (d) show experimentally determined integrated responses in blue in comparison with computationally predicted integrated responses in red. Reprinted with permission from [60]; Copyright 2009 IOP Publishing Ltd

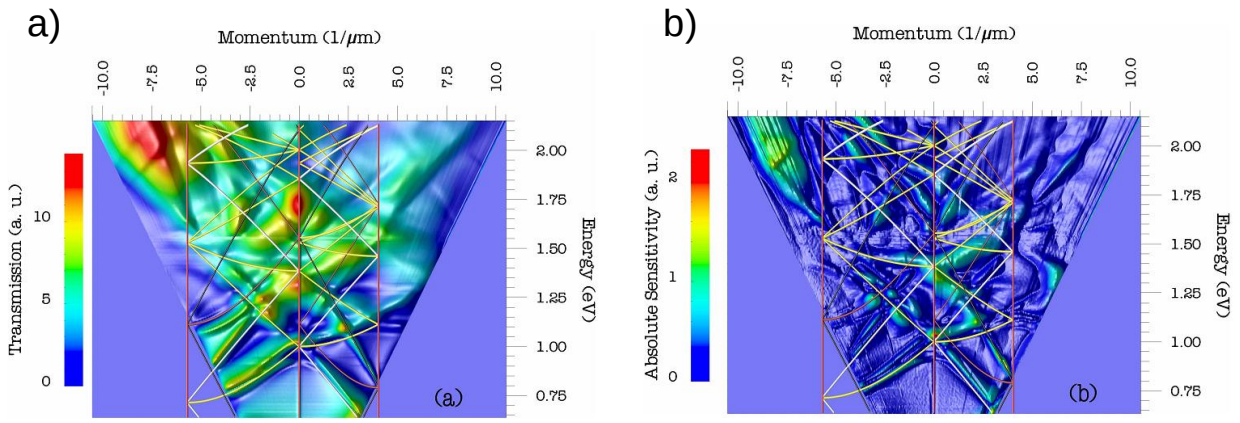

Figure 1.8 a) Plasmonic Brillouin zone map of a quasi 3D plasmonic crystal with overlaid surface plasmon polariton dispersion curves. b) Absolute sensitivity map of quasi 3D plasmonic crystal after formation of a 1-hexadecanethiol self-assembled monolayer with overlaid surface plasmon polariton dispersion curves. Reprinted with permission from [57]; Copyright 2005 Optical Society of America

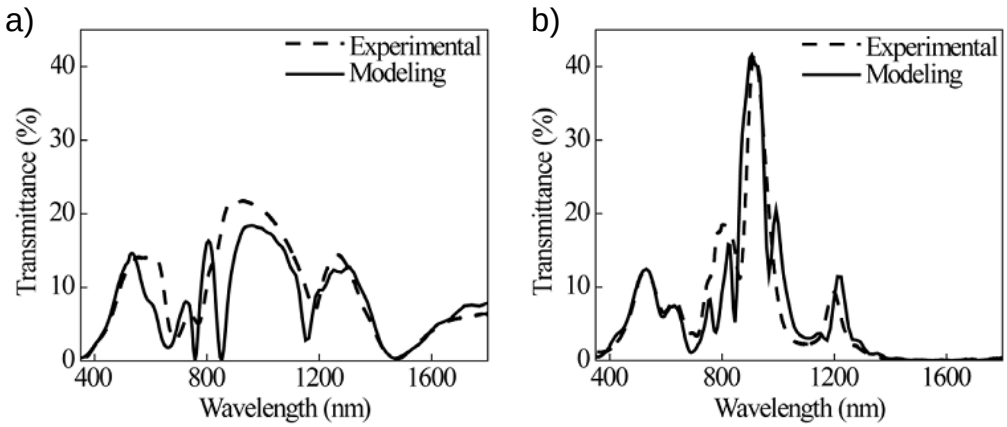

Figure 1.9 Comparison of experimental transmission spectra with those calculated using the finite-difference time-domain method for nanopost (a) and full 3D nanohole (b) plasmonic crystals. Reprinted with permission from [60]; Copyright 2009 IOP Publishing Ltd

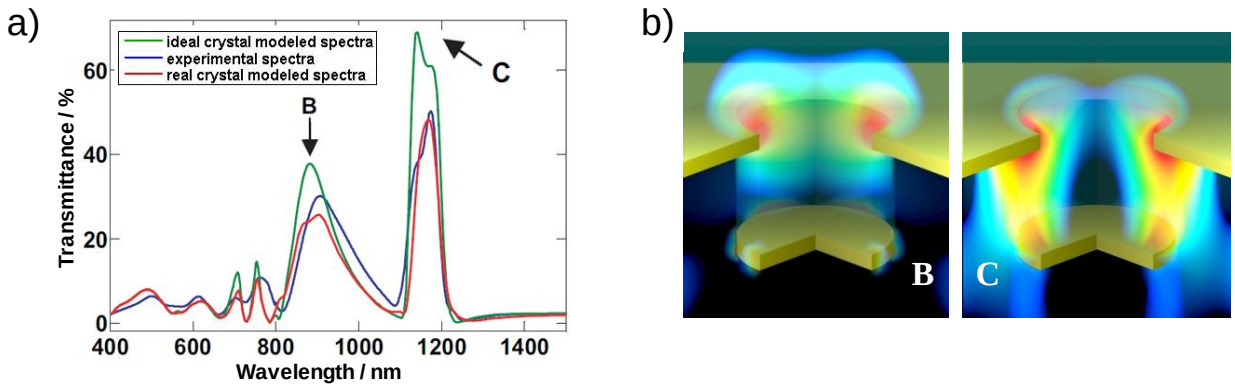

Figure 1.10 a) Experimental (blue) and computationally modeled (red and green) transmission spectra for a quasi 3D nanohole plasmonic crystal. The green curve represents an idealized gold distribution, and the red curve represents a more realistic gold distribution in which small nanograins of gold are included near the edge of the bottom gold disc. b) Calculated electric field distributions for the spectral features marked "B" and "C" in panel a. Reprinted with permission from [4]; Copyright 2006 National Academy of Sciences, U.S.A.

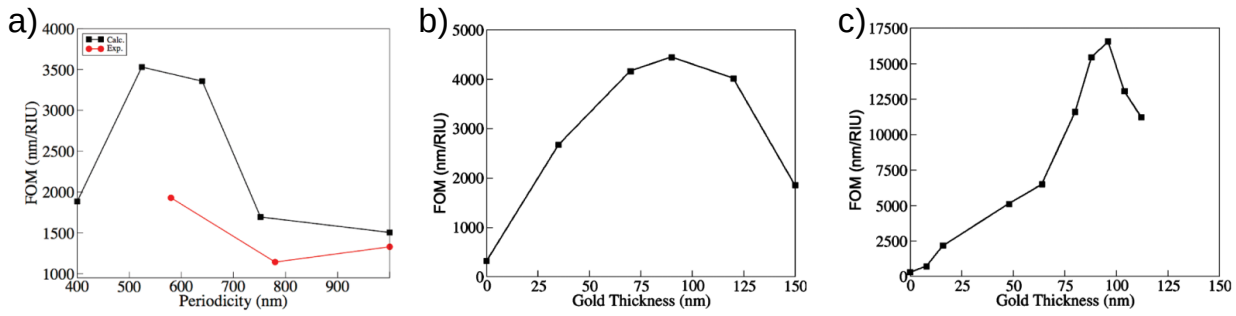

Figure 1.11 Computationally modeled figures of merit for optimization of selected full 3D nanohole design parameters: a) Periodicity of nanohole array variation (with hole diameter fixed as 60% of the periodicity). b) and c) Gold thickness variation assuming a uniform thickness on the top, bottom, and sidewalls of the nanohole for (b) a structure with a 752 nm periodicity, 456 nm hole diameter, and 500 nm relief depth and (c) a structure with a 524 nm periodicity, 320 nm hole diameter, and 400 nm relief depth. Reprinted with permission from [72]; Copyright 2009 American Chemical Society

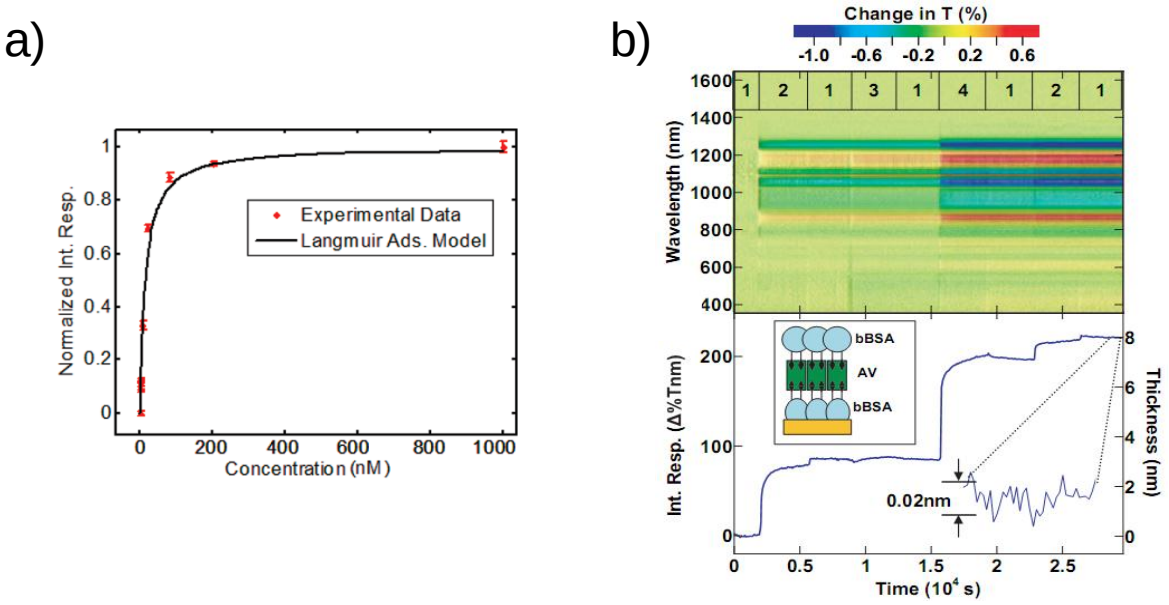

Figure 1.12 a) Quantitative goat IgG/antigoat IgG assay performed on full 3D plasmonic crystal with nonlinear data fit to Langmuir isotherm. Reprinted with permission from [61]; Copyright 2009 American Chemical Society. b) Spectral difference map (top) and integrated response (bottom) for biotin-avidin assay performed on quasi 3D plasmonic crystal with representative schematic inset. Overlaid numbers on spectral difference map correspond to injection sequence of PBS (1), bBSA (2), BSA (3), and avidin (4). Integrated response inset illustrates noise-limited sensitivity corresponding to a layer thickness of 0.02 nm. Reprinted with permission from [4]; Copyright 2006 National Academy of Science, U.S.A.

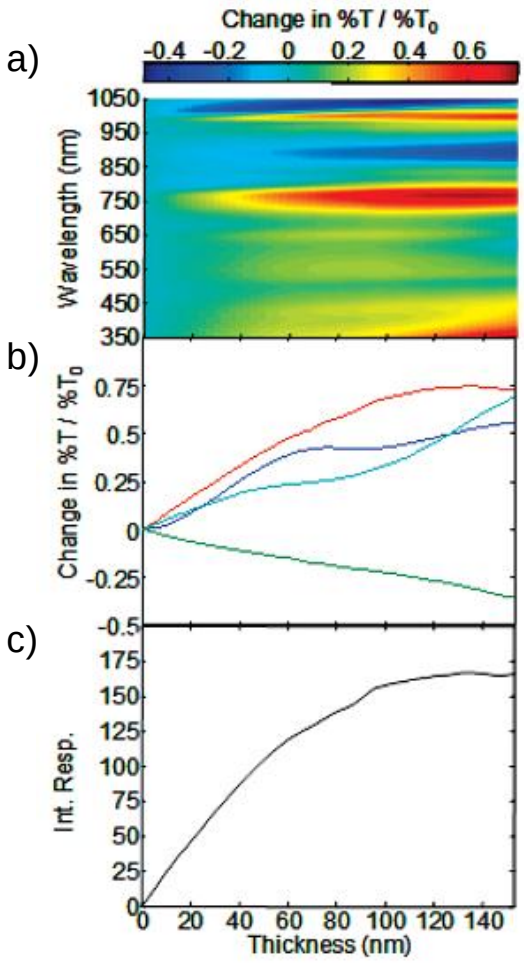

Figure 1.13 a) Normalized spectral difference map, b) normalized transmission difference at 357 nm (cyan), 769 nm (red), 894 (green) and 996 nm (blue), and c) integrated response as a function of polyelectrolyte layer thickness on a full 3D plasmonic crystal. Reprinted with permission from [61]; Copyright 2009 American Chemical Society

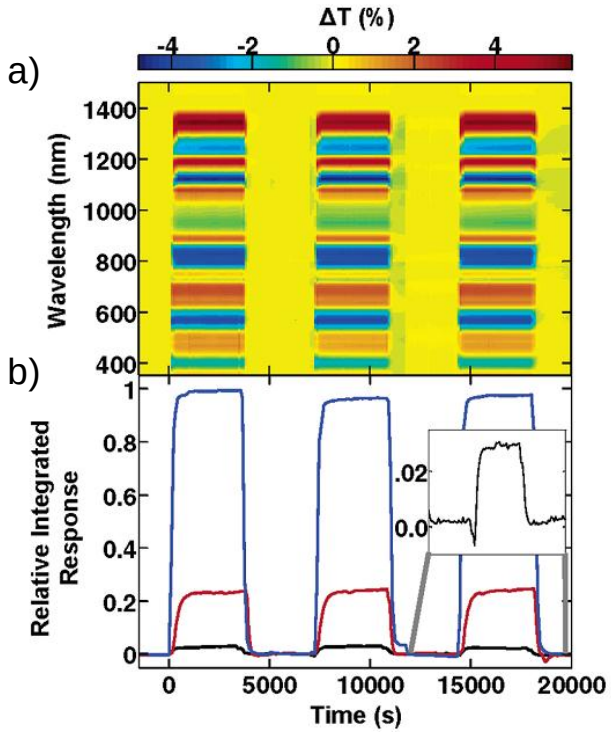

Figure 1.14 a) Transmission difference map for hydrogel-modified quasi 3D nanohole plasmonic crystal cycled from pH 7.86 to 1.44. b) Relative integrated response for hydrogel-modified plasmonic crystal for pH changes of 7.86 to 1.44 (blue), 6.42 to 5.13 (red), and 5.76 to 5.66 (black). Inset shows a magnified view of the black curve. Reprinted with permission from [79]; Copyright 2007 American Chemical Society

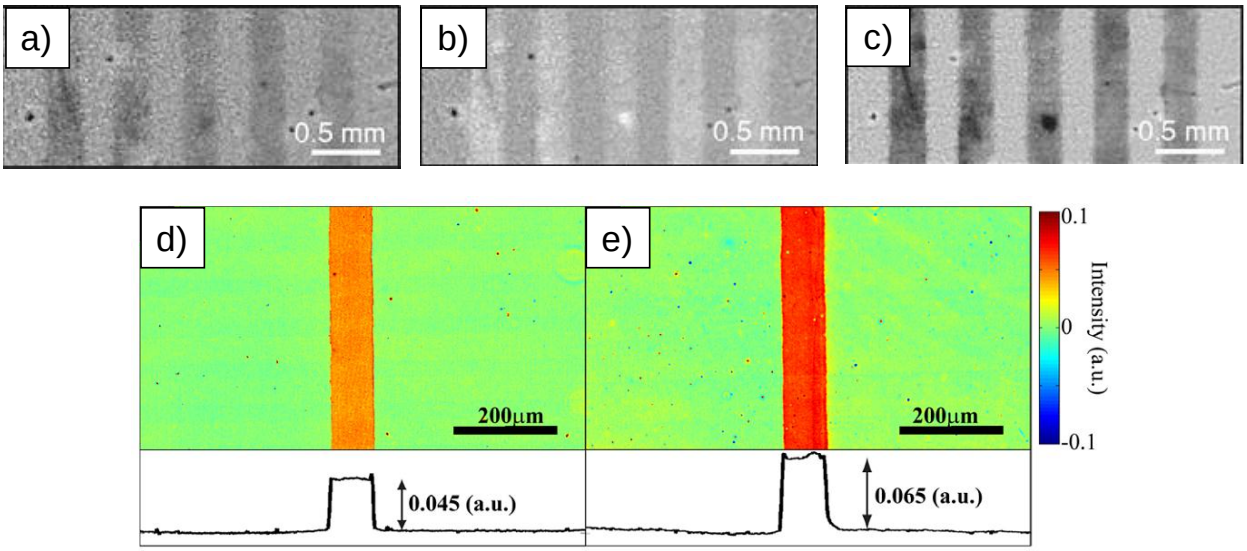

Figure 1.15 a), b), and c) Background corrected spatial imaging of nonspecifically adsorbed fibrinogen lines on quasi 3D nanohole plasmonic crystals illuminated by (a) white light, (b) monochromatic 1090 nm, (c) monochromatic 1200 nm. (a-c) reprinted and adapted with permission from [62]; Copyright 2007 American Institute of Physics. d) and e) Transmitted light image of fibrinogen nonspecifically adsorbed onto nanopost (d) and full 3D nanohole (e) plasmonic crystals with curves corresponding to the measured light intensity contrast determined from the images. (d) and (e) reprinted with permission from [60]; Copyright 2009 IOP Publishing Ltd

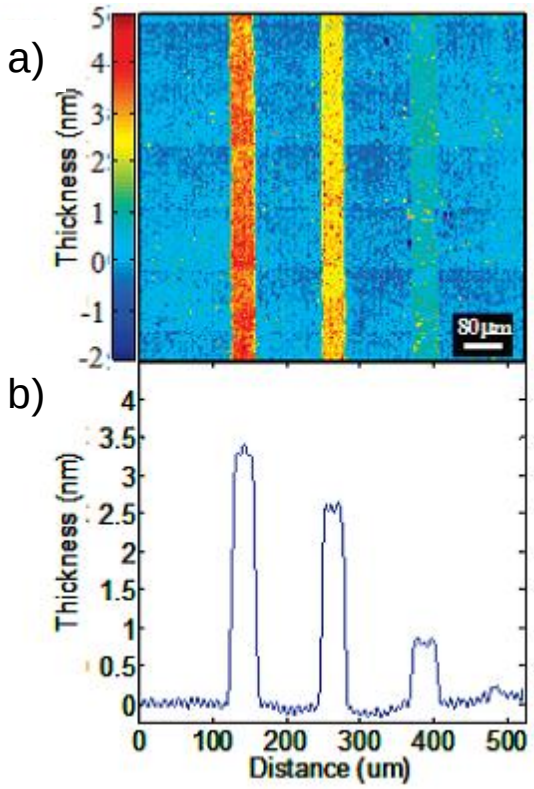

Figure 1.16 a) Quantitative transmission spatial imaging of (left), γ-globulins (center), and myoglobin (right) nonspecifically adsorbed on full 3D nanohole plasmonic crystal with corresponding layer thickness . b) Average height profile for image presented in (a). Reprinted and adapted with permission from [61]; Copyright 2009 American Chemical Society.

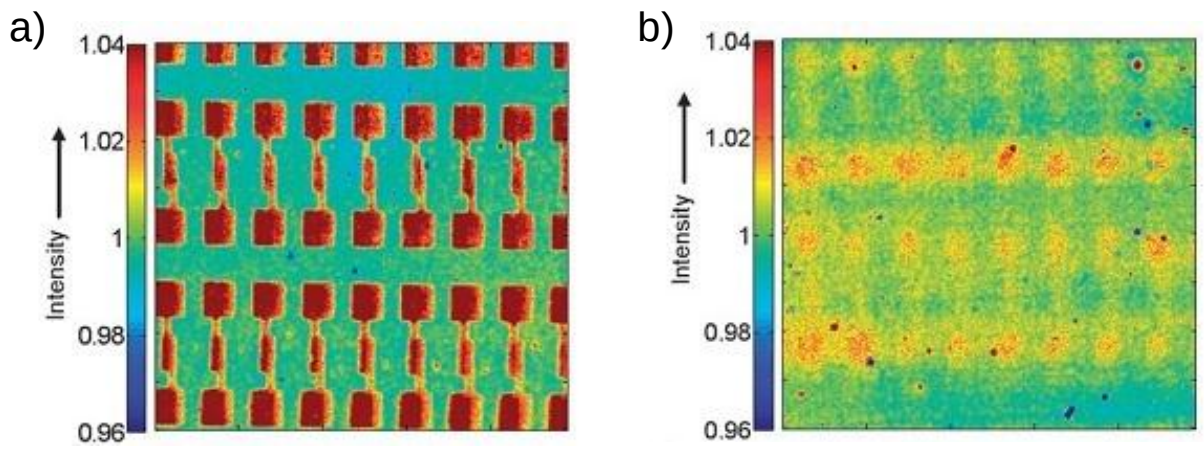

Figure 1.17 Optical transmission images of a 1-octadecanethiol self-assembled monolayer patterned on a full 3D nanohole plasmonic crystal a) before and b) after backfilling with 1-hexadecanethiol for 5 minutes. Box ends of octadecanethiol pattern approximately 50 μm wide. Reprinted with permission from [59]; Copyright 2008 Wiley-VCH Verlag GmbH & Co.

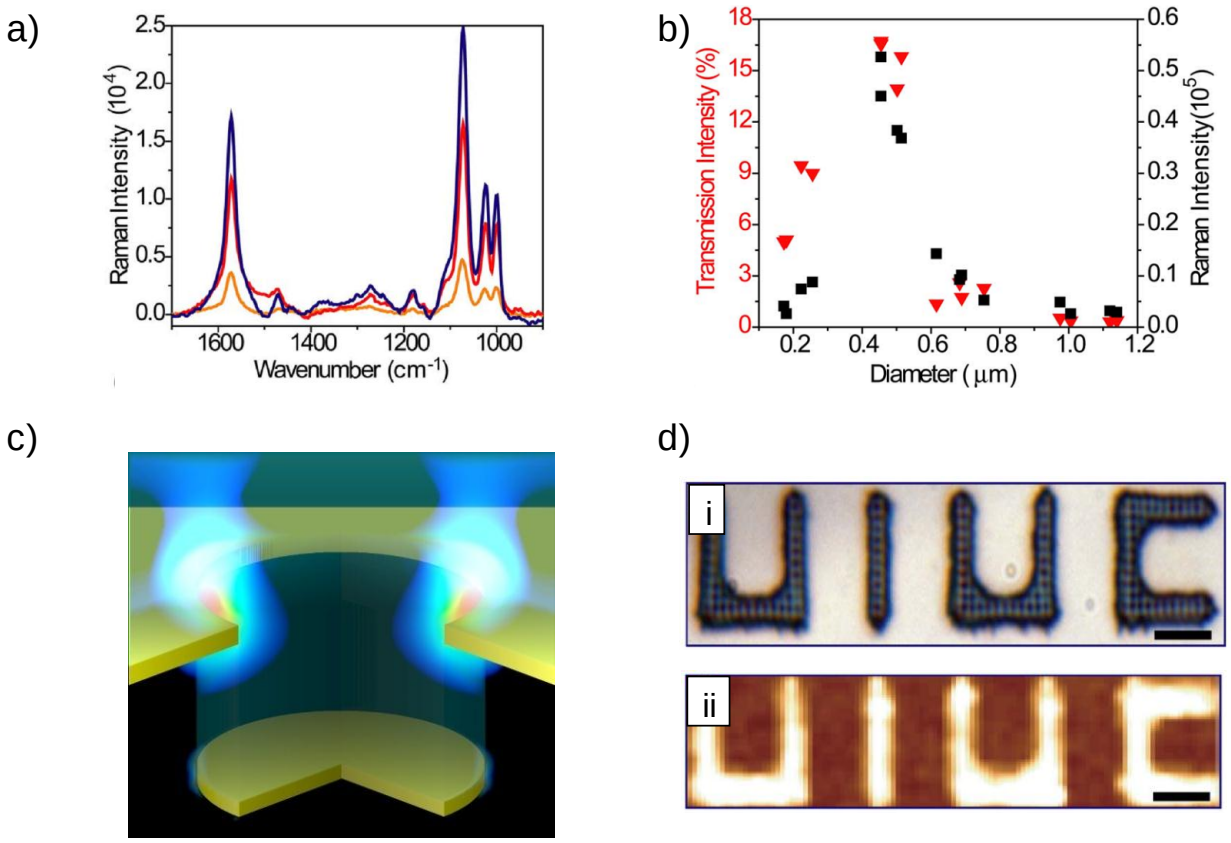

Figure 1.18 a) Raman spectra of benzenethiol monolayer on three quasi 3D nanohole plasmonic crystal with varying periodicity and hole diameter. b) Comparison of transmission intensity at 826 nm and intensity of Raman feature at 1087 cm^{-1} as a function of nanohole diameter (and periodicity). c) Electric field plot of transmission spectral feature at 826 nm computed using FDTD modeling. d) Optical image (*i*) of nanohole array embossed in photodefined SU-8 and SERS image (*ii*) of benzenethiol adsorbed onto the structure in (*i*). Scale bars are 5 μm. Figures reprinted with permission from [24]; Copyright 2009 American Institute of Physics

1.10 References

(1) Knoll, W. *Annu. Rev. Phys. Chem.* **1998**, *49*, 569.

(2) Ozbay, E. *Science* **2006**, *311*, 189.

(3) Raether, H. *Surface plasmons on smooth and rough surfaces and on gratings*; Springer Verlag: Berlin/Heidelberg/New York, 1988.

(4) Stewart, M. E.; Mack, N. H.; Malyarchuk, V.; Soares, J. A. N. T.; Lee, T.-W.; Gray, S. K.; Nuzzo, R. G.; Rogers, J. A. *Proc. Natl. Acad. Sci. USA* **2006**, *103*, 17143.

(5) Zhao, J.; Zhang, X.; Yonzon, C. R.; Haes, A. J.; Van Duyne, R. P. *Nanomedicine* **2006**, *1*, 219.

(6) Chau, L.-K.; Lin, Y.-F.; Cheng, S.-F.; Lin, T.-J. *Sens. Actuators B* **2006**, *113*, 100.

(7) Homola, J. *Chem. Rev.* **2008**, *108*, 462.

(8) Nelson, B. P.; Frutos, A. G.; Brockman, J. M.; Corn, R. M. *Anal. Chem.* **1999**, *71*, 3928.

(9) Wark, A. W.; Lee, H. J.; Corn, R. M. *Anal. Chem.* **2005**, *77*, 3904.

(10) Kretschmann, E.; Raether, H. *Z. Naturforsch. A* **1968**, *23*, 2135

(11) Otto, A. *Z. Phys.* **1968**, *216*, 398

(12) Homola, J. *Anal. Bioanal. Chem.* **2003**, *377*, 528.

(13) Nath, N.; Chilkoti, A. *Anal. Chem.* **2002**, *74*, 504.

(14) Barnes, W. L.; Dereux, A.; Ebbesen, T. W. *Nature* **2003**, *424*, 824.

(15) Barnes, W. L.; Murray, W. A.; Dintinger, J.; Devaux, E.; Ebbesen, T. W. *Phys. Rev. Lett.* **2004**, *92*, 107401.

(16) Ebbesen, T. W.; Lezec, H. J.; Ghaemi, H. F.; Thio, T.; Wolff, P. A. *Nature* **1998**, *391*, 667.

(17) Sherry, L. J.; Chang, S.-H.; Schatz, G. C.; Van Duyne, R. P.; Wiley, B. J.; Younan, X. *Nano Lett.* **2005**, *5*, 2034.

(18) Yonzon, C. R.; Jeoung, E.; Zou, S.; Schatz, G. C.; Mrksich, M.; Van Duyne, R. P. *J. Am. Chem. Soc.* **2004**, *126*, 12669.

(19) Stewart, M. E.; Anderton, C. R.; Thompson, L. B.; Maria, J.; Gray, S. K.; Rogers, J. A.; Nuzzo, R. G. *Chem. Rev.* **2008**, *108*, 494.

(20) Camden, J. P.; Dieringer, J.; Zhao, J.; Van Duyne, R. P. *Acc. Chem. Res.* **2008**, *41*, 1653.

(21) Gordon, R.; Sinton, D.; Kavanagh, K. L.; Brolo, A. G. *Acc. Chem. Res.* **2008**, *41*, 1049.

(22) Stuart, D. A.; Haes, A. J.; Yonzon, C. R.; Hicks, E. M.; Van Duyne, R. P. *IEE Proc.-Nanobiotechnol.* **2005**, *152*, 13.

(23) Willets, K. A.; Duyne, R. P. V. *Annu. Rev. Phys. Chem.* **2007**, *58*, 267.

(24) Baca, A. J.; Truong, T. T.; Cambrea, L. R.; Montgomery, J. M.; Gray, S. K.; Abdula, D.; Banks, T. R.; Yao, J.; Nuzzo, R. G.; Rogers, J. A. *Appl. Phys. Lett.* **2009**, *94*, 243109.

(25) Liebermann, T.; Knoll, W. *Colloid Surface A* **2000**, *171*, 115.

(26) Liebermann, T.; Knoll, W.; Sluka, P.; Herrmann, R. *Colloid Surface A* **2000**, *169*, 337.

(27) Ekgasit, S.; Stengel, G.; Knoll, W. *Anal. Chem.* **2004**, *76*, 4747.

(28) Yu, F.; Persson, B.; Lofas, S.; Knoll, W. *J. Am. Chem. Soc.* **2004**, *126*, 8902.

(29) Feller, B. E.; Kellis, J. T.; LCascao-Pereira, L. G.; Knoll, W.; Robertson, C. R.; Frank, C. W. *Langmuir* **2008**, *24*, 12303.

(30) Johansson, P.; Xu, H.; Käll, M. *Phys. Rev. B* **2005**, *72*, 035427.

(31) Kneipp, K.; Wang, Y.; Kneipp, H.; Perelman, L. T.; Itzkan, I.; Dasari, R. R.; Feld, M. S. *Phys. Rev. Lett.* **1997**, *78*, 1667.

(32) Michaels, A. M.; Jiang; Brus, L. *J. Phys. Chem. B* **2000**, *104*, 11965.

(33) Nie, S.; Emory, S. R. *Science* **1997**, *275*, 1102.

(34) Xu, H.; Bjerneld, E. J.; Käll, M.; Börjesson, L. *Phys. Rev. Lett.* **1999**, *83*, 4357.

(35) Xu, H. X.; Aizpurua, J.; Kall, M.; Apell, P. *Phys. Rev. E* **2000**, *62*, 4318.

(36) Dintinger, J.; Klein, S.; Ebbesen, T. W. *Adv. Mater.* **2006**, *18*, 1267.

(37) Przybilla, F.; Genet, C.; Ebbesen, T. W. *Appl. Phys. Lett.* **2006**, *89*, 121115.

(38) Bozhevolnyi, S. I.; Volkov, V. S.; Devaux, E.; Laluet, J.-Y.; Ebbesen, T. W. *Nature* **2006**, *440*, 508.

(39) Chang, C.-K.; Lin, D.-Z.; Yeh, C.-S.; Lee, C.-K.; Chang, Y.-C.; Lin, M.-W.; Yeh, J.-T.; Liu, J.-M. *Appl. Phys. Lett.* **2007**, *90*, 061113.

(40) Grand, J.; Adam, P.-M.; Grimault, A.-S.; Vial, A.; de la Chapelle, M. L.; Bijeon, J.-L.; Kostcheev, S.; Royer, P. *Plasmonics* **2006**, *1*, 135.

(41) Rechberger, W.; Hohenau, A.; Leitner, A.; Krenn, J. R.; Lamprecht, B.; Aussenegg, F. R. *Opt. Commun.* **2003**, *220*, 137.

(42) Henzie, J.; Lee, M. H.; Odom, T. W. *Nat. Nanotechnol.* **2007**, *2*, 549.

(43) Kwak, E.-S.; Henzie, J.; Chang, S.-H.; Gray, S. K.; Schatz, G. C.; Odom, T. W. *Nano Lett.* **2005**, *5*, 1963.

(44) Henzie, J.; Lee, J.; Lee, M. H.; Hasan, W.; Odom, T. W. *Annu. Rev. Phys. Chem.* **2009**, *60*, 147.

(45) Gao, H.; McMahon, J. M.; Lee, M. H.; Henzie, J.; Gray, S. K.; Schatz, G. C.; Odom, T. W. *Opt. Express* **2009**, *17*, 2334.

(46) X. Zhang; C. Yonzon; Duyne, R. P. V. *J. Mat. Res.* **2006**, *21*, 1083.

(47) X. Zhang; A. V. Whitney; J. Zhao; E. M. Hicks; Van Duyne, R. P. *J. Nanosci. Nanotechnol.* **2006**, *6*, 1920.

(48) Stiles, P. L.; Dieringer, J. A.; Shah, N. C.; Van Duyne, R. P. *Annu. Rev. Anal. Chem.* **2008**, *1*, 601.

(49) Bartlett, P. N.; Baumberg, J. J.; Coyle, S.; Abdelsalam, M. E. *Faraday Discuss.* **2004**, *125*, 117.

(50) Cintra, S.; Abdelsalam, M. E.; Bartlett, P. N.; Baumberg, J. J.; Kelf, T. A.; Sugawara, Y.; Russell, A. E. *Faraday Discuss.* **2006**, *132*, 191.

(51) Abdelsalam, M. E.; Mahajan, S.; Bartlett, P. N.; Baumberg, J. J.; Russell, A. E. *J. am Chem. Soc.* **2007**, *129*, 7399.

(52) Haynes, C. L.; Van Duyne, R. P. *J. Phys. Chem. B* **2001**, *105*, 5599.

(53) Yang, S.-M.; Jang, S. G.; Choi, D.-G.; Kim, S.; Yu, H. K. *Small* **2006**, *2*, 458.

(54) Prikulis, J.; Hanarp, P.; Olofsson, L.; Sutherland, D.; Kaell, M. *Nano Lett.* **2004**, *4*, 1003.

(55) Bukasov, R.; Shumaker-Parry, J. S. *Nano Lett.* **2007**, *7*, 1113.

(56) Stewart, M. E.; Motala, M. J.; Yao, J.; Thompson, L. B.; Nuzzo, R. G. *Proc. Inst. Mech. Eng. Part N: J. Nanoeng. Nanosyst.* **2007**, *220*, 81.

(57) Malyarchuk , V.; Hua, F.; Mack, N. H.; Velasquez, V. T.; White, J. O.; Nuzzo, R. G.; Rogers, J. A. *Opt. Express* **2005**, *13*, 5669.

(58) Truskett, V. N.; Watts, M. P. C. *Trends Biotechnol.* **2006**, *24*, 312.

(59) Yao, J.; Stewart, M. E.; Maria, J.; Lee, T.-W.; Gray, S. K.; Rogers, J. A.; Nuzzo, R. G. *Angew. Chem. Int. Ed.* **2008**, *47*, 5013

(60) Truong, T. T.; Maria, J.; Yao, J.; Stewart, M. E.; Lee, T.-W.; Gray, S. K.; Nuzzo, R. G.; Rogers, J. A. *Nanotechnol.* **2009**, *20*, 434011.

(61) Stewart, M. E.; Yao, J.; Maria, J.; Gray, S. K.; Rogers, J. A.; Nuzzo, R. G. *Anal. Chem.* **2009**, *81*, 5980.

(62) Malyarchuk, V.; Stewart, M. E.; Nuzzo, R. G.; Rogers, J. A. *Appl. Phys. Lett.* **2007**, *90*, 203113.

(63) Delamarche, E.; Schmid, H.; Michel, B.; Biebuyck, H. *Adv. Mater.* **1997**, *9*, 741.

(64) Hua, F.; Sun, Y.; Gaur, A.; Meitl, M. A.; Bilhaut, L.; Rotkina, L.; Wang, J.; Geil, P.; Shim, M.; Rogers, J. A. *Nano Lett.* **2004**, *4*, 2467.

(65) Odom, T. W.; Love, J. C.; Wolfe, D. B.; Paul, K. E.; Whitesides, G. M. *Langmuir* **2002**, *18*, 5314.

(66) Schmid, H.; Michel, B. *Macromolecules* **2000**, *33*, 3042.

(67) Truong, T. T.; Lin, R.; Jeon, S.; Lee, H. H.; Maria, J.; Gaur, A.; Hua, F.; Meinel, I.; Rogers, J. A. *Langmuir* **2007**, *23*, 2898.

(68) Rolland, J. P.; Hagberg, E. C.; Denison, G. M.; Cater, K. R.; DeSimone, J. M. *Angew. Chem. Int. Ed.* **2004**, *43*, 5796.

(69) Rothrock, G. D.; Maynor, B.; Rolland, J. P.; DeSimone, J. M. *Proc. SPIE* **2006**, *6152*, 61523F.

(70) Rolland, J. P.; Van Dam, R. M.; Schorzman, D. A.; Quake, S. R.; DeSimone, J. M. *J. Am. Chem. Soc.* **2004**, *126*, 2322.

(71) Yao, J.; Le, A.-P.; Gray, S. K.; Moore, J. S.; Rogers, J. A.; Nuzzo, R. G. *Adv. Mater.* **2010**, *22*, 1102.

(72) Maria, J.; Truong, T. T.; Yao, J.; Lee, T.-W.; Nuzzo, R. G.; Leyffer, S.; Gray, S. K.; Rogers, J. A. *J. Phys. Chem. C* **2009**, *113*, 10493.

(73) Hohng, S. C.; Yoon, Y. C.; Kim, D. S.; Malyarchuk, V.; Muller, R.; Lienau, C.; Park, J. W.; Yoo, K. H.; Kim, J.; Ryu, H. Y.; Park, Q. H. *Appl. Phys. Lett.* **2002**, *81*, 3239.

(74) Chaemi, H. F.; Thio, T.; Grupp, D. E.; Ebbesen, T. W.; Lezec, H. J. *Phys. Rev. B* **1998**, *58*, 6779.

(75) Chang, S.-H.; Gray, S. K.; Schatz, G. C. *Opt. Express* **2005**, *13*, 3150.

(76) Dahlin, A.; Zach, M.; Rindzevicius, T.; Kall, M.; Sutherland, D. S.; Hook, F. *J. Am. Chem. Soc.* **2005**, *127*, 5043.

(77) Hutter, E.; Fendler, J. H. *Adv. Mater.* **2004**, *16*, 1685.

(78) Taflove, A.; Hagness, S. C. *Computational Electrodynamics: The Finite-Difference Time-Domain*; Artech House: Boston, 2005.

(79) Mack, N. H.; Wackerly, J. W.; Malyarchuk, V.; Rogers, J. A.; Moore, J. S.; Nuzzo, R. G. *Nano Lett.* **2007**, *7*, 733.

(80) Lin, L.; Harris, J. W.; Thompson, G. R.; Brody, J. P. *Anal. Chem.* **2004**, *76*, 6555.

(81) Huang, T. T.; Sturgis, J.; Gomez, R.; Geng, T.; Bashir, R.; Bhunia, A. K.; Robinson, J. P.; Ladisch, M. R. *Biotechnol. Bioeng.* **2003**, *81*, 618.

(82) Mack, N. H.; Dong, R.; Nuzzo, R. G. *J. Am. Chem. Soc.* **2006**, *128*, 7871.

(83) Howell, E. In *Handbook of Raman Spectroscopy*; Lewis, I. R., Edwards, H. G. M., Eds.; CRC Press: 2001.

(84) Magde, D.; Wong, R.; Seybold, P. G. *Photochem. Photobiol.* **2002**, *75*, 327.

(85) Le Ru, E. C.; Blackie, E.; Meyer, M.; Etchegoin, P. G. *J. Phys. Chem. C* **2007**, *111*, 13794.

(86) Schatz, G.; Young, M.; Van Duyne, R. In *Surface-Enhanced Raman Scattering*; Kneipp, K., Moskovits, M., Kneipp, H., Eds.; Springer Berlin / Heidelberg: 2006; Vol. 103, p 19.

(87) Brolo, A. G.; Arctander, E.; Gordon, R.; Leathem, B.; Kavanagh, K. L. *Nano Lett.* **2004**, *4*, 2015.

(88) Haynes, C. L.; Van Duyne, R. P. *J. Phys. Chem. B* **2003**, *107*, 7426.

CHAPTER 2

Nanoimprinted Optical Fiber Microprobes for Surface-Enhanced Raman Scattering

2.1 Abstract

Development of surface-enhanced Raman scattering (SERS) based analyses has focused largely on the optimization of the plasmonic nanostructures which give rise to the surface enhancement but additional efforts are required to integrate these nanostructured materials into flexible systems capable of real-world analyses. A soft nanoimprint lithography technique was adapted for the facile fabrication of nanostructured plasmonic crystals directly on the tips of silica optical fibers using an inorganic spin-on-glass material for use as SERS optrodes. These nanoimprinted plasmonic substrates exhibited Raman enhancement in vastly different refractive index environment; the same design rule for the nanostructure architecture was capable of enhancing the Raman scattering from a benzenethiol monolayer in air as well as from Rhodamine 6G in aqueous solution. Strategies were developed to mitigate the impacts of Raman contributions from the silica fiber substrate itself, as were methods to incorporate the silica Raman signal as an internal standard to aid comparison. The fiber-based probe demonstrated stable Raman enhancements at high laser powers (~50 mW), and Raman scattering from silica was found to scale proportionally with that of the analyte. This combination of soft embossing, a fabrication method capable of rapid and inexpensive nanostructure generation, with optical fibers

substrates creates a versatile SERS sensing platform which can be readily generalized and optimized for the practical detection of analytes under real-world conditions.

2.2 Introduction

Surface-enhanced Raman scattering (SERS) is a vibrational spectroscopy technique capable of highly sensitive detection while providing chemically specific information, and these attributes make it very attractive for potential environmental monitoring applications (such as the detection of explosives or biological agents).[1,2] In fact, this analytical technique has experienced a Renaissance of sorts in recent years as nanofabrication methods capable of creating Raman-enhancing structures with precisely defined shapes and sizes have matured. Considerable effort has been invested in maximizing the enhancement factor achievable using various nanoparticle assemblies and nanostructured surfaces, and detections down to single molecule levels have been reported in the literature.[3-7] Although high performance substrates are a necessity for the continued development of SERS applications, they are unlikely to see widespread adoption for real-world analyses without additional effort invested towards the integration of these Raman-enhancing substrates into versatile analytical systems that can be inexpensively fabricated and implemented.

Optical fiber-based systems have previously been integrated for use in handheld Raman spectrometers, and these fibers bear significant advantages for real-world applications of both standard as well as surface-enhanced Raman spectroscopy.[8,9] The optical fiber itself allows the sampling element to be separated from the illumination source and detector, providing flexibility in the physical configuration of the instrument. The laser illumination is confined within the fiber, reducing the risk of inadvertent exposure as well as simplifying the optical arrangements

required to steer the beam towards the sample. The small diameter of optical fibers along with the chemical stability of the silica substrate could potentially enable direct Raman sensing in hazardous, remote, or (relatively) inaccessible environments. Optical fibers could even be embedded in materials to probe the chemical nature of a sample in areas away from the surface, such as within biological tissues for *in situ* diagnostics.

Despite these advantages, the adoption of optical fiber probes for Raman spectroscopy is limited chiefly by Raman scattering from the silica in the fiber itself.[8,10] The incident laser light used to generate Raman-scattered photons from the analyte also generates Raman-scattered photons from the optical fiber; although the Raman scattering from silica is relatively weak, the comparatively large amounts of silica fiber in the probe result in large effective scattering volumes. The silica Raman scattering leads to a large background in the Raman spectrum, and this background can easily swamp the Raman signal from the analyte of interest.

Fiber optic probes for standard Raman spectroscopy have been engineered to circumvent this silica Raman background limitation by separating the probe's two functions: delivery of the laser illumination and collection of the Raman signal from the analyte.[11] By separating these functions into separate fibers, bandpass filters can be incorporated into the probe design. Filters on the illumination fibers rejects the Raman-scattered photons generated as the laser excitation travels through the fiber to the sample, and filters on the collection fibers reject any laser light reflected by the sample. While this arrangement of fibers has proven to be successful at markedly reducing the silica Raman background, the complexities associated with bundling of the fibers and incorporation of the filters precludes the ultimate goal for optical fiber Raman probes, where the same fiber is used to both illuminate the sample as well as deliver the Raman scattered photons to the detector in the so-called 'optrode' configuration.

The discovery of enhanced Raman scattering from molecules interacting with roughened or patterned metal surfaces has broadened interest in the use of this vibrational spectroscopy technique.[1,12,13] The source of this enhanced Raman scattering is generally attributed to the presence of nanoscale metallic features capable of supporting localized surface plasmon resonances which generate evanescent electric fields that assist in the coupling of photons into and back out of the analyte.[1,14] The nanostructured metal features capable of producing this surface-enhanced Raman scattering have generally used gold or silver and come in many different forms, including individual nanoparticles of different shapes, nanoparticle assemblies as well as nanostructured metal films.[15] The advent of SERS has sparked a rebirth in the investigation of optical fiber based systems for Raman spectroscopy. The integration of metallic nanostructures with the optical fiber could sufficiently increase the Raman scattering intensity of the analyte such that the Raman signal from the analyte can be detected over the silica Raman background. In short, these Raman-enhancing nanostructures could become an enabling technology for the successful development of single-fiber SERS probes.

A number of different routes have been demonstrated for the fabrication or assembly of plasmonic nanostructures on optical fibers. One class of methods involves the assembly or growth of nanoparticles or nanorods on the optical fiber.[16-21] The optical fiber tip can be roughened by ablating the surface using a femtosecond laser, generating roughened areas across the fiber tip onto which silver or gold nanoparticles can be created or adsorbed.[22,23] An alternative method has been to chemically etch the cylindrical fiber to a tapered shape, increasing the exposed surface area through which light can escape the fiber into the surroundings; silver nanoparticles or islands are deposited along the length of this taper to complete the SERS probe.[24-26] While synthetic methods are capable of producing nanoparticles of monodisperse size

distributions, the assembly of the nanoparticles on the fiber surface is, for the most part, random. Furthermore, the fiber treatments used (femtosecond laser ablation, chemical etching) add complexity to the fabrication process.

The second class of techniques for creating SERS fiber probes generates deterministic nanostructures directly on the optical fiber surface. Focused ion beam milling has been the prevalent method for writing such structures, and arrays of nanostructures with arbitrary sizes and shapes have been successfully created on optical fiber faces.[27,28] More recently, electron beam lithography has been employed to produce nanostructured surfaces via a two step process; arrays of structures such as nanoantennas are written on a separate substrate via electron beam lithography, and these structures are transferred onto the optical fiber tip in a second step using decal transfer lithography.[29] While both of these methods have been successfully employed to create nanostructured optical fiber surfaces, writing of the nanostructures is a generally slow process that is difficult to perform in parallel, limiting the rate at which patterned substrates can be produced. Additionally, these milling methods are limited in the overall pattern size they can write in a single step, although the substrate can be physically displaced to write a pattern over large areas. An inexpensive fabrication technique that could precisely replicate nanoscale features over large areas (> 100 μm in diameter) directly on the optical fiber tip would greatly enhance the feasibility of optical fiber-based SERS sensing.

In this work, we have fabricated nanostructured plasmonic crystals directly on the tips of optical fibers using soft nanoimprint lithography for use as SERS fiber probes.[30-33] Photolithography is used to generate a nanostructured master pattern, and a poly(dimethyl siloxane) (PDMS) stamp cast from this master is subsequently used to mold this pattern with high fidelity and nanometer-scale resolution. This soft embossing technique is capable of rapidly

replicating deterministic arrays of nanoscale features directly on the optical fiber tip using inexpensive materials. While the use of single optical fibers in Raman sensing applications entails the presence of the silica Raman background, we show that this background is not an impediment to detection of the Raman scattering for benzenethiol monolayers as well as that for Rhodamine in aqueous solution, which is indeed enhanced by the nanopatterned optical fiber tip. The soft embossing of nanostructures coupled with a single optical fiber configuration mode creates a versatile SERS sensing platform that can be readily adapted and optimized for different sensing environments.

2.3 Experimental Materials and Methods

2.3.1 Reagents

All reagents were used as received without further purification unless otherwise noted. Spin-on-glass (product number 314) was purchased from Honeywell and filtered using a 0.02 μm syringe filter immediately before use. Polydimethylsiloxane (soft PDMS; Sylgard 184, Dow Corning) was purchased from Ellsworth Adhesives. Hard PDMS components: poly(7-8% vinylmethylsiloxane)-(dimethylsiloxane) (VDT-731); 1,3,5,7-tetravinyl-1,3,5,7-tetramethylcyclotetrasiloxane(SIT-7900); poly(25-30% methylhydrosiloxane)-(dimethylsiloxane) (HMS-301); platinum-divinyltetramethyldisiloxane (SIP6831.1); and (tridecafluoro-1,1,2,2-tetrahydrooctyl)trichlorosilane (‘no-stick treatment’) were purchased from Gelest. Rhodamine 590 chloride was purchased from Exciton. Benzenethiol (thiophenol) was purchased from Sigma Aldrich. Low-OH, step-index multimode optical fiber (200 um diameter,

0.22 NA, product no. BFL22-200) was purchased from Thorlabs. Ultrapure water (18 MΩ) was produced using a Millipore Milli-Q Academic A-10 system.

2.3.2 Soft Embossing of Plasmonic Nanostructures on Optical Fiber Tips

The plasmonic nanostructures imprinted onto the fiber tip consist of a square array of nanoholes originally created photolithographically on a silicon wafer in photoresist.[31-36] This plasmonic crystal pattern was replicated in a siloxane-based spin-on-glass (SOG) cast onto a glass microscope slide via a soft nanoimprint lithography process previously described;[31] this glass-slide based plasmonic crystal replica was itself used as a replication master for the casting of composite hard-PDMS/soft-PDMS stamps which were subsequently used to pattern the optical fiber tips. A 'no-stick' treatment was applied to the composite PDMS stamps prior to use using previously described methods.[34]

Optical fiber probes were prepared by cutting portions of desired length, followed by removal a portion of the polymer coating from the fiber using a Micro-Strip stripping tool (Micro Electronics, Inc.) with blades appropriately sized to the diameter of the fiber and coating. The stripped portion of the fiber was wiped with a methanol-dampened Kimwipe to remove any residual debris, and smooth fiber faces were cut on each end of the fiber using a mechanical fiber cleaving tool (Fujikara High Precision Fiber Cleaver, product no. CT-04B). Debris was blown off the fiber ends using compressed nitrogen gas, and the fiber face was found to be sufficiently smooth for imprinting; no further polishing of the cleaved fiber end was performed.

After the fiber tips were cleaved, the fiber was inserted into a UV-ozone cleaning chamber (UVOCS) for five minutes, and the fiber was then fastened onto a vertically mounted translation stage using double-sided tape. A photograph of this apparatus is presented in Figure

2.1a, and Figure 2.1b-e present a schematic overview of the nanoimprint lithography process used to pattern the optical fiber tips. The SOG sol was filtered through a 0.02 μm syringe filter to remove any particulates present, and a drop of the SOG sol was formed at the tip of a syringe needle and brought to the tip of the optical fiber to transfer a thin film of the sol to the tip of the optical fiber. The composite PDMS stamp was placed above the fiber tip (Figure 2.1b), and the translation stage was used to controllably push the optical fiber into the stamp surface (Figure 2.1c). This assembly (fiber, stamp, and stage) was placed into an oven at 110°C for 3 minutes, after which the fiber was then removed from the stage and the stamp (Figure 2.1d). The fiber was then placed into the oven and baked at 200°C for 5 minutes and then held overnight at 150°C to thermally cure the nanoimprinted plasmonic structures on the optical fiber tip. The plasmonic crystal patterned on the optical fiber had a periodicity of ~740 nm (hole center-to-hole center), individual nanohole diameters of ~440 nm, and relief depths of ~300 nm. An adhesion layer (5 nm TiO_2) and a metal layer (50 nm Au) were deposited onto the patterned tips of the optical fibers using an electron-beam evaporator (Temescal) to complete the fabrication of the plasmonic crystal (Figure 2.1e).

2.3.3 Characterization of Plasmonic Nanostructures on Optical Fiber Tips

Several imaging methods were employed to assess the replication fidelity of the nanostructures embossed on the optical fiber tips. Darkfield microscopy was performed using an ausJena Jenavert upright optical microscope with a 12.5×, 0.25 NA objective; the microscope was equipped with a darkfield condenser and a white light halogen illuminator. Darkfield images were captured using an Infinity 1-3C complementary metal-oxide-semiconductor (CMOS) digital camera (Lumenera Scientific) mounted on the microscope.

Scanning electron microscopy (SEM) was performed using a JEOL 6060-LV scanning electron microscope operated in high vacuum mode; while the tip of the optical fiber was coated with a thin film of gold, an additional thin film of Pd/Au was sputtered onto the fiber after it had been mounted on a sample stub to render the entire assembly electrically conductive. Atomic force microscopy (AFM) measurements were performed using an Asylum Research MFP-3D atomic force microscope operated in tapping mode. Collection of the SEM and AFM images required the nanostructured tip to be separated from the rest of the optical fiber in order for the sample to physically fit within the instruments; this was achieved by using a razor blade to cut through the silica fiber. Further preparation was necessary for the AFM measurements: the nanostructured fiber tip was embedded in an epoxy adhesive in order to mount in vertically on a glass microscope slide; once cured, the epoxy provided a rigid matrix to prevent the optical fiber from moving or deflecting during the measurement. Analyses of the darkfield and SEM images were performed using ImageJ, while analysis of the AFM data was performed using IgorPro and the Asylum Research AFM software.

2.3.4 Surface-Enhanced Raman Spectroscopy of Adsorbed Benzenethiol Monolayers and of Rhodamine Solutions

SERS spectra were collected using a Bruker SENTERRA dispersive Raman microscope with a 20× objective and a 785 nm fiber-coupled diode laser. The Raman spectra were collected over a range of Raman shifts between 400 – 2000 cm^{-1}. The optical fiber probe was mounted in a chuck such that the incident laser illumination entered the fiber through the distal (non-patterned) end. All Raman spectra were collected using 30 s signal integration times. Raman data analysis, including background fitting and subtraction, was performed using OriginPro.

A self-assembled monolayer of benzenethiol was adsorbed onto the optical fiber probes (~10 cm in length) by immersing the metalized, patterned tips in a 15 mM solution of benzenethiol in ethanol overnight. Following formation of the benzenethiol monolayer, the fiber tips were removed from the benzenethiol solution, rinsed thoroughly with ethanol, and dried with compressed nitrogen gas.

SERS measurements of Rhodamine were collected using a 20 μM solution of Rhodamine 590 chloride was prepared in ultrapure water. A 785 nm diode laser with a power of 50 mW was used to illuminate the optical fiber probe. Plasmonic nanohole arrays were patterned onto the tips of optical fibers (approximately 1 m in length) as previously described, and the nanostructured fiber tip was inserted into the Rhodamine solution immediately prior to collection of the Raman spectrum and remained immersed for the duration of the measurement.

2.4 Results and Discussion

2.4.1 Soft Embossing of Plasmonic Nanostructures on Optical Fiber Surfaces

Inorganic, siloxane-based spin-on-glass materials (SOG) have been previously adapted for use as an embossing material, and plasmonic crystals molded in SOG exhibited improved SERS enhancements compared to equivalent structures molded in organic materials such as a photocurable polyurethane or an epoxy-based photoresist.[31] The SOG material also exhibits chemical stability in a wide range of environments, which could be advantageous for sensing applications in oxidizing or corrosive environments. The optical properties of the SOG material itself combined with its improved resistance to thermally-induced deformation are believed to be responsible for the improved enhancement, which is a desirable design element for these optical

fiber probes. Additionally, it was shown that the spectral properties of SOG-based plasmonic crystals can be tuned through control over the fabrication conditions (although this was not explored in the present work).

Plasmonic nanohole arrays were replicated on the surface of the optical fibers using a soft nanoimprint lithography method, and representative images of the nanostructures patterned on the optical fiber tip are presented in Figure 2.2. The large-area scanning electron microscopy image in Figure 2.2a reveals that the nanostructures are patterned across the entire optical fiber tip; the core of the optical fiber is 200 μm in diameter with a 20 μm cladding layer surrounding the core. A higher magnification SEM image of the outer edge of the fiber tip is presented in Figure 2.2b which shows that the nanoholes were uniformly formed across the bulk of the surface, although they did become less consistent approaching the edge of the fiber. These distortions were attributed to a 'squeezing out' of the spin-on-glass sol as the fiber tip was pressed into the composite PDMS stamp. This should only have a limited impact on the performance of the SERS fiber microprobe as the photon flux at the fiber edges is smaller than towards the center of the fiber. Furthermore, a 20 μm thick cladding layer is present around the periphery of the fiber, and the distorted nanostructures lie predominantly in this region.

A darkfield microscopy image is shown in Figure 2.2c, and this image generally shows a lack of defects in the patterned nanostructures just as the SEM image in Figure 2.2a. The nanohole topography was mapped using atomic force microscopy, and an inverted 3D projection of the AFM data is presented in Figure 2.2d. This projection reveals uniform nanohole relief depths (~340 nm in this case), and the nanostructure replication quality shown here is consistent with that demonstrated previously for soft lithography using spin-on-glass. These images provide evidence for the suitability of soft nanoimprint lithography techniques for the replication

of nanoscale features on challenging substrates, and the nanostructures patterned here are produced relatively quickly – the molding time required was approximately 3 minutes, although the spin-on-glass is cured overnight in an oven.

Initial trials for the imprinting of SOG on the optical fiber tip resulted in anomalous behavior not previously observed when molding SOG on glass microscope slides. One such defect is depicted in Figure 2.3a-c where large areas of the nanostructured SOG film appear to have lifted off from the optical fiber. (No gold had been deposited onto the optical fiber tips when the darkfield images in Figure 2.3 were acquired, and only a thin film of Pd/Au was deposited on them to enable the SEM imaging.) In fact, examination of the higher magnification SEM image in Figure 2.3c reveals that the areas where the SOG pattern lifted off are not entirely empty. Small squares which appear to correspond to the area between four nanoholes were left behind, and the nanostructure loss appeared to follow the cardinal directions of the square array.

This behavior may be the result of poor adhesion of the SOG to the silica fiber substrate as well as unexpectedly strong adhesion between the SOG and the composite PDMS stamp, and the fabrication procedures were altered to exert better control over these adhesive properties: A fluorinated no-stick coating was covalently bound to the PDMS stamp surface to decrease the apparent affinity between the SOG sol and the stamp itself.[34] The surface of the optical fiber tip was exposed to ultraviolet light and ozone gas to activate the silica surface, generating surface silanol groups with the hopes of generating covalent bonds between the silica surface and the siloxane-based SOG.[37,38] After this procedural modification, no further occurrences of this nanostructure 'lift-off' was observed.

An additional difficulty encountered in the fabrication of SOG-based nanostructures on the optical fiber surface was cracking of the SOG film, an example of which is shown in Figure

2.3d-f. The high magnification SEM image in Figure 2.3f shows that the nanostructures themselves are properly molded in the SOG film, but the cracks observed in the film appeared only after heating of the fiber and SOG to cure the nanostructured film. The high magnification SEM image also suggests that portions of the SOG film have also lifted off of the surface, suggesting again that the adherence of the SOG film to an otherwise untreated silica fiber surface was poor. These raised areas scatter light more effectively than the surrounding region and led to the anomalously bright areas observed in the darkfield image of the patterned fiber tip (Figure 2.3d). The particular spin-on-glass used to fabricate these nanostructures has an intended thickness range between 220 nm and 360 nm,[39] and the cracking may be a result of a SOG film that was too thick. The fabrication procedure was modified to limit the total amount of SOG applied to the fiber by suspending a droplet of the filtered SOG sol on the tip of a syringe needle and dabbing the droplet onto the tip of the optical fiber after it had been mounted on the translation stage. Combined with the surface treatments previously described, these procedural changes largely eliminated the fabrication defects shown in Figure 2.3, and highly uniform nanostructures could be successfully replicated in SOG on the optical fiber tip as demonstrated in Figure 2.2.

The images in Figure 2.2 and Figure 2.3 also demonstrate the utility of darkfield microscopy in the evaluation of the nanoimprinting quality. Due to space limitations within the SEM and AFM sample chambers, the nanostructured optical fiber tips had to be separated from the rest of the fiber for them to fit. While these imaging methods themselves do not damage the nanostructured surfaces, they are, in fact, destructive from the standpoint of the ability to use the optical fiber probe after imaging. In contrast, the optical fiber tip can be imaged under a darkfield microscope (provided sufficient space is available underneath the microscope stage)

without destroying the utility of the probe itself, and the darkfield images readily reveal the same gross structural defects as those found in the SEM images. Furthermore, fiber tips can be examined more rapidly under a darkfield microscope, making this an attractive method for judging the broader qualities of the replicated nanostructures prior to continued processing.

2.4.2 SERS Measurements of Adsorbed Benzenethiol Self-Assembled Monolayers Using Nanostructured Optical Fiber Microprobes

SERS measurements were made using gold-coated optical fiber microprobes mounted within a Raman microscope in an optrode configuration; a block diagram of the optical setup is provided in Figure 2.4. Excitation light from a 785 nm diode laser is focused through the microscope objective onto the distal end of the optical fiber probe – that is, the light is incident on the end of the optical fiber opposite from the nanostructured tip. The excitation light propagates down the fiber to reach the metalized, nanostructured tip; and these photons interact with the structured metal surface and nearby analytes. Only Raman photons scattered back towards the metal surface and optical fiber at angles within the acceptance range of the fiber can be collected for analysis. These Raman scattered photons propagate back through the optical fiber and are collected by the microscope objective and passed to the detector; a dichroic mirror is used to filter the Raman scattered photons from laser light that were reflected back through the fiber. The optrode configuration used in this experiment is remarkably simple to assemble – the optical fiber is inserted into a fiber chuck to mount it underneath the microscope objective, and only a single alignment/focusing step is required prior to use.

A characteristic raw Raman spectrum for benzenethiol adsorbed onto a patterned optical fiber tip is presented as the black curve in Figure 2.5a, and this spectrum exhibits a non-constant

baseline which increases at smaller Raman shifts. In order to flatten this baseline, an exponential decay function of the form $y = y_0 + A_1 e^{-x/t_1} + A_2 e^{-x/t_2}$ was fit using OriginPro to approximate its shape, and the resulting calculated baseline is included in Figure 2.5a as the red curve in the plot. It should be noted that while the shape of this baseline appears to be a good fit for the baseline at Raman shifts greater than ~550 cm^{-1}, but the exponential function is clearly invalid for the portion of the spectrum with Raman shifts of less than ~500 cm^{-1}. The Raman bands of interest for benzenethiol in this work are at larger Raman shifts (greater than 1000 cm^{-1}), so this limitation in the baseline fitting was acceptable. All subsequent Raman spectra have been baseline subtracted in this manner.

The resulting Raman spectrum after baseline subtraction is presented in Figure 2.5b, and this spectrum is actually a convolution of two individual spectra, one of benzenethiol and one of silica. Although silica is a relatively weak Raman scatterer, the sheer length of fiber through which the excitation laser must pass results in a sizable Raman contribution that can swamp Raman signals coming from the analyte of interest; this has previously been a limiting factor in the use of the optrode configuration for Raman fiber probes despite the simplified optical setup. The Raman signal for silica appears as the peaks centered around 500 cm^{-1}, 600 cm^{-1} and 800 cm^{-1} as well as the broader features at ~1050 cm^{-1}, 1200 cm^{-1}, and ~1600 cm^{-1}. (The peak at 500 cm^{-1} is not as well defined as those at 600 cm^{-1} and 800 cm^{-1} because of the imperfect baseline subtraction at smaller Raman shifts.) The Raman spectrum for benzenethiol is overlaid on top of the silica spectrum as the triplet of peaks between 1000 – 1100 cm^{-1} as well as the peak around 1570 cm^{-1}, and this SERS spectrum for benzenethiol is in good agreement with those previously reported in the literature.[33,40-42]

The Raman data were processed further by normalizing the intensity of the baseline-subtracted spectra to the intensity of the silica peak at ~600 cm^{-1} such that it was assigned an arbitrary value of 100. (This peak at ~600 cm^{-1} for silica is reported in the literature as the D_2 'defect' line, and computational simulations associate this spectral feature with a coherent breathing mode for a ring consisting of three Si-O units in vitreous silica.[43]) This peak was chosen to act as an internal standard to help compensate for deviations in the spectra, such as those related to laser intensity fluctuations, resulting in more meaningful comparisons.

Figure 2.6 presents a comparison of the normalized Raman spectra for a benzenethiol monolayer adsorbed onto the tip of an embossed optical fiber (red curve) and onto the tip of an unstructured, flat optical fiber (black curve); both optical fiber tips were otherwise prepared in the same manner. The unstructured control spectrum (black curve) clearly shows the silica Raman peaks, but the benzenethiol Raman contribution is absent – this is easily seen by comparing it to the Raman spectrum acquired using the nanostructured optical fiber (red curve). This control comparison clearly indicates that the Raman signal from benzenethiol is enhanced by the plasmonic nanostructures embossed on the tip of the optical fiber. Furthermore, the benzenethiol Raman signal is distinguishable from that of silica, even in regions of spectral overlap (*e.g.* 1000 – 1100 cm^{-1}). The silica background signal was previously considered an impediment in the development of fiber optic Raman probes, and while that background is still present, these experimental results suggest that enhancement of the Raman signal via a nanoimprinted plasmonic crystal on the fiber tip makes this optrode configuration feasible.

2.4.3 Normalized Raman Intensity Dependence on Excitation Laser Power

One strategy for increasing the Raman scattering signal of an analyte has been to increase the excitation laser power, and this has previously been accomplished in optical fiber probe designs using so-called '*N*+1' fiber bundles, where one fiber is used to collect the Raman scattered photons while a group of *N* optical fibers arranged around the collection fiber delivers the excitation illumination.[11] While the optrode configuration used in this experiment obviates the need for separate optical fibers to transport the excitation light, higher laser powers could still be used to increase the Raman signal from analytes at the probe tip. However, increased laser power would be expected to generate a larger background signal from the silica fiber itself; experiments were performed using a single optical fiber probe to investigate the dependence on excitation intensity on the Raman scattering of both benzenethiol adsorbed on the optical fiber tip and silica in the fiber.

Figure 2.7a presents the baseline-flattened Raman spectra from a single patterned optical fiber using different excitation powers: 1 mW, 10 mW, 25 mW, 50 mW, and 100 mW. As expected, the Raman intensities for both the silica and the benzenethiol bands increased as the excitation power was increased. While this comparison of laser powers demonstrates that higher laser fluences can indeed be utilized to increase the Raman scattering intensity, more interesting behavior is observed after normalizing the Raman spectra to the intensity of the silica band at ~600 cm^{-1}. These normalized Raman spectra are shown in Figure 2.7b, and an examination of the benzenethiol features reveals that their normalized intensity remains largely the same, independent of the incident laser power. A more quantitative comparison is made for the normalized intensity of the benzenethiol peak at ~1570 cm^{-1}, and the normalized peak height for

this feature displayed on the graph for each incident laser power. (This peak, corresponding to a C-C stretching mode of the benzene ring, was chosen for comparison between the spectra because its intensity is readily distinguished from the small, broad silica band in the same spectral region that was observed in the control spectrum in Figure 2.6.[8,42]) As the laser power is increased from 1 mW to 50 mW, the normalized intensity of the benzenethiol peak at ~1570 cm^{-1} remains approximately constant. Put another way, the absolute peak intensities of the silica feature at ~600 cm^{-1} and the benzenethiol feature at ~1570 cm^{-1} increased with the laser power (as seen in Figure 2.7a), but the *relative* peak intensities did not.

At the highest laser power investigated here (100 mW), the normalized intensity of the benzenethiol peak was smaller than it was at lower laser powers, and this is likely due to several factors related to the heat generated at the optical fiber tip by the incident laser. Localized heating of the metalized tip could cause thermal desorption of the benzenethiol, resulting in decreased analyte coverage of the surface with a corresponding drop in signal. Additionally, heating of the tip could cause deformation or damage to the gold film – this has been observed previously in both inorganic SOG-based and organic polymer-based plasmonic crystals used for SERS measurements of benzenethiol.[31] Heating of the metal film could result in annealing or melting of the film, resulting in distortions which would alter the plasmonic properties of the metal layer and the ability of the plasmonic nanostructure to successfully enhance the Raman scattering from benzenethiol. (It should be noted that previous investigations have found that the underlying SOG nanostructures themselves were not deformed by the heating – in these measurements, the stability of the plasmonic substrate is limited by the stability of the metal film itself.)

In fact, thermal damage to the nanostructured optical fiber tip was observed after some measurements. Figure 2.8a presents a darkfield microscopy image of a fully fabricated optical fiber tip after a benzenethiol monolayer was adsorbed onto the gold-coated surface, and Figure 2.8b is a darkfield image of the same optical fiber tip after Raman measurements were collected. The post-measurement image clearly shows discoloration and damage to regions of the nanostructured surface which were induced during the measurement. Greater heating of the optical fiber tip in Raman applications has been previously reported and is attributed, in part, to poorer thermal conductivity from the metal surface in this configuration.[8] The specific conditions leading to damage and discoloration at the metalized tip are not currently well understood, but the patterned nanostructure dimensions may play a role in the metalized tip's susceptibility to heating-related deformation.

2.4.4 Corrections for Silica Contributions to the Raman Signal

Assuming there is no interaction between benzenethiol and the silica fiber substrate, the Raman spectra should be the result of the additive overlap of the non-enhanced Raman scattering of silica from the fiber, the enhanced Raman scattering from benzenethiol at the probe surface, and Raman scattering from silica at the fiber tip which is enhanced because of its close proximity to the nanostructured metal surface. If the scattering intensity of the analyte is low compared to that of silica at the same Raman shift, the analyte signal may be swamped by the silica signal, and corrections to the spectra to remove the silica Raman contributions can render the analyte signal distinguishable once again.

Previous studies of optical fiber-based SERS probes have collected the Raman spectrum of the fiber probe itself first, without any analyte, and this background spectrum is subtracted

from the experimental spectrum when the analyte is present in order to remove both the enhanced and non-enhanced Raman scattering of silica.[29] While this method is effective at removing the silica Raman signal, effective implementation of this correction requires the ability to collect the reference spectrum under the same experimental conditions; the optical properties of plasmonic substrates can change depending on the environment. This may not be feasible for all applications, and retaining a portion of the silica Raman signal could prove advantageous for use as an internal standard for quantitative measurements.

We have investigated an alternate correction method to remove only the non-enhanced Raman contributions from the silica fiber. Raman spectra for benzenethiol adsorbed onto a nanopatterned optical fiber probe were collected as portions of the fiber were cut off, resulting in a decrease in the silica Raman signal as the optical fiber became shorter. The raw Raman spectra of the shortened optical fiber probes were subtracted from that of the original spectrum (obtained for the full-length fiber probe) and then normalized against the total length of fiber that had been removed. A comparison of these length-normalized Raman spectra (after baseline flattening) is presented in Figure 2.9a, and these spectra show remarkable consistency. The lack of distinguishable peaks corresponding to benzenethiol in these difference spectra suggests that this approach is indeed capable of separating the non-enhanced Raman signal from the surface-enhanced Raman components.

An average Raman contribution per unit length of silica fiber was calculated using these length-normalized spectra and was subtracted from the Raman spectrum obtained using the full-length fiber probe. The original Raman spectrum and the resulting spectrum after application of this correction for non-enhanced silica Raman scattering are presented in Figure 2.9b. (These spectra have been normalized such that the intensity of the residual silica peak at 600 cm^{-1} is

once again assigned a value of 100.) The triplet of benzenethiol peaks can be inferred in the original Raman spectrum (black curve) between 1000 – 1100 cm^{-1}, but individual peaks clearly cannot be resolved from the silica feature in the same spectral region. After subtraction of the silica fiber contribution, these three benzenethiol peaks were recovered and can be readily identified. Additionally, the normalized benzenethiol peak intensity at ~1570 cm^{-1} increased by ~15% after the silica subtraction was performed; this result is expected as the Raman intensity of the silica reference peak would have decreased after subtraction.

It is curious, however, that the relative intensities of the different Raman bands associated with silica were not equally affected by the subtraction. The relative intensity of the silica peak at 800 cm^{-1} (compared to that at 600 cm^{-1}) decreased, while the silica peaks between 1000 – 1200 cm^{-1} as well as the broad feature at centered around 1600 cm^{-1} appear to have been completely removed. The Raman peak at 600 cm^{-1} is associated with a 'defect' mode consisting of a ring formed by three Si—O pairs,[43] while the Raman peaks at 800 cm^{-1}, 1000 – 1200 cm^{-1}, and 1600 cm^{-1} are vibrations and overtones for vibrations associated with SiO_4.[44] This suggests underlying differences between the enhancements (or lack thereof) for the different silica Raman modes.

Given these identifications, it is perhaps less surprising differences are observed in the silica Raman subtraction. The very presence of the surface disrupts the covalent bonding network in silica, reducing the number of silicon atoms bonded to four other oxygen atoms at the surface and necessarily reducing the potential for the Raman signal from these groups to be enhanced by the plasmonic nanostructure at the fiber tip. Thus, it is reasonable that the Raman signal observed at Raman shifts greater than 800 cm^{-1} are largely the result of scattering from the bulk of the fiber and would be adequately removed using the correction method. The conservation (at least in part) of the defect band for silica at 600 cm^{-1} suggests that this Si-O ring

structure is present at the surface (and thus enhanced by the nanostructured tip) as well as in the bulk of the fiber; this latter point is seen as the presence of the peak at 600 cm^{-1} in the non-enhanced Raman spectra shown in Figure 2.9a.

2.4.5 SERS Measurements in Aqueous Rhodamine Solutions Using Optical Fiber Probes

Optical fiber SERS probes would be particularly well-suited for solution-based measurements as solutions could be remotely probed with little need for sample collection or preparation. Additionally, the solution could itself act as a heat sink, reducing the occurrence of heating related damage of the nanostructured metal film. Nanoimprinted optical fibers were thus used to probe solutions of Rhodamine 6G dissolved in water as a test system.

Longer optical fibers were used in these measurements (1 m vs. 10 cm used in the benzenethiol measurements), and a comparison of Raman spectra collected using a nanostructured optical fiber and a flat control fiber is presented in Figure 2.10a. (While only the structured fiber has the embossed nanohole array, both fiber tips were coated with 50 nm of gold.) Again, both spectra are dominated by the Raman features associated with silica, but a closer examination of the Raman spectra between 1300 – 1800 cm^{-1} reveals the presence of additional Raman features in the spectra obtained using the nanostructured optical fiber probe. A magnified view of the Raman spectra in this region are presented in Figure 2.10b. The small peaks at ~1310 cm^{-1}, 1360 cm^{-1}, 1500 cm^{-1}, 1600 cm^{-1}, and 1650 cm^{-1} have previously been assigned to vibrational modes of Rhodamine 6G and are entirely unresolved in the control spectrum.[45,46]

While the normalized intensities of the Rhodamine peaks are small, these results do show that the nanostructures on the optical fiber tips produce an enhancement of the Raman signal.

Several opportunities exist to significantly increase the performance of these fibers in aqueous conditions: The nanostructure design rule used for this probe was the same as that used for the benzenethiol measurements. However, the refractive index contrast between the two sensing environments (n ~ 1.00 for the benzenethiol monolayer in air vs. n ~ 1.33 for the aqueous Rhodamine solution) will result in changes in the underlying plasmonic properties of the nanostructured metal surfaces, and moving to a different design rule could markedly improve the enhancements observed in solution. (Similar optimizations could be performed to improve the Raman enhancements for monolayers in air as well.) The experimental protocol could also be altered to promote adsorption of Rhodamine to the metal surface, such as pre-soaking the fiber tip in the solution prior to measurement or the addition of NaCl to the solution;[47] these measures would increase the effective concentration of Rhodamine within the evanescent electric field volume at the metal surface. These steps were not taken in the current work in order to provide a base view of the Raman enhancements possible using these nanoimprinted optical fibers, but further refinement of the probe nanostructures and the experimental procedures would be expected to yield greater device performance.

The SERS enhancement factors were not calculated in this work. Although the incident laser spot size at the entrance to the optical fiber is known (5 μm diameter spot), the spot size at the nanopatterned end would undoubtedly be larger than at the entrance because of the angular dispersion of light as it traveled through the fiber. Additionally, the incident laser intensity cannot be assumed to be evenly distributed across the illuminated region. Imaging studies along with computational simulations could provide guidance regarding the distribution of light at the SERS-active face of the probe after which more informed estimates could be made regarding the enhancement factors.

These results clearly reveal the successful enhancement of Raman scattering from benzenethiol and Rhodamine using a nanostructured optical fiber probe, as compared to unstructured optical fiber probes. However, significant room remains for optimization of the device performance: Only one set of nanostructure design rules was explored here as a demonstration of the ability for soft embossing to replicate a functional, Raman-enhancing plasmonic crystal structure on the optical fiber tip. Changes to the metal layer thickness as well as the pitch, size, and depth of the nanohole arrays could be used to tune the optical properties of the replicated plasmonic crystal for the Raman scattering of a desired analyte in a particular environment, and these efforts would be greatly informed by rigorous electrodynamic simulations of the optical and electric field properties of the plasmonic nanostructures. The soft lithography method used in this work is highly amenable to design rule changes – once the appropriate master has been created, the nanostructures can be readily replicated without the need to change the fabrication protocols that were implemented here. Additionally, the use of optical fibers with larger numerical apertures (and correspondingly larger acceptance angles for scattered light) could increase the efficiency of the collection of Raman scattered photons from the analyte and could be an exceedingly simple method to increase the effective performance of these SERS fiber probes.

2.5 Conclusions

In this work, soft nanoimprint lithography was successfully adapted to emboss a nanostructured plasmonic crystal in an inorganic spin-on-glass film on the tip of a multimode optical fiber. The use of soft embossing to create the nanostructured surface on the optical fiber not only enables the rapid fabrication of high quality nanostructures across the entire fiber tip but

also provides flexibility for the fabrication of nanostructures with different design rules. Darkfield microscopy was shown to be a rapid yet effective proxy for the evaluation of the quality of the replicated nanostructures. These patterned optical fibers were successfully used as optrodes for the measurement of surface-enhanced Raman spectra of benzenethiol monolayers adsorbed onto the plasmonic crystal surface as well as of Rhodamine 6G molecules in aqueous solution. Computational guidance regarding the optical properties of the embossed plasmonic crystals would greatly inform efforts to optimize the performance of these devices, and the fabrication flexibility afforded by soft lithography greatly enhances the utility of these optical fiber probes as a general platform for SERS sensing of different analytes within different environments.

2.6 Acknowledgments

I gratefully acknowledge the contributions of my collaborators towards this work: Matthew Schulmerich for his useful discussions and for collecting the Raman spectra, Jimin Yao for her assistance and advice with preparing and characterizing the nanoimprinted fibers, and Julio Soares for his useful discussions. My contributions to this work included design of the research; fabrication of the nanostructured optical fiber probes; darkfield microscopy, atomic force microscopy, and scanning electron microscopy measurements of the optical fiber tips; and analysis of the Raman spectra. This work was supported by the U. S. Department of Energy and was performed using resources at the Frederick Seitz Materials Research Laboratory Central Facilities at the University of Illinois, including the Center for Microanalysis of Materials, which is supported by the U.S. Department of Energy, Basic Energy Science, Materials Science and

Engineering Division under Award No. DE-FG02-07ER46471; the Micro/Nanofabrication Facility; and the Laser and Spectroscopy Facility.

2.7 Figures

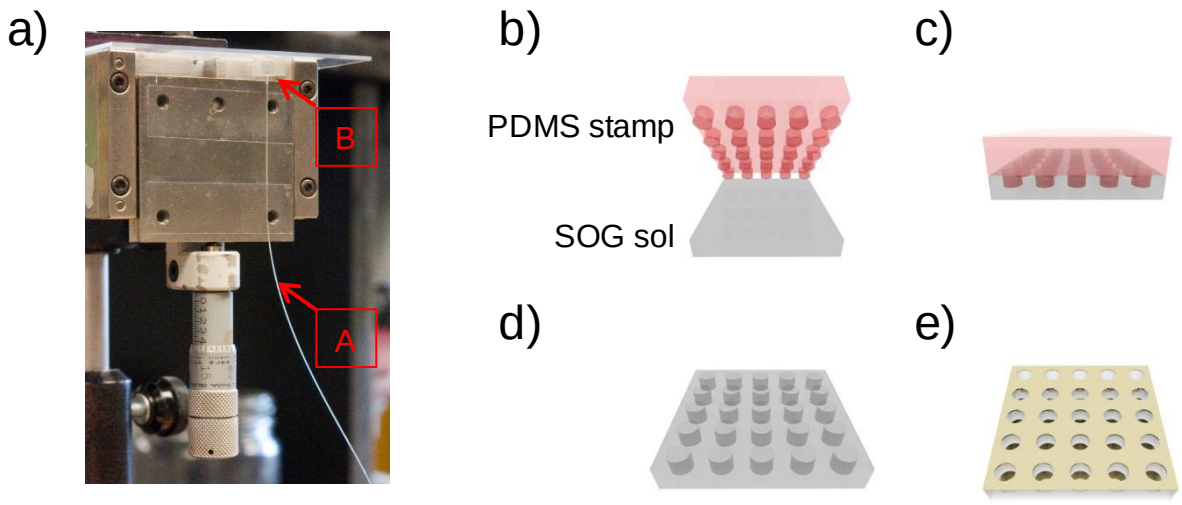

Figure 2.1 a) Photograph of an optical fiber mounted on a translation stage for nanostructure imprinting. The box labeled 'A' points to the optical fiber which has been secured on the stage with double-sided tape, and the box labeled 'B' points towards the composite PDMS stamp used to emboss the nanostructures. b-e) Schematic diagram of the soft embossing process for plasmonic crystal molding: b) SOG sol is applied to the optical fiber tip and the structured PDMS stamp is placed above the sample. c) The SOG coated fiber tip is pressed into the stamp and heated. d) After the initial thermal curing, the PDMS stamp is removed, leaving behind the nanopatterned SOG film on the optical fiber surface. e) After curing, a thin gold film is evaporated onto the patterned optical fiber tip to complete the fabrication of the plasmonic crystal.

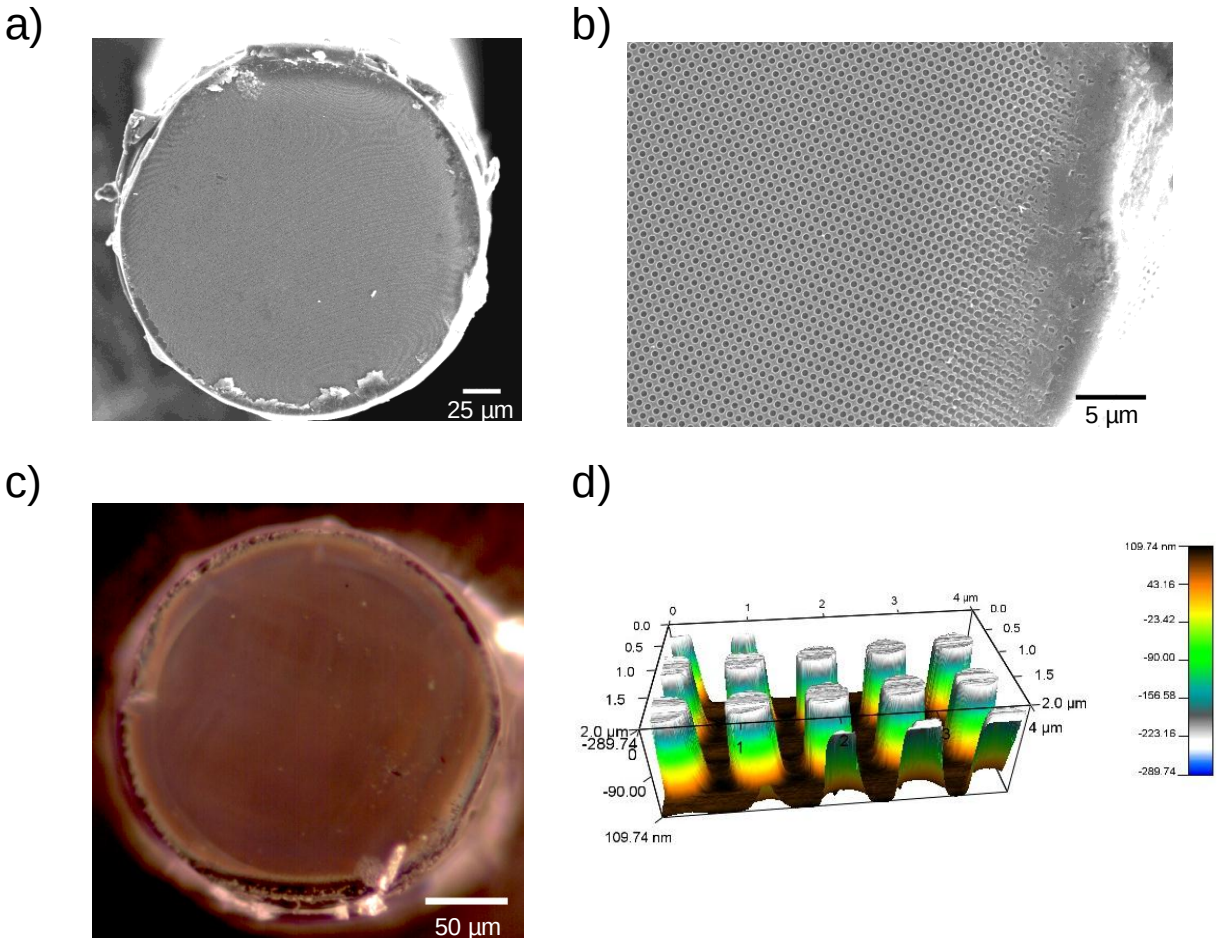

Figure 2.2 a) SEM image of a nanostructured optical fiber tip patterned through soft embossing. b) Higher magnification SEM image of the edge of the patterned optical fiber tip from panel a. c) Darkfield optical image of the same embossed optical fiber tip shown in panel a showing similar features. d) Inverted 3D projection of AFM measurements collected from nanostructures patterned on the optical fiber surface showing the uniformity of the nanohole relief depths.

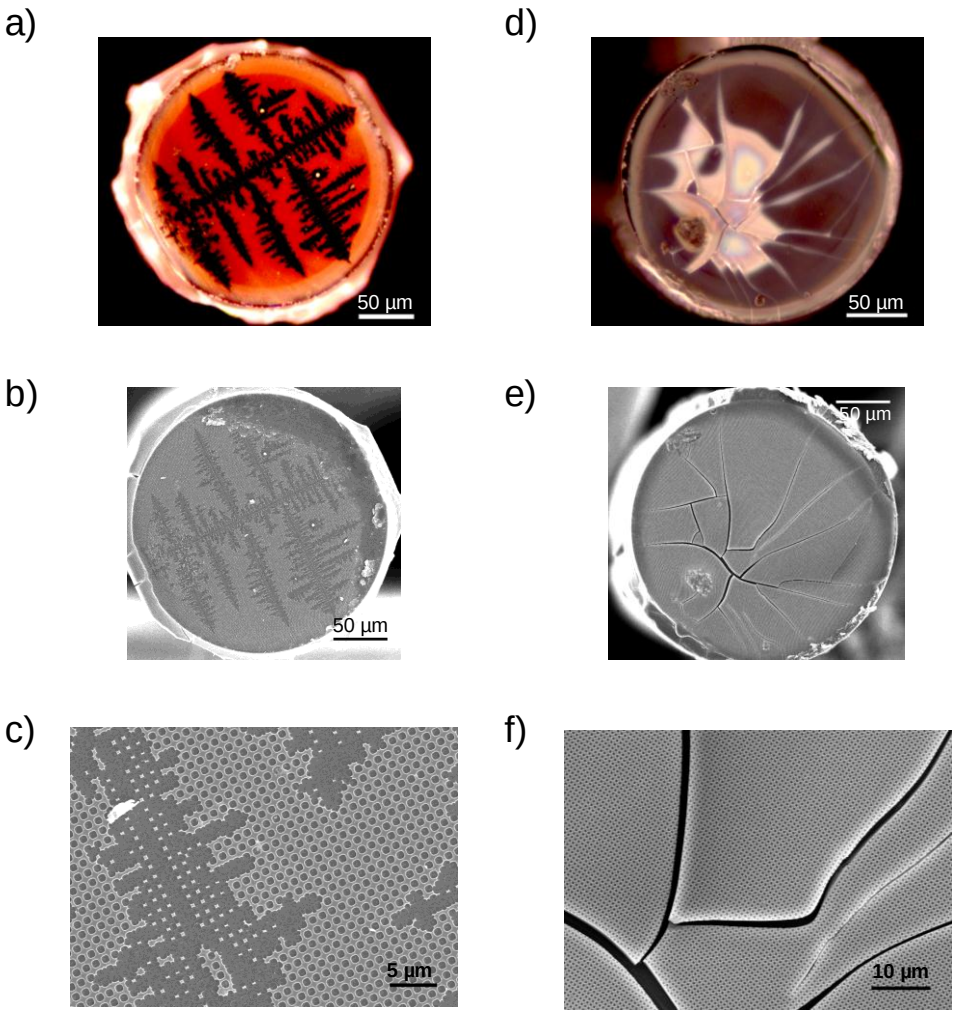

Figure 2.3 a) Darkfield and b) SEM images of a nanostructured fiber tip where parts of the patterned SOG film have lifted off from the silica surface. c) Magnified SEM image of the fiber tip presented in panels a and b showing regions where the patterned SOG film was detached from the surface. d) Darkfield and e) SEM images of a nanostructured fiber tip where the patterned SOG film cracked during thermal curing. f) Magnified SEM image of the fiber tip presented in panels d and e showing cracked areas of the nanostructured film. The center portion appears to have lifted off of the surface as well.

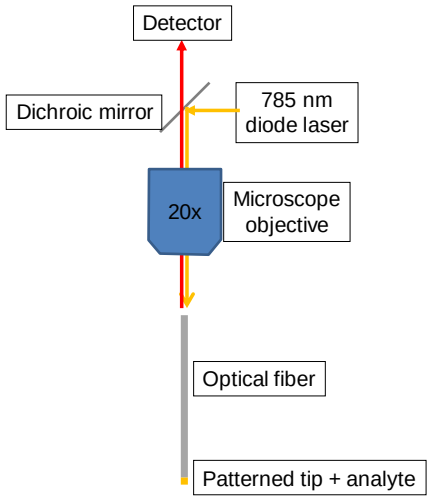

Figure 2.4 Block diagram of the instrumental arrangement for fiber-based SERS measurements. Incident illumination from a 785 nm diode laser (yellow line) was transported through a Raman microscope and focused through a microscope objective into the non-patterned end of the optical fiber. This laser illumination propagated through the fiber to reach the nanostructured tip where the analyte was present. Raman scattered photons (red line) were collected by the same fiber and transported back through the optical fiber to the microscope. A dichroic mirror was used to filter out reflected laser light, and the Raman scattered photons were passed to the detector.

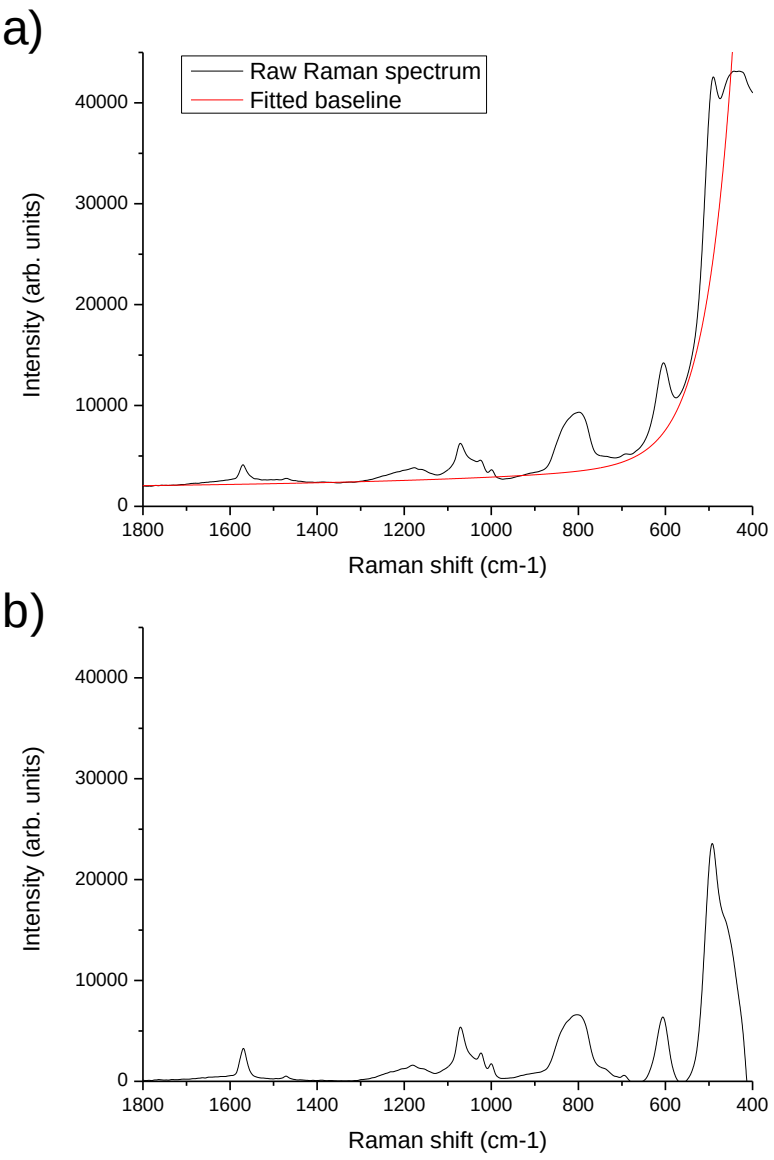

Figure 2.5 a) Comparison of raw Raman spectrum (black) of benzenethiol collected from a nanopatterned optical fiber and an exponential function (red) fit to approximate the baseline present in the raw spectrum. b) Resulting Raman spectrum for benzenethiol after subtraction of the baseline from the raw Raman spectrum presented in panel a.

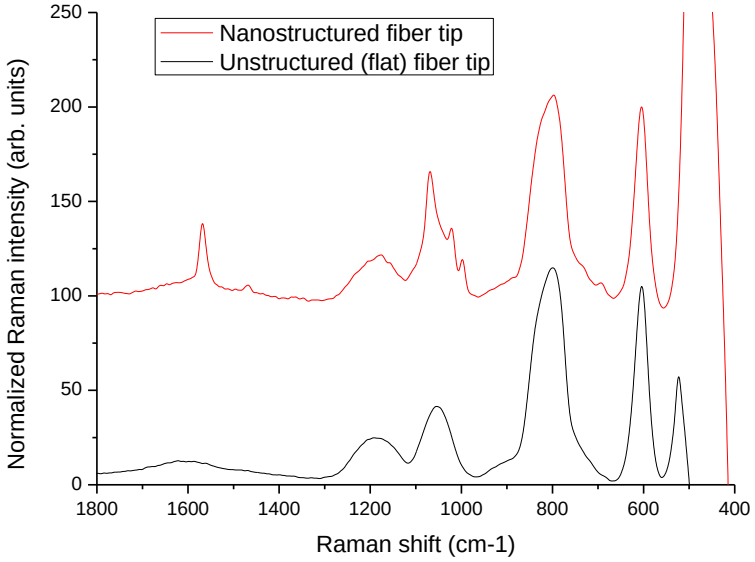

Figure 2.6 Normalized Raman spectra collected for benzenethiol monolayers adsorbed onto a nanostructured optical fiber tip (red) and onto a flat optical fiber tip (black). Both optical fiber tips were coated with 50 nm of gold.

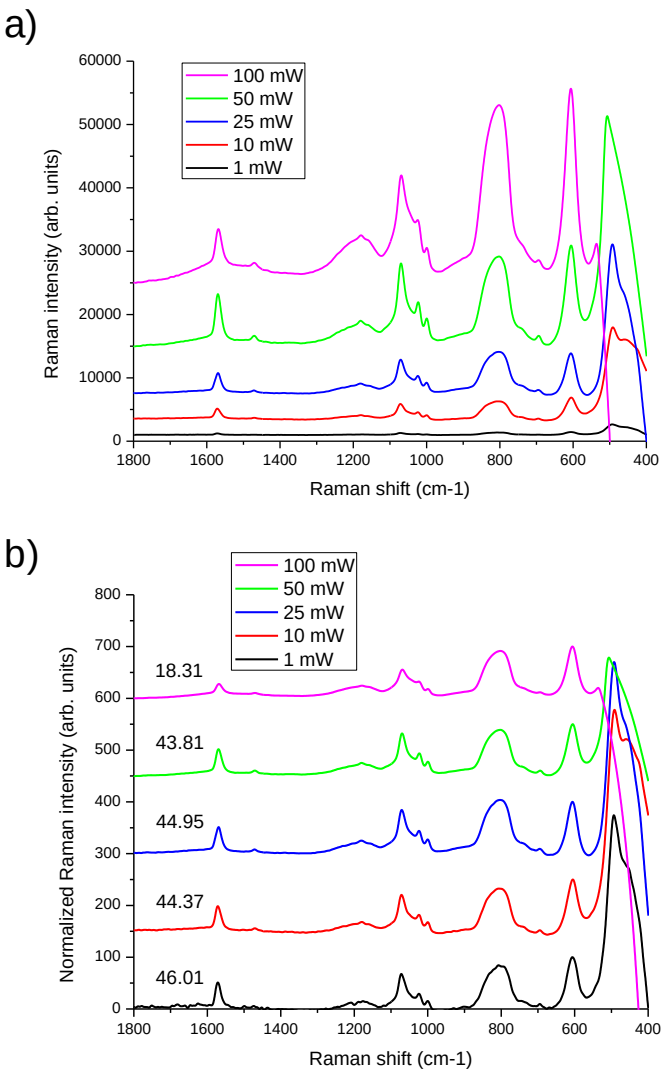

Figure 2.7 a) Comparison of baseline-subtracted Raman spectra of benzenethiol collected with a single nanostructured optical fiber using different excitation powers: 1 mW, 10 mW, 25 mW, 50 mW, and 100 mW. B) Comparison of the spectra presented in panel a after normalization against the silica peak at ~600 cm^{-1}. Normalized peak heights for the benzenethiol feature at ~1570 cm^{-1} are superimposed on each spectrum.

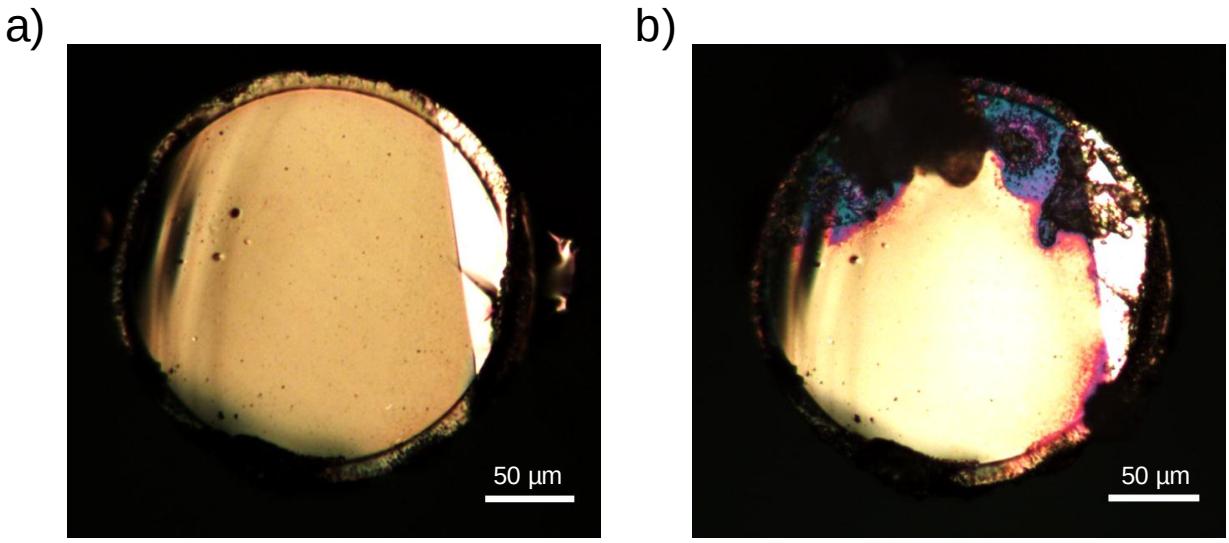

Figure 2.8 Darkfield images of gold-coated nanostructured optical fiber tips a) before and b) after Raman measurements and exposure to laser powers of 100 mW. The image in panel b clearly shows discoloration and damage to the metalized surface after laser exposure.

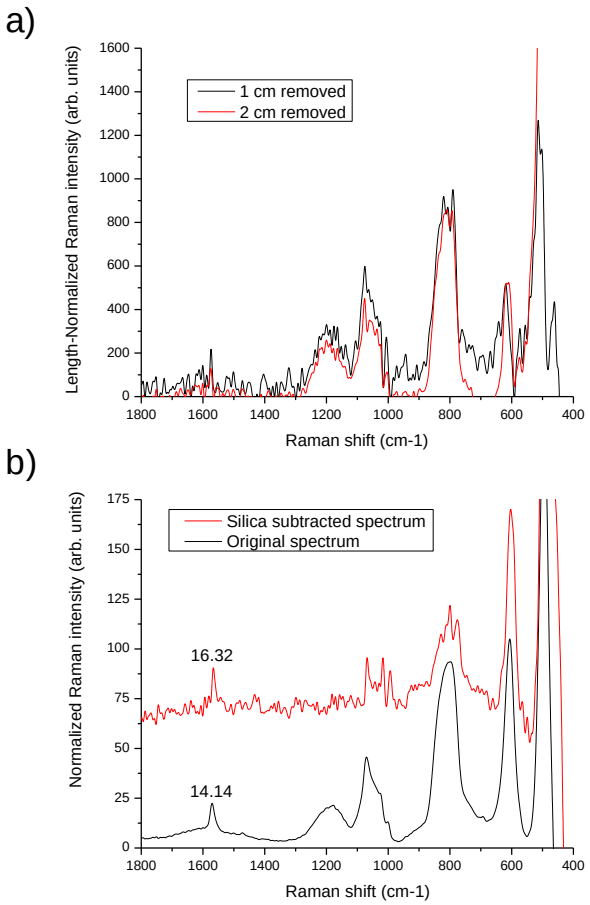

Figure 2.9 Raman spectra were collected from a single nanostructured optical fiber probe as portions were cut off. a) Comparison of the Raman spectra contributions attributed to non-enhanced Raman scattering from the silica fiber, normalized against the total length of optical fiber that was removed. b) Comparison between the original Raman spectrum (black curve) and the Raman spectrum after subtraction of the non-enhanced silica Raman signal (red curve) based on the normalized spectra presented in panel a. Subtraction of the silica contribution enhanced the benzenethiol peak at ~1570 cm^{-1} and recovered the benzenethiol peaks between 1000-1100 cm^{-1}.

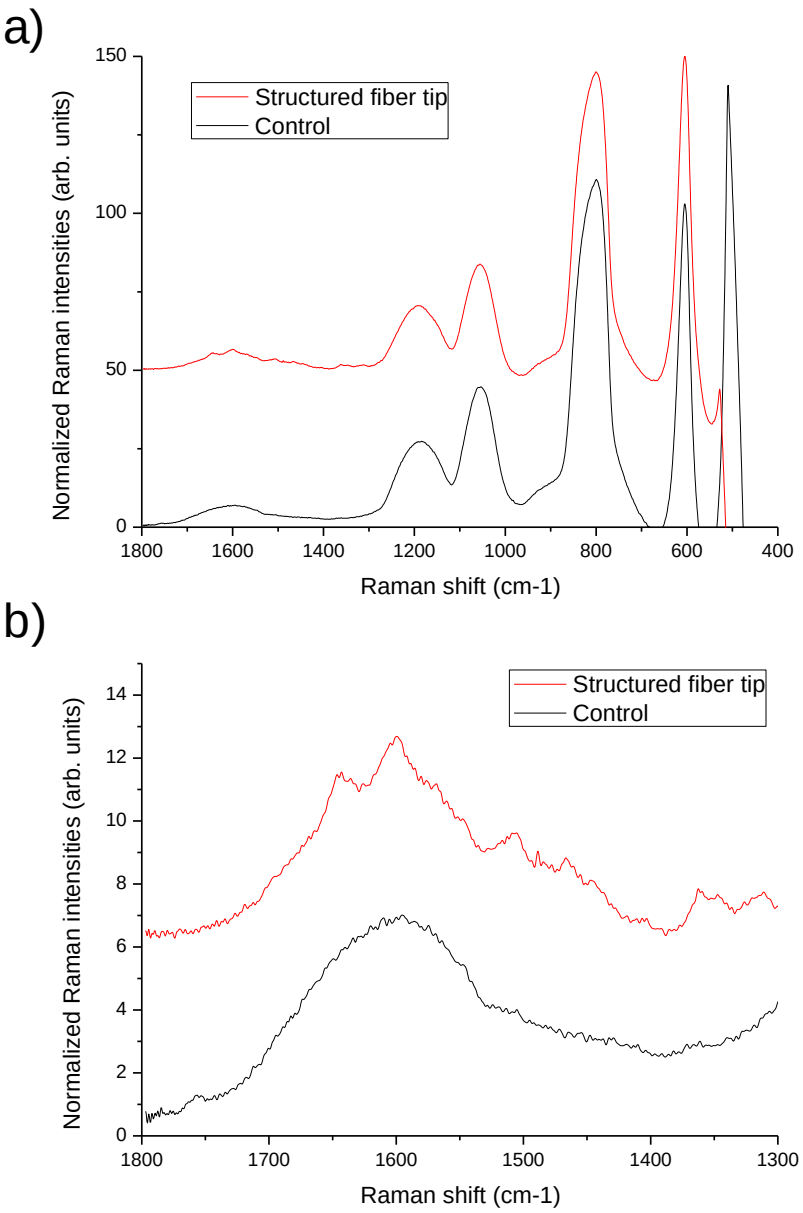

Figure 2.10 a) Comparison of normalized Raman spectra collected from nanostructured (red curve) and flat optical fiber tips (black curve) immersed in a 20 µM solution of Rhodamine 6G in water. b) Magnified view of the normalized Raman spectra presented in panel a showing the presence of peaks corresponding to Rhodamine in the spectrum collected using the patterned optical fiber.

2.8 References

(1) Le Ru, E. C.; Etchegoin, P. G. *Principles of Surface-Enhanced Raman Spectroscopy: And Related Plasmonic Effects*; Elsevier: Amsterdam, 2009.

(2) Golightly, R. S.; Doering, W. E.; Natan, M. J. *ACS Nano* **2009**, *3*, 2859.

(3) Kneipp, K.; Kneipp, H. *Appl. Spectrosc.* **2006**, *60*, 322A.

(4) Kneipp, K.; Wang, Y.; Kneipp, H.; Perelman, L. T.; Itzkan, I.; Dasari, R. R.; Feld, M. S. *Phys. Rev. Lett.* **1997**, *78*, 1667.

(5) Kneipp, K.; Kneipp, H.; Itzkan, I.; Dasari, R. R.; Feld, M. S. *Chem. Rev.* **1999**, *99*, 2957.

(6) Xu, H.; Bjerneld, E. J.; Käll, M.; Börjesson, L. *Phys. Rev. Lett.* **1999**, *83*, 4357.

(7) Michaels, A. M.; Nirmal, M.; Brus, L. E. *J. Am. Chem. Soc.* **1999**, *121*, 9932.

(8) Stoddart, P. R.; White, D. J. *Anal. Bioanal. Chem.* **2009**, *394*, 1761.

(9) *Handbook of Optical Fibre Sensing Technology*; López-Higuera, J. M., Ed.; John Wiley & Sons, 2002.

(10) Ma, J.; Li, Y.-S. *Appl. Opt.* **1996**, *35*, 2527.

(11) Cooney, T. F.; Skinner, H. T.; Angel, S. M. *Appl. Spectrosc.* **1996**, *50*, 849.

(12) Fleischmann, M.; Hendra, P. J.; McQuillan, A. J. *Chem. Phys. Lett.* **1974**, *26*, 163.

(13) Jeanmaire, D. L.; Van Duyne, R. P. *J. Electroanal. Chem.* **1977**, *84*, 1.

(14) Schatz, G.; Young, M.; Van Duyne, R. In *Surface-Enhanced Raman Scattering*; Kneipp, K., Moskovits, M., Kneipp, H., Eds.; Springer Berlin / Heidelberg: 2006; Vol. 103, p 19.

(15) Campion, A.; Kambhampati, P. *Chem. Soc. Rev.* **1998**, *27*, 241.

(16) Chu, H.; Liu, Y.; Huang, Y.; Zhao, Y. *Opt. Express* **2007**, *15*, 12230.

(17) Stokes, D. L.; Vo-Dinh, T. *Sens. Actuator B-Chem.* **2000**, *69*, 28.

(18) Mullen, K. I.; Wang, D.; Crane, L. G.; Carron, K. T. *Anal. Chem.* **1992**, *64*, 930.

(19) Amezcua-Correa, A.; Yang, J.; Finlayson, C. E.; Peacock, A. C.; Hayes, J. R.; Sazio, P. J. A.; Baumberg, J. J.; Howdle, S. M. *Adv. Funct. Mater.* **2007**, *17*, 2024.

(20) Konorov, S. O.; Addison, C. J.; Schulze, H. G.; Turner, R. F. B.; Blades, M. W. *Opt. Lett.* **2006**, *31*, 1911.

(21) Xuan, Y.; Chao, S.; Wheeler, D.; Newhouse, R.; Bin, C.; Zhang, J. Z.; Gu, C. *J. Opt. Soc. Am. A* **2010**, *27*, 977.

(22) Lan, X.; Han, Y.; Wei, T.; Zhang, Y.; Jiang, L.; Tsai, H.-L.; Xiao, H. *Opt. Lett.* **2009**, *34*, 2285.

(23) Ma, X. D.; Huo, H. B.; Wang, W. H.; Tian, Y.; Wu, N.; Guthy, C.; Shen, M. Y.; Wang, X. W. *Sensors* **2010**, *10*, 11064.

(24) Pesapane, A.; Lucotti, A.; Zerbi, G. *J. Raman Spectrosc.* **2010**, *41*, 256.

(25) Stokes, D. L.; Chi, Z. H.; Vo-Dinh, T. *Appl. Spectrosc.* **2004**, *58*, 292.

(26) Viets, C.; Hill, W. *J. Mol. Struct.* **2001**, *563-564*, 163.

(27) Dhawan, A.; Muth, J. F.; Leonard, D. N.; Gerhold, M. D.; Gleeson, J.; Vo-Dinh, T.; Russell, P. E. *J. Vac. Sci. Technol. B* **2008**, *26*, 2168.

(28) Fan, M. K.; Andrade, G. F. S.; Brolo, A. G. *Anal. Chim. Acta* **2011**, *693*, 7.

(29) Smythe, E. J.; Dickey, M. D.; Jiming, B.; Whitesides, G. M.; Capasso, F. *Nano Lett.* **2009**, *9*, 1132.

(30) Kostovski, G.; Chinnasamy, U.; Jayawardhana, S.; Stoddart, P. R.; Mitchell, A. *Adv. Mater.* **2011**, *23*, 531.

(31) Yao, J.; Le, A.-P.; Schulmerich, M. V.; Maria, J.; Lee, T.-W.; Gray, S. K.; Bhargava, R.; Rogers, J. A.; Nuzzo, R. G. *ACS Nano* **2011**, *Published online*.

(32) Stewart, M. E.; Mack, N. H.; Malyarchuk, V.; Soares, J. A. N. T.; Lee, T.-W.; Gray, S. K.; Nuzzo, R. G.; Rogers, J. A. *Proc. Nat. Acad. Sci. USA* **2006**, *103*, 17143.

(33) Baca, A. J.; Truong, T. T.; Cambrea, L. R.; Montgomery, J. M.; Gray, S. K.; Abdula, D.; Banks, T. R.; Yao, J.; Nuzzo, R. G.; Rogers, J. A. *Appl. Phys. Lett.* **2009**, *94*, 243109.

(34) Malyarchuk, V.; Hua, F.; Mack, N.; Velasquez, V.; White, J.; Nuzzo, R.; Rogers, J. *Opt. Express* **2005**, *13*, 5669.

(35) Malyarchuk, V.; Stewart, M. E.; Nuzzo, R. G.; Rogers, J. A. *Appl. Phys. Lett.* **2007**, *90*, 203113.

(36) Yao, J.; Stewart, M. E.; Maria, J.; Lee, T.-W.; Gray, S. K.; Rogers, J. A.; Nuzzo, R. G. *Angew. Chem. Int. Ed.* **2008**, *47*, 5013.

(37) Haubert, K.; Drier, T.; Beebe, D. *Lab on a Chip* **2006**, *6*, 1548.

(38) Bhattacharya, S.; Datta, A.; Berg, J. M.; Gangopadhyay, S. *J. Microelectromech. Syst.* **2005**, *14*, 590.

(39) *Honeywell ACCUGLASS T-14 Spin-on Glass*, Datasheet No. PB0030707Rev10; Honeywell International, Inc., https://www51.honeywell.com/sm/em/common/documents/msds-em-product-application-documents/ACCUGLASS-T-14.pdf (accessed August 22, 2010).

(40) Baca, A. J.; Montgomery, J. M.; Cambrea, L. R.; Moran, M.; Johnson, L.; Yacoub, J.; Truong, T. T. *J. Phys. Chem. C* **2011**, *115*, 7171.

(41) Szafranski, C. A.; Tanner, W.; Laibinis, P. E.; Garrell, R. L. *Langmuir* **1998**, *14*, 3570.

(42) Joo, T. H.; Kim, M. S.; Kim, K. *J. Raman Spectrosc.* **1987**, *18*, 57.

(43) Pasquarello, A.; Car, R. *Phys. Rev. Lett.* **1998**, *80*, 5145.

(44) Lan, G.-L.; Banerjee, P. K.; Mitra, S. S. *J. Raman Spectrosc.* **1981**, *11*, 416.

(45) Hildebrandt, P.; Stockburger, M. *J. Phys. Chem.* **1984**, *88*, 5935.

(46) Watanabe, H.; Hayazawa, N.; Inouye, Y.; Kawata, S. *J. Phys. Chem. B* **2005**, *109*, 5012.

(47) Pristinski, D.; Tan, S.; Erol, M.; Du, H.; Sukhishvili, S. *J. Raman Spectrosc.* **2006**, *37*, 762.

CHAPTER 3

Quantitative Reflection Imaging of Thin Films on Nanostructured Plasmonic Crystals

3.1 Abstract

Studies of the dynamic interactions and growth of cells in response to chemical and physical cues from their substrates would benefit greatly from the development of analytical techniques capable of surface sensitive imaging in real time. To this end, a reflection imaging protocol capable of quantitative determination of the thicknesses of thin films grown on nanoimprinted plasmonic crystal surfaces was developed, its ability to measure films of nanometer-scale thicknesses was demonstrated. Layer-by-layer polyelectrolyte films served as the model system to calibrate the reflection contrast response as a function of surface layer thickness, and these calibrations were used to quantitate the thicknesses of peripheral structures from *Aplysia californica* pedal neurons cultured on the plasmonic crystal surface. Spectral regions with differing image contrast behavior as surface layer thicknesses increased were isolated using bandpass filters, and we developed an analysis method to combine data from images acquired using different bandpass filters to account for this behavior. In fact, these composite images displayed increased contrast and sensitivity to surface layer thickness. This reflection imaging method is inexpensive to implement, using easily fabricated nanoimprinted

plasmonic crystals and a common laboratory microscope with CCD camera and filters, yet is capable of quantitating thicknesses at nanometer scales over large areas and in near-real time.

3.2 Introduction

The morphology and outgrowth behavior of cells is significantly influenced by their interactions with a substrate,[1-7] but quantitative investigations of the three dimensional structure of cells and these cell-substrate interactions are hampered by the imaging techniques currently available. In turn, this directly impacts our ability to probe and, ultimately, to understanding cell growth and signaling. Light scattering and absorption by components such as the nucleus and mitochondria make the cell optically thick, complicating efforts for three dimensional imaging. By contrast, two dimensional imaging is readily performed, but these data are, in essence, only projections of 3D information, and the need to work around this limitation has driven the development of increasingly complex instrumentation, techniques, and protocols. Alternative imaging methods capable of providing truly quantitative three dimensional information about the outgrowth of cells (at minimal expense) would reveal, quite literally, additional dimensions of cell behavior that could only be inferred from existing techniques.

Optical microscopy methods are widely used for the study of cells and offer a number of advantages, including rapid data acquisition using common laboratory equipment which is readily available at (relatively) low expense. Within this long history, a number of techniques and instrumental modifications have been developed to increase the contrast and resolution of images, including phase contrast microscopy[8] and differential interference contrast microscopy.[9,10] Fluorescence microscopy and immunostaining techniques have been used with great success to selectively label cellular structures with a fluorescent probe, and multiple probes

can be implemented to image multiple types of structures simultaneously.[5,11,12] These techniques have elucidated countless details regarding cellular structure, dynamics, and interactions, but they are generally limited to providing information in the *x*-*y* plane with little information in *z*.

Alternative optical imaging methods are capable of providing this three-dimensional information. Scanning confocal microscopy is capable of high resolution imaging of cells in three dimensions,[5] while total internal reflection microscopy is capable of selectively visualizing the interface between a cell and its substrate.[13,14] However, these methods generally require the addition of fluorescent labels through protocols which can be cumbersome and require a significant degree of optimization; the introduction of fluorescent labels in live cells may alter the natural behavior of the cell. Scanning white light interference microscopy uses an interferometer and a microscope stage capable of precise vertical movements to vertically scan the focal plane through the sample; the resulting interference fringes can be analyzed to determine the surface topography.[15,16] Digital holographic microscopy has been used to map the effective transmission path lengths of cell structures without the need for external labels.[17] A drawback of all of these techniques, however, is that they have significantly more demanding instrumentation requirements.

Surface topography measurements fall squarely within the domain of scanning probe techniques such as atomic force microscopy, which is capable of highly sensitive measurements of surface feature heights ranging from angstroms to micrometers in thickness.[18-20] Functionalization of the probe can provide additional information regarding the nature of the surface in addition to its topography. The major drawback of atomic force microscopy is data acquisition speed, which is limited by the rate at which the probe can be scanned across the

substrate. Imaging over large areas incurs a tremendous time penalty, limiting its effectiveness in the observations of dynamic systems.

Surface plasmon resonances (SPR) are coherent oscillations of conduction electrons at a metal-dielectric interface which generate an evanescent electric field that decays exponentially with distance from the metal surface; this field is generally considered to extend up to ~100-200 nm from the metal surface.[21-24] Because the plasmonic electric field is localized within a few hundred nanometers of the metal surface, SPR imaging methods are inherently sensitive to changes in the refractive index profile within this distance from the surface. These SPR-based techniques have been used to detect surface binding events with high sensitivity and have been employed in multiplex assays sensing antibody-antigen interactions or DNA hybridization events.[25-29] These measurements can be made without the need for external labeling of the analyte, and SPR sensing is capable of analyte detection at sub-monolayer sensitivities in real time. It should be noted that in themselves, SPR-based methods are sensitive only to changes in refractive index and provide little or no chemically-specific information. Additional chemical recognition or reporting mechanisms can be incorporated to bridge this gap, providing data that is both chemically specific and localized at the surface.

These inherent capabilities make SPR-based imaging a natural fit for studies of cell morphology and substrate interactions within this limit, with demonstrations of refractive index mapping and thickness profiling of cell-surface contacts previously reported.[30-33] Many SPR imaging techniques utilize a configuration in which a prism is used to couple light into a flat gold film in the Kretschmann configuration, but as a consequence, these techniques require relatively complex optical systems with demanding alignment requirements.[22,25,29,34] An ideal SPR

imaging system would be able to provide this surface-sensitive data in near-real time but without the need for specialized optical equipment.

Grating-based nanoimprinted plasmonic crystals have been introduced as an alternative to prism-based systems for SPR imaging and are capable of the same surface-sensitive measurements but with relaxed instrumentation requirements.[23,35-40] In fact, molecular-scale imaging has been successfully demonstrated on plasmonic crystal substrates using a common laboratory microscope and charge-coupled device camera.[36] The optical and plasmonic properties of these plasmonic crystals will change as a function of the refractive index and thickness of any material immediately adjacent to the metal surface, and previous studies have shown that the plasmonic response does indeed change for surface layers up to ~90 nm thick.[37]

This work focuses on developing imaging techniques to take advantage of the surface sensitivity of these nanostructured plasmonic crystals for quantitative thickness determinations within this ~90 nm limit using the controlled growth of polyelectrolyte layer-by-layer assemblies on the plasmonic crystal surface as a calibration system. The very nature of the underlying surface plasmon effects produces complex imaging phenomena, and the notable attribute of the technique developed here is the explicit incorporation of wavelength dependence in the analysis of multispectral plasmonic reflection images. These complex plasmonic phenomena are not otherwise encountered in more established reflection microscopy methods, but they in fact present exciting possibilities for the development of image contrasts that, as we show here, can be both enhanced and interpreted quantitatively as applied to the structural features present in a complex, surface-bound system – in this case, a fixed pedal neuron from *Aplysia californica*, plated and sustained in culture to elicit process development for subsequent study.[41-43]

3.3 Experimental Materials and Methods

3.3.1 Reagents

Reagents were used as received without further purification unless otherwise specified. Spin-on-glass (product number 314) was purchased from Honeywell and was filtered through 0.02 μm syringe filters immediately before use. Polydimethylsiloxane (soft PDMS; Sylgard 184, Dow Corning) was purchased from Ellsworth Adhesives. Hard PDMS components: poly(7-8% vinylmethylsiloxane)-(dimethylsiloxane) (VDT-731); 1,3,5,7-tetravinyl-1,3,5,7-tetramethylcyclotetrasiloxane(SIT-7900); poly(25-30% methylhydrosiloxane)-(dimethylsiloxane) (HMS-301); and platinum-divinyltetramethyldisiloxane (SIP6831.1) were purchased from Gelest. Photocurable polyurethane (NOA 73) was purchased from Norland Products. Manganese(II) chloride tetrahydrate, poly(sodium 4-styrenesulfonate) (PSS, MW = 70,000 g/mol), poly(allylamine hydrochloride) (PAH, MW = 70,000 g/mol), and 4,4'-dithiodibutyric acid (DTBA) were purchased from Sigma-Aldrich. Ultrapure water (18 MΩ) was generated using a Millipore Milli-Q Academic A-10 system and used to prepare the polyelectrolyte solutions.

3.3.2 Plasmonic Crystal Fabrication via Soft Nanoimprint Lithography

Full 3D plasmonic crystals were fabricated using a soft nanoimprint lithography technique as previously reported.[23,36,37,44] Briefly, a composite hard PDMS/soft PDMS stamp was cast from a photolithographically patterned photoresist master and used to mold a replica master in spin-on-glass.[40] An additional composite PDMS stamp is then cast from the spin-on-

glass master and is subsequently used to fabricate the plasmonic crystals used in this study; a schematic illustration of the nanoimprinting process is presented in Figure 3.1. A photocurable polyurethane polymer (NOA) is drop cast onto a glass slide, and this second PDMS stamp is pressed into the liquid prepolymer (Figure 3.1a) and then exposed to ultraviolet light (UVOCS UV-ozone cleaning chamber) for 5 minutes to cure the polyurethane (Figure 3.1b). The stamp is peeled away from the now-solid patterned polymer structure (Figure 3.1c) which is cured at 65°C overnight. The replicated nanostructures are a well-defined square array of cylindrical depressions with a hole spacing (center to center) of ~740 nm, a hole diameter of ~460 nm, and a relief depth of ~300 nm. An adhesion layer (5 nm TiO2) and a metal layer (30 nm gold) are sputtered onto the relief structure (AJA International, 5 mTorr argon) to complete the plasmonic crystal fabrication (Figure 3.1d).

3.3.3 Polyelectrolyte Layer-by-layer Assemblies on Plasmonic Crystal Surfaces

Polyelectrolyte layer-by-layer assemblies were grown on the plasmonic crystal surface and on gold-coated pieces of silicon following previously reported procedures.[37,45] A small drop of NOA was applied to one corner of the plasmonic crystal surface and cured to block a region of the plasmonic crystal from adsorption of the polyelectrolyte layers. Carboxyl-terminated self-assembled monolayers were formed on the gold plasmonic crystal surface by immersing the plasmonic crystal in ethanolic solutions of DTBA (33 mM) for 24 h, after which the plasmonic crystals were rinsed thoroughly with ethanol. Layers of PAH and PSS were alternately adsorbed onto the surface to build up the polyelectrolyte assembly. The plasmonic crystal was immersed in a PAH solution (3 mg PAH / mL in water, pH = 8.0) for five minutes, rinsed thoroughly with water and dried with nitrogen gas. The crystal was then immersed in a PSS solution (3 mg PSS /

mL in 1 M $MnCl_2$, pH = 2.0) for 90 s, rinsed with water, and dried with nitrogen gas. Reflection images and ellipsometry measurements were collected after each round of polyelectrolyte depositions.

3.3.4 Ellipsometry of Polyelectrolyte Layer-by-layer (LBL) Assemblies

The thicknesses of polyelectrolyte LBL assemblies grown on gold-coated pieces of silicon were measured using a Woollam VASE spectroscopic ellipsometer using 50° and 70° incident angles; data were collected over a wavelength range of 400-900 nm. The polyelectrolyte layer was modeled as a Cauchy material with parameters An = 1.61, Bn = 0.01, Cn = 0 such that the modeled refractive index at 630 nm was 1.635.[37,45] The equivalent thickness for a refractive index corrected material of more biological origin was modeled from the spectroscopic ellipsometry data by substituting the polyelectrolyte layer in the model for a layer modeled as a Cauchy material with parameters An = 1.47, Bn = 0.01, Cn = 0 corresponding to a refractive index n = 1.495 at 630 nm.[46,47]

3.3.5 Cell Culture and Fixation of *Aplysia californica* Neurons

Aplysia californica (100-300 g) were supplied by the National Resource for Aplysia (Miami, FL) and kept in circulated, aerated seawater at 14°C. Prior to dissection, the animals were anesthetized by injection of isotonic magnesium chloride solution into the body cavity (~30-50% of body weight). Individual *Aplysia* pedal neurons were isolated after incubation in artificial seawater (ASW; (in mM) 460 NaCl, 10 KCl, 10 $CaCl_2$, 22 $MgCl_2$, 26 $MgSO_4$, and 10 HEPES, pH 7.7) with proteases (1% type XIV, Sigma-Aldrich) at 34°C for between 60-120 min

as described previously.[48,49] A poly-L-lysine layer (1-2 nm) was formed on the plasmonic crystal surface, and the cells were mechanically isolated in ASW, transferred onto the plasmonic crystal surface immersed in ASW supplemented with antibiotics (ASW containing 100 units/ml penicillin G, 100 mg/ml streptomycin, and 100 mg/ml gentamicin, pH 7.7) and left to attach and grow overnight at room temperature. Six to eight pedal neuron cells were cultured on the plasmonic crystal surface at a time. Cells were fixed by addition of 1 mL of 4% paraformaldehyde to 3 ml ASW antibiotic culture media and occasional stirring for 30 s, removal of 3 mL of the solution, addition of another 1 mL of the 4% paraformaldehyde solution in water and exposure of the cell culture for 30 s, followed by the removal of all solution. After removal of the fixation solution, the cells were washed with deionized water and dried.

3.3.6 Reflection Imaging using a Laboratory Optical Microscope

Reflection mode images of both the polyelectrolyte LBL structures and of cells cultured on the plasmonic crystal surface were made using an Olympus AX-70 upright microscope fitted with a halogen light source and a 20×, 0.40 NA microscope objective. A frosted glass filter was placed immediately after the light source to homogenize the incident illumination. The plasmonic crystal was turned upside-down such that the light was incident first on the glass substrate of the plasmonic crystal before propagating to the nanostructured metal surface. Bandpass filters (500-550 nm, 525-1000 nm, 570-600 nm, 570-1000, and 610-700 nm) were purchased from Omega Optical and inserted in the microscope immediately in front of the microscope camera. Images were captured using an Optronics Magnafire charge-coupled device camera (1280 x 1024 array of pixels, each pixel 6.7 x 6.7 um). The halogen lamp intensity was varied to control the overall exposure. Grayscale images were acquired using individual

exposure times of 750 ms with fifteen consecutive images averaged together. Image processing and thickness calibration application was performed using Matlab while image analysis was performed using ImageJ.

Vignetting in the reflection images was corrected using images of a silver mirror acquired with each bandpass filter in place. A Gaussian blur (100 pixel radius) was applied to the reference mirror image to remove blemishes and debris in the image, and the reference image was normalized by dividing each pixel by the average pixel intensity in the image. Vignetting in the polyelectrolyte layer and cell images was corrected using a pixel-by-pixel division of the experimental image by the blurred mirror reference image obtained with the corresponding bandpass filter.

3.3.7 Atomic Force Microscopy and Scanning Electron Microscopy of Cells on Plasmonic Crystals

Atomic force microscopy (AFM) height profiles of *Aplysia* neurons grown on the plasmonic crystal surface were measured using an Asylum Research MFP-3D atomic force microscope operated in tapping mode. Analysis of the data, including the Fast Fourier - Transform filtering, was performed using IgorPro and the Asylum Research AFM software. Scanning electron microscopy images of *Aplysia* neurons cultured on plasmonic crystals were obtained using a JEOL 6060-LV scanning electron microscope operated under high vacuum. A thin layer of Au/Pd was sputtered onto the plasmonic crystal after all other analyses were complete to make the sample electrically conductive.

3.3.8 Finite-Difference Time-Domain (FDTD) Simulations of Plasmonic Nanostructures

Full 3D FDTD simulations were carried out to model the zero-order reflection and transmission spectra (with light incident on the glass substrate) and their changes with polyelectrolyte layer thickness. The unit cell grid spacing was 4 nm in all three dimensions with a total unit cell size of 187 x 187 x 600 grid points. The unit cell geometry defines a gold nanohole in the x-y plane with a 740 nm center-to-center hole spacing, 456 nm hole diameter, 292 nm relief depth, 32 nm Au film on the top surface of the plasmonic crystal, 12 nm Au film conformally coating the nanohole sidewalls, and 12 nm Au film on the bottom of the nanoholes. Periodic boundary conditions in x and y generate an infinite square array, and uniaxial perfectly matched layers were incorporated on the top and bottom surfaces of the unit cell to minimize the effects of unintended reflection from the domain boundaries. The frequency dependent dielectric constant of gold was modeled using previously reported parameters for a Drude plus two-pole Lorentzian model.[39] The refractive indices of NOA, polyelectrolyte, refractive index corrected material, and air were taken to be 1.56, 1.64, 1.50, and 1.00, respectively.

3.4 Results and Discussion

3.4.1 Polyelectrolyte Layer-by-Layer Assembly on Plasmonic Crystal Surfaces

Polyelectrolyte layer-by-layer (LBL) films were assembled on the plasmonic crystal surface to serve as a calibration system for the reflection contrast. A self-assembled monolayer of DTBA was initially formed on the gold surface of the plasmonic crystal in order to anchor the subsequent polyelectrolyte layers to the gold surface, and the carboxyl groups on the DTBA

monolayer served as the initial (negatively-charged) layer for the electrostatic attraction of the PAH layer to the plasmonic crystal surface. Alternating layers of positively charged PAH and negatively charged PSS were then deposited onto the surface of the DTBA-modified plasmonic crystal via the electrostatic attraction between the polymer in solution and the material that has already been deposited on the surface. (The charge states of the polymers are controlled via the pH of the solution which controls the protonation states of PAH and PSS.) This polyelectrolyte film growth is electrostatically self-limiting, enabling controlled growth of surface layers which can be dried, analyzed, and then built upon further. Spectroscopic ellipsometry was used to measure the thickness of dried polyelectrolyte films which were simultaneously deposited onto gold-coated pieces of silicon wafer under identical conditions as those deposited on the plasmonic crystals.

The optical response of plasmonic systems are influenced by both the thickness of the material at the metal-dielectric interface as well as its refractive index, and the marked refractive index contrast between the polyelectrolytes ($n \sim 1.64$)[45] and those of biological materials ($n \sim$ 1.35-1.5)[17,46,47,50] may present a challenge to the suitability of these LBL films as a calibration system. To investigate these effects, the thicknesses of the polyelectrolyte films were measured using ellipsometry, a technique which itself is sensitive to layer thickness and refractive index. The ellipsometric data were modeled in order to determine the polyelectrolyte layer thickness, and these data were subsequently analyzed to determine the thickness required for a layer with a refractive index more appropriate for biological materials with high organic content ($n = 1.50$) to exhibit similar ellipsometric behavior. For clarity, we introduce a refractive index corrected thickness, symbolized by θ in this work, which corresponds to the thicknesses determined through ellipsometric modeling using the adjusted refractive index ($n = 1.50$) for biological

materials, and Figure 3.2 presents the corresponding pairs of polyelectrolyte and index corrected thicknesses.

The validity of this ellipsometric thickness conversion was evaluated using finite-difference time-domain (FDTD) calculations. Because of the finite spacing between grid points (4 nm) available for the calculation, only a few pairs of polyelectrolyte and refractive index corrected thickness equivalents could be adequately incorporated into the model. Figure 3.3 presents the simulated transmission spectra for plasmonic crystals coated with a conformal dielectric layer of either polyelectrolyte or index corrected material with the appropriate thickness. The transmission spectra show remarkable similarity between both cases, especially for the data presented in Figure 3.3b where the modeled thicknesses (polyelectrolyte = 24 nm, index corrected material = 28 nm) were closest to the ellipsometrically estimated thicknesses. These data demonstrate the suitability of using a polyelectrolyte LBL assembly as a calibration system which can be extended to other materials; a library of equivalent layer thicknesses for materials of different refractive indices could be derived from a single ellipsometry dataset. The small discrepancies between the transmission spectra are most likely a result of errors introduced when adjusting the layer thickness to values which fit neatly within the computational grid. Calibration data subsequently presented here are for refractive index corrected thicknesses derived from these ellipsometric measurements.

3.4.2 Reflection Imaging Contrast Calibration

Reflection images of polyelectrolyte LBL films deposited on the plasmonic crystal surface were acquired using a common laboratory optical microscope with bandpass filters

inserted immediately before the camera to restrict the wavelengths being imaged. The plasmonic crystal was oriented such that the light was incident on the glass substrate (i.e., the plasmonic crystal was imaged from the reverse side), and a representative image is presented in Figure 3.4a. The area labeled NOA denotes a region where a drop of photocurable polyurethane (NOA) was deposited and cured on the plasmonic crystal surface prior to formation of the DTBA self-assembled monolayer. This blocked a region of the plasmonic crystal from subsequent LBL deposition and, from the standpoint of the plasmonic sensing volume, effectively created a region where the surface refractive index profile remained constant; the region marked LBL in the image denotes the area where the polyelectrolyte was deposited. Because the NOA region remained effectively constant throughout the LBL growth process, the pixel intensities in this region of the image could serve as an internal reference to correct for variations in illumination intensity between images, a necessity considering the calibration data were derived from multiple images. The red boxes drawn on the figure are illustrative of the areas in each region where the average pixel intensity was calculated.

Reflection images were collected using different bandpass filters at different points during the deposition of the polyelectrolyte LBL assembly, and the calibrations were calculated in reference to the plasmonic crystal prior to any polyelectrolyte adsorption. The pixel values for each image were scaled such that the average pixel value in the polyelectrolyte-free NOA regions were equal, and the normalized reflection contrast was calculated using the average pixel intensity from the LBL regions according to the following formula:

$$\text{Normalized reflection contrast} = \frac{\text{[LBL pixel average]} - \text{[reference pixel average]}}{\text{[reference pixel average]}}$$

This normalized contrast is similar to multispectral analysis methods that have been previously applied to spectroscopic measurements using plasmonic crystals, but this metric does not use the absolute value. Thus, the normalized reflection contrast can be positive or negative (corresponding to regions where the reflectivity is higher or lower than the reference condition) and matches the behavior that was observed in the experimental images.

It should be noted that the average pixel values calculated for the NOA (polyelectrolyte free) regions of the plasmonic crystal were used only as a correction for the illumination intensity. The reference average used to calculate the normalized reflectance contrast above refers to the average intensity calculated from the LBL region of the image before any polyelectrolyte was adsorbed.

The lateral resolution of this optical system (including the camera, microscope optics, and plasmonic crystal) was estimated based upon an analysis of the step-edge profile between the NOA and LBL regions in the calibration images. A step function was convolved with a Gaussian function, and the width of the Gaussian was iterated to match the observed step behavior of the normalized reflection contrast in the image.[36] The resultant fit is presented in Figure 3.4b, and the reflection contrast data are well modeled with a Gaussian width (σ) corresponding to an estimated lateral resolution of 1.0 μm. This lateral resolution is only slightly larger than the resolution limit of the microscope optics and camera at this magnification (~0.67 μm).

The normalized reflection contrast as a function of index corrected material thickness is presented in Figure 3.5 for three different wavelength ranges. Using a 500-550 nm bandpass filter (Figure 3.5a), the reflection contrast becomes more negative as the adsorbed surface layer

becomes thicker, while the reflection contrast becomes more positive when the same sample is imaged using a 525-1000 nm bandpass filter (Figure 3.5b). Linear regressions were calculated for both of these sets of data and are presented in the figures. In other wavelength regions, more complex reflection contrast behavior, such as the data presented in Figure 3.5c for reflection images collected using a 570-1000 nm bandpass filter; a simple linear regression is clearly inadequate to mathematically approximate the experimental behavior. This complexity is attributed to that of the underlying surface plasmon modes and their changes in response to the adsorbed surface material.

Error bars are included on the plots in Figure 3.5, but they are obscured by the data markers themselves. The relative standard deviations of the pixel values in the calibration images was ~2-5%, but the standard error calculated through a formal propagation of error was significantly smaller as a result of the number of pixels (50,000+) used to determine the averages.

Additional FDTD calculations were carried out to investigate the changes in the simulated reflection spectrum of the plasmonic crystal with increasing polyelectrolyte thickness. Figure 3.6a presents the reflection spectra for plasmonic crystal systems with increasing polyelectrolyte layer thickness, and these simulated spectra reveal a complex behavior akin to that seen in the reflection imaging calibrations. Some wavelength ranges (such as ~675-770 nm) exhibit a decrease in reflectance with larger polyelectrolyte thicknesses while the opposite trend is observed in other wavelength ranges (*e.g.* ~770-820 nm).

As a comparison, the simulated reflectance spectra for LBL films on flat gold surfaces (rather than the nanostructured ones used experimentally and used in the modeling for Figure 3.6a) are presented in Figure 3.6b. Above ~530 nm, the reflectance spectra show monotonically

decreasing reflectance with larger polyelectrolyte layers, although the magnitudes of the reflectance changes do exhibit a dependence on wavelength. This flat film modeling accounts for Fresnel effects associated with light interacting with and passing through boundaries between layers with different refractive indices but otherwise lacks any plasmonic properties; the 'contrast inversion' observed experimentally and in the simulation results presented for the nanostructured systems must be due to the behavior of the underlying surface plasmon resonances. Additionally, comparison of the modeling results in Figure 3.6 reveals that the nanostructured plasmonic system exhibits larger reflectance changes in certain wavelength regions (~770-820 nm) than the flat gold film case; this should translate into higher sensitivity to changes in surface layer thickness in this wavelength region (albeit with a more complex optical response).

It is important to note, however, that the results presented in Figure 3.6 were obtained from simulations in which the illumination was normally incident to the surface. The reflection images obtained experimentally used an objective lens with a numerical aperture of 0.40, corresponding to a cone of illumination with a maximum angle of ~23°. This is significant because previous studies show a dependence of the spectral properties of related plasmonic crystal geometries on illumination angle.[35] While the computational modeling performed here offers insight into the complexity behind the observed reflection behavior, a more complete theoretical understanding will require simulations that incorporate those oblique illumination angles which is not currently possible with our FDTD code.

3.4.3 Reflection Imaging of *Aplysia* Pedal Neurons Cultured on Plasmonic Crystals

Aplysia californica pedal neurons were cultured on plasmonic crystal surfaces (six to eight neurons at a time) and imaged using bandpass filters as a demonstration of the ability of

this plasmonic reflection imaging to quantitate surface layer thicknesses. Figure 3.7a and Figure 3.7b present reflectance images of a neuron cultured on nanostructured plasmonic crystal surface, while Figure 3.7c and Figure 3.7d are images of a different neuron cultured on a flat gold surface. A cursory comparison of the images collected using a 500-550 nm bandpass filter (Figure 3.7a and Figure 3.7c) and a 525-1000 nm bandpass filter (Figure 3.7b and Figure 3.7d) clearly reveals the differences in contrast inversion that was observed in the calibration images and the computational modeling. The peripheral regions of the neurons cultured on flat gold appear darker than the surrounding area in both the 500-550 nm and 525-1000 nm images, while the analogous regions of the cell grown on the plasmonic substrate show an inversion in contrast. (The peripheral region appears darker than the surrounding area in the 500-550 nm image but lighter than the surrounding area in the 525-1000 nm image).

These cultured neurons have features that range in thickness from tens of nanometers to several microns, while surface plasmon effects are generally assumed to be sensitive to refractive index changes only within ~100-200 nm of the metal surface. The neuron soma appears very dark in both sets of images, with anomalously bright fringes in different locations, and these are likely the result of a convolution of optical phenomena including surface plasmon-mediated reflection; light absorption, reflection, and scattering by cellular structures further away from the cell-plasmonic crystal interface; and interference effects. This current work focuses only on those features within the plasmonic sensing volume (up to ~100 nm from the surface), although the examination of these thicker structures may be of interest for follow-up studies.

The reflection contrast calibrations presented in Figure 3.5 were applied to the reflection images shown in Figure 3.7a and Figure 3.7b to determine the thicknesses of the material present in the image. (It is worth emphasizing that although the calibrations were calculated using thin

films of polyelectrolytes, the calibrations applied here used the index corrected thicknesses, θ, calculated from the ellipsometric data for biological materials.) The normalized reflection contrast was calculated pixel-by-pixel in the cell image based on the average pixel intensity in an area with no apparent features immediately adjacent to the cell; this area was thus used as the normalization reference. The normalized reflection contrast was then transformed mathematically to index corrected material thicknesses using the appropriate regression equation corresponding to the bandpass filter used to acquire the original image.

The thickness transformations for the cell image collected using a 500-500 nm bandpass filter are presented in Figure 3.8a and Figure 3.8b, and those for the 525-1000 nm bandpass filter are presented in Figure 3.8c and Figure 3.8d. Figure 3.8b and Figure 3.8d are tilted three-dimensional projections of the corresponding data presented in Figure 3.8a and Figure 3.8c and are intended to help emphasize the profile of the neuron outgrowth features in the lower left region of the image compared to the surrounding areas. In processing these thickness transformations, the normalized reflection contrast values in the cell image were restricted to values corresponding to θ between 0 and 80 nm. Pixel values outside of this range were truncated and set to either the minimum or maximum allowed reflection contrast value (based on whether the contrast value of the pixel was above or below the allowed range), leading to regions in the images presented in Figure 3.8 where θ is 'saturated' at 0 nm or at 80 nm. The neuron soma is reasonably expected to have a thickness significantly larger than 80 nm (and thus falling outside of the plasmonic sensing volume); while thickness estimates were made for these regions of the image, they clearly cannot be valid. The analyses performed in this work focus instead on the thinner neurite outgrowths and growth cone regions in the lower left portion of the images which are arguably more interesting, considering that these regions are the locations for cell

growth and spreading on the substrate. Images from both wavelength regions reveal a sparse 'film' of material in this region with thicknesses of ~30 nm relative to the surrounding area and string-like filaments with thicknesses of ~60 nm relative to the surroundings.

Although there are areas in the images where no cell structures are present, it bears mentioning that even these ‘empty’ regions would actually have a thin film of poly-L-lysine present; this layer was applied to the plasmonic crystal surface to improve the biocompatibility of the substrate. The contributions of this cell adhesion layer to the estimated thicknesses are expected to be minimal, however, because of the thickness of this poly-L-lysine layer (1-2 nm) as well as its presence in both the cell growth regions and the ‘empty’ reference regions. (In calculating the normalized reflectance contrast, the contrast associated with the poly-L-lysine layer would effectively cancel out.) Heterogeneities in the thickness of this layer would result in additional baseline noise, but this does not appear to have significantly affected the results presented.

3.4.4 Self-Consistency of Quantitative Thickness Estimates

These thickness calibrations were readily applied to images captured using different bandpass filters, but a key performance indicator of this imaging protocol is the self-consistency of the thickness estimates obtained using different wavelength intervals. Figure 3.9 presents the same thickness data (θ) for the cell obtained using the 500-550 nm (Figure 3.9a) and 525-1000 nm (Figure 3.9c) bandpass filters, and height profiles along the red lines drawn in the cell images are presented in Figure 3.9b for the 500-550 nm bandpass filter and in Figure 3.9d for the 525-1000 nm bandpass filter. The red lines correspond to the same region in each image. The effect of truncating the contrast values in the image prior to application of the thickness calibration is

particularly apparent in the line profile for the 525-1000 nm image (Figure 3.9d) where many pixels were assigned a thickness of zero.

Comparisons of the height profiles between the two wavelength intervals show they are broadly consistent, supporting the utility of this plasmonic imaging method for quantitative thickness imaging. Despite the truncation in the 525-1000 nm image, good agreement is observed for the height of the filament feature at position X ~40 μm – both wavelength ranges assign a thickness of ~60 nm to this feature. Good correspondence is also observed for the feature at X ~ 100 μm (thickness ~50 nm). The agreement between the two images is poorer for features with smaller thicknesses, however. At X positions between 50-90 μm, the 525-1000 nm image (Figure 3.9c) reveals more structure than is found in the 500-550 nm image. This discrepancy may arise from the relatively coarse regressions applied to the calibration imaging data; while the regressions for both wavelength ranges appear roughly linear, the corresponding regression equation may de-emphasize or over-emphasize the contrast change in particular thickness ranges. A more fine-grained regression analysis, calculated over subsets of the layer thicknesses imaged or using more complex mathematical fits, may yield improved consistency between wavelength regions. Alternatively, these simple regressions could be retained and images from different wavelength regions used to examine areas within a particular thickness range.

3.4.5 Atomic Force Microscopy (AFM) Height Profiles of Cell Features

Independent verification of the heights determined through this reflection imaging contrast method was performed using atomic force microscopy in the same region as that used to produce the height profiles in Figure 3.9. An image of the AFM data is presented in Figure

3.10a and reveals a periodic modulation arising from the underlying nanostructured plasmonic crystal surface. A scanning electron micrograph of a different cell is presented in Figure 3.10b, and these figures suggest that these thinner cell outgrowth regions conform, at least partially, to the plasmonic crystal's surface topography while thicker layers appear to be less strongly affected.

The periodic modulation from the underlying substrate is not observed in the reflection images, however, because the individual nanoholes (~450 nm in diameter) are smaller than the length scales resolved by the camera at this magnification (each pixel corresponds to a lateral distance of ~670 nm). While the center-to-center spacing between holes is ~740 nm, a single pixel in the image may overlap part of one or several nanoholes depending on the optical alignment. It is reasonable that the reflectivity may not be identical between the top and bottom surfaces of the nanohole, and the pixel intensity could vary somewhat due to differences in nanohole coverage. While no particular pattern was observed in histograms of the pixel intensities in the calibration images, this nanohole coverage effect would contribute to the variance in the data with a corresponding increase in the standard deviation. Image smoothing, such as a Gaussian blur with a tightly restricted radius, can be employed to reduce these pixel intensity variations and ultimately reduce the size of the error bars in the calibration plots. However, no such steps were taken in this work.

The periodic modulation in the AFM data introduced by the surface topography adversely affects the interpretation of thickness information from the data in this region. As a remedy, the periodic oscillations were filtered out using a Fast Fourier Transform (FFT) of the image where all but the lowest frequency components were removed from the image. A 3D projection of the raw AFM data is presented in Figure 3.10c for comparison with a 3D projection of the FFT

filtered data in Figure 3.10d. These images clearly show that the effects of the periodic nanostructures on the surface have been significantly reduced, but there is a loss in apparent image sharpness as a result of the filtering. Despite this loss of lateral detail, the FFT filtered image is much more suitable for estimating the feature height thicknesses. Future research directions may pursue optical imaging at higher magnifications at which point the individual nanoholes will become discernable in the image. A more refined version of the FFT filtering method used here may prove useful in removing the periodic structures in those future images.

A comparison of the cell feature thickness estimates based on reflection imaging and AFM measurements is presented in Figure 3.11. The line cut area in the 525-1000 nm reflectance image (Figure 3.11a) has been adjusted to better match that of the region profiled using the atomic force microscope, and the corresponding height profile is presented in Figure 3.11b. The FFT filtered AFM data is presented in Figure 3.11c, and a height profile along the red line drawn is shown in Figure 3.11d. These data reveal a remarkable correspondence between the thickness estimates of the filament structure at X ~ 40 μm in the reflectance image (Figure 3.11a,b) and at X ~ 35 μm in the AFM image (Figure 3.11c,d); both methods assign a thickness of ~60 nm to this structure.

The AFM data collected provide independent confirmation of the thicknesses estimated using the thin film reflectance contrast calibrations, and this result is significant for several reasons. First, the AFM data validates the estimate of the refractive index of the surface material that was used in converting the polyelectrolyte layer thicknesses to the equivalent index corrected material thicknesses. The cell material was assumed to have a refractive index of 1.50 based on the literature reports of the refractive indices of proteins, lipids, and cell membranes. Other sources report a refractive index range of 1.35 – 1.41 for cell components such as the

cytoplasm and organelles. However, these values are derived from live cells whereas the cells in this work have been fixed and desiccated to some degree; this would have the effect of concentrating the species present in the cell which have raised the refractive index from that of the baseline value for water (n = 1.33).

Had the thicknesses differed significantly, the AFM data could itself have been used as a calibration target for the ellipsometric modeling, where the refractive index of the index corrected material could be adjusted to achieve good correspondence with the AFM data. This result would provide additional information regarding the nature of the material on the plasmonic crystal surface (*i.e.* its refractive index). In this manner, the AFM measurements and the reflection imaging synergistically provide information about both the topography and the composition of the cell material on the plasmonic crystal surface.

The second significant outcome is that this reflection imaging on plasmonic crystal surfaces has the potential to complement atomic force microscopy for revealing topographic details for thicknesses up to ~100 nm. The use of surface plasmon effects to gauge material thicknesses at the metal-dielectric interface is limited to the depth of the plasmon sampling volume, while atomic force microscopes can measure thicknesses that are several orders of magnitude larger. However, this plasmonic imaging method is capable of measuring these surface thicknesses over large areas within seconds; the AFM would take significantly longer to measure a much smaller area. Quantitative reflection imaging is thus capable of monitoring dynamic processes (such as live cell growth) in near-real time, and image acquisition parameters (such as wavelength range, acquisition times, and magnification) can be optimized for specific applications.

Furthermore, the thickness quantitation demonstrated here for films on plasmonic crystals was performed without the need for specialized equipment. The plasmonic crystal itself can be easily and inexpensively replicated via a soft nanoimprint lithography process, and the imaging was performed using a standard optical microscope with a halogen illuminator and a typical charge-coupled device camera. Bandpass filters are commercially available with wavelength ranges covering the visible and near-infrared wavelengths and passbands of nearly arbitrary width. While further investigation of the capability of these plasmonic crystals for quantitative reflection imaging is certainly warranted, these results suggest that they are able to measure surface layer thicknesses at nanometer scales in real time.

3.4.6 Increased Image Contrast through Wavelength Combination

Imaging detectors, such as the charge-coupled device camera used in this work, integrate the photon flux across the accessible wavelength range. A decrease in the number of photons at one wavelength within that range (corresponding to a decrease in reflection) can be offset by an increase in photons at a different wavelength, and this integration ultimately results in reduced image contrast if the wavelengths imaged overlap spectral regions with opposite contrast behavior. Bandpass filters allows these spectral regions to be isolated from one another and analyzed separately in a form of quasi-hyperspectral imaging, albeit with relatively coarse wavelength control. By identifying wavelength regions where the reflection contrast exhibits opposite behavior and imaging these regions separately, judicious recombination of these data while accounting for the respective increases or decreases in image contrast can restore and even enhance image contrast that would otherwise have been lost.

Figure 3.12a presents thickness calibration curves obtained using 570-600 nm and 570-1000 nm bandpass filters. Because of the wavelength overlap between these two filters, the reflection behavior between 570-600 nm must be present in the data collected over 570-1000 nm, but it is convolved with the reflection behavior at all of the other wavelengths. These calibration curves show that the reflection contrast obtained using the 570-600 nm filter decreases for θ thicknesses greater than ~20 nm, but this contrast decrease is not as pronounced in the data obtained using the 570-1000 nm bandpass filter. This indicates that the reflection must tend to increase for thicker θ at wavelengths between 600-1000 nm in order to offset the behavior observed between 570-600 nm. Additionally, the 570-1000 nm data shows a larger increase in reflection contrast for thinner θ (up to ~20 nm). This calibration behavior signals an opportunity to combine the imaging data in such a way that accounts for their difference in sign (increasing or decreasing), generating increases in overall image contrast and sensitivity.

Additional knowledge of the camera detector itself is needed in order to properly combine the calibration images obtained using the 570-600 nm and 570-1000 nm bandpass filters into a single composite calibration curve. The spectral response of the CCD detector in the Olympus Magnafire camera used in this experiment is not equal across all wavelengths; its sensitivity peaks between 500-520 nm and decreases as wavelength increases.[51] In fact, the 570-600 nm bandpass filter covers only ~7% of the wavelength range between 570-1000 nm but accounts for ~18% of the total sensitivity! Thus, the contributions of the 570-600 nm wavelength range to the overall image contrast are disproportionately larger relative to the size of the passband because of the inherent spectral sensitivity of the camera.

Recognition of the sensitivity of the camera allows for a more complete processing and combination of the imaging data from both wavelength regions. Individual images using the 570-600 nm and 570-1000 nm bandpass filters were combined using the following formula:

$$\text{Composite Image} = \frac{([\text{570-1000 nm}]\times 147.75) - 2\times([\text{570-600 nm}]\times 26.55)}{147.75}$$

The individual images are weighted by the total integrated sensitivity of the wavelength range based upon the camera manufacturer's specifications, and the data from the 570-600 nm images is subtracted from the corresponding 570-1000 nm image. This subtraction takes into account the decreasing trend in reflection contrast experimentally observed and mathematically converts it to an increasing trend to match the reflection contrast behavior inferred for the rest of the 570-1000 nm wavelength range. The 570-600 nm data is subtracted twice in this analysis: Subtraction once (ideally) removes its contribution from the data collected over the entire 570-1000 nm wavelength range, and subtracting the data once restores its contribution but with the inverted trend. The resultant image was then used to calculate the normalized reflection contrast as described earlier.

The combined calibration results are plotted in Figure 3.12a, and it is readily apparent that the overall reflection contrast trend now increasing across the index corrected material thicknesses examined. Furthermore, the image contrast is in fact enhanced, with larger absolute changes in the normalized reflection contrast at larger θ. Error bars are included for the wavelength combined calibration data, but once again, they are obscured by the data markers

themselves. A power law regression was applied to the combined calibration curve because it appeared to better fit the data than a linear regresssion.

This composite calibration curve was applied to the images of the same Aplysia neuron cultured on the plasmonic crystal presented previously, and the resultant thickness estimates are presented in Figure 3.12b and Figure 3.12c. The thickness estimates show good agreement with those produced using the 500-550 nm and 525-1000 nm calibration curves. A height profile was determined along the line drawn in Figure 3.13a; this line is in the same position as those presented in Figure 3.9 for the single bandpass filter images. The height profile presented in Figure 3.13b for the combination image reveals the same structural features as those seen using the 500-550 nm and 525-1000 nm bandpass filters. In fact, the line cut presented in appears to combine elements from both previous data sets: The ~60 nm filament feature at X~50 um is present and remains in good agreement with the AFM measurements and the plasmonic reflection estimates performed in the same region, and the smaller features between X~50-90 um that were more clearly observed in the 525-1000 nm bandpass filter image are clearly present in the composite thickness calibration. These results show the efficacy of combining images acquired over different wavelength ranges to increase contrast and sensitivity in the resultant image.

3.4.7 Quantitative Thickness Estimates from Nonplasmonic Optical Effects

While the thickness quantitation methods demonstrated here rely on the sensitivity of surface plasmon resonances to changes in the refractive index profile at the metal surface, the images clearly show other areas of the cell with thicknesses significantly larger than those that can be adequately probed using the surface plasmon's evanescent electric field. Additional

nonplasmonic optical effects are present in the image, including Fresnel reflections from any interface between regions of different refractive indices along with light scattering and absorption by cellular components. Figure 3.14a presents the 500-550 nm bandpass image of the cell with particular attention drawn to the structure at the bottom of the image. Rotated and magnified views of this region acquired using 500-550 nm, 570-600 nm, and 610-700 nm bandpass filters are presented in Figure 3.14b, Figure 3.14c, and Figure 3.14d, respectively. These images reveal alternating light and dark bands moving from the lower left tip towards the upper right, and the size and position of these bands changes depending on the particular bandpass filter used.

These alternating intensity bands are reminiscent of a thin film interference effect ('Newton's rings') arising from constructive and destructive interference from light reflected within what is essentially a resonant cavity formed by the top and the bottom surfaces of the cell structure. The number and position of these bright and dark regions are functions of the wavelengths of light being imaged and the cavity length (cell structure thickness) required to produce resonant conditions. Since the wavelengths of light being imaged are known, this thin film interference effect provides an additional method by which material thicknesses in the image can be quantitated. The resonant cavity length was estimated for the second band indicated in the 500-550 nm image (Figure 1.13b) using the extreme ends of the range of wavelengths (500 nm and 550 nm) and incident angles (0° and 23.6°) along with the previous estimate of the refractive index (n~1.5). The convolution and overlap of different wavelengths with different illumination angles (as a result of the microscope objective optics) result in a range of cavity thicknesses between ~330-400 nm capable of producing constructive interference at the location highlighted in Figure 3.14b.

AFM measurements were obtained for this cell structure as an independent verification of its thickness. The FFT filtered AFM image is presented in Figure 3.14e, and a height profile along the line drawn is presented in Figure 3.14f. The thickness of the feature in the AFM images is ~400 nm at approximately the same location as the area analyzed from Figure 3.14b. Once again, the AFM and optical thickness estimates are in good agreement.

This thin film interference based thickness quantitation is advantageous as a complement to the surface plasmon-based estimates. The thin film interference calculations have the advantage that they can be performed without prior calibration, and they can estimate thicknesses larger than those possible using only plasmonic effects. This capability does not come without drawbacks, however. The thickness range estimates can become very broad when imaging large wavelength ranges, and the nature of the microscope objectives themselves results in a range of thicknesses capable of producing constructive or destructive interference at a location, even if the sample was illuminated with monochromatic light. The minimum thickness required to observe thin film interference effects is one-half of the wavelength (or one-fourth, if reflection from the upper surface results in a 180° phase shift). Even for 400 nm illumination at normal incidence, this corresponds to a minimum thickness of 100 nm – at the upper limit for quantitating thicknesses using plasmonic calibrations. While these considerations constrain the use of thin film interference effects to quantitate material thicknesses, they also reveal possibilities for a synergistic integration of both methods where plasmonic calibrations can be used to quantitate surface thicknesses up to ~100 nm, and thin film interference can be used to estimate larger thicknesses.

3.4.8 Inferences Regarding Cell Structures Observed on Plasmonic Crystals

While thickness estimates of the material present on the plasmonic crystal surface provide quantitative information regarding the neuron's outgrowth behavior prior to fixation, the thickness estimates themselves provide little information regarding the function of those structures. The growth and extension of neurites from the *Aplysia* pedal neuron body begins with the emergence of growth cones, which can be very large (tens to hundreds of microns).[41] The growth cone is defined by a thicker central region, where vesicles and microtubules can be found, and a surrounding thinner 'veil' composed of lamellipodia and filopodia.[41,52,53] As the cell matures, this peripheral region is resorbed as the neurite thickens and rounds,[41,54] and it is likely that the thin film regions examined in these plasmonic images reveal stages of this neurite outgrowth process.

Figure 3.15a presents the cell image with thickness correlations from the combined 570-600 nm and 570-1000 nm calibrations applied. The structure labeled 'A' in the image appears to be a neurite which has fully formed (with a corresponding thickness of ~60 nm). The area labeled 'B' in the image appears to be a sparse distribution of thin features and may be the remnants of the peripheral region of the growth cone. Similar features are seen in the reflection image of a different cell presented in Figure 3.15b. Tracing upwards from the cell body, the darker neurite on the left side (labeled 'C') is readily distinguished from the thinner region (labeled 'D'), and the patchy nature of the surface coverage moving further away from the cell body (labeled 'E') may be indicative of the resorption or partial resorption of the peripheral portion of the growth cone. The cell structures characterized by 'Newton's rings' in the thin film interference analysis may be the central regions of the growth cones. These regions are more

readily observed in the image in Figure 3.15c, and several have been marked for ease of reference. Many of these regions appear to be surrounded by the thin 'veil' previously associated with the peripheral region of the growth cone, and the thicker nature of the central region lends credence to this identification.

The images presented in Figure 3.15 appear to show *Aplysia* pedal neurons in different stages of growth. The neurons in Figure 3.15a and Figure 3.15b have more clearly defined neurites and fewer central regions and thus may be more mature (or were allowed to grow for a longer time), while the neuron in Figure 3.15c has fewer defined neurites and many more growth cone regions. Although these same conclusions could be drawn from reflection images without the need for quantitation, the thicknesses of the cell features may be indicative of the health or function of the cell or of the nature of the interaction between the cell structure and the surface. Imaging sensitivity to thin films can be optimized in part by proper choice of the wavelength range used, and this sensitivity could be used to observe features that may not be visible in other forms of optical imaging. Additionally, while these images were acquired using fixed cells, this imaging method could be adapted for imaging the growth of live cells. One consideration for live cell growth would be a decreased refractive index contrast between the cell structures and the surrounding aqueous medium. Based upon spectroscopic transmission measurements of the bulk refractive index sensitivity, this class of plasmonic crystals should be capable of differentiating refractive index changes on the order of 10^{-3} refractive index units,[23,36] and this would be sufficient to observe a difference between water (n = 1.33) and cytoplasm (n = 1.36),[50] for example. More recent reports even suggest that reflection mode measurements may be more sensitive to changes in refractive index.[55] These potential applications certainly call for additional investigations.

3.5 Conclusions

In this work, nanoimprinted plasmonic crystals were used to perform label-free reflection imaging capable of quantitating the thickness of thin films present on the metal surface. Calibrations based on polyelectrolyte layer-by-layer assemblies were applied to *Aplysia* pedal neurons cultured on the plasmonic crystal surface to estimate the thickness of cell structures produced during the neurons' growth, and these thicknesses were confirmed using atomic force microscopy. The use of bandpass filters to restrict the wavelengths of light imaged can improve image contrast and sensitivity, with further improvements possible by the post-acquisition combination of images captured using different wavelength ranges. Significant improvements to image contrast and sensitivity may be possible through optimization of the plasmonic crystal structure and metal thicknesses in tandem with investigations of reflection contrast over different wavelength ranges. Additional computational studies incorporating non-normally incident angles could provide insight into the plasmonic phenomena underlying the experimental results and provide theoretical guidance for design of the plasmonic crystal and the wavelengths used. This plasmonic reflection imaging holds great promise for detailed investigations of the interactions between live cells and their substrates, all in a fully label-free, quantitative format using otherwise common laboratory equipment.

3.6 Acknowledgments

I gratefully acknowledge the contributions of my collaborators towards this work: Lucas Thompson for his useful discussions and ideas on experimental design and image analysis as well as his assistance in preparing this chapter, and within the Sweedler research group, Xiying

Wang for preparing the *Aplysia* cell cultures and Stanislav Rubakhin for preparing the *Aplysia* cell cultures and his enlightening discussions. My contributions to this work include fabrication of the plasmonic structures, polyelectrolyte LBL growth, reflection imaging and analysis of both the polyelectrolyte films and the cultured cells, atomic force microscopy and scanning electron microscopy of the cultured cells, and FDTD simulations. This work was supported by the U. S. Department of Energy and was performed using resources at the Frederick Seitz Materials Research Laboratory Central Facilities at the University of Illinois, including the Center for Microanalysis of Materials, which is supported by the U.S. Department of Energy, Basic Energy Science, Materials Science and Engineering Division under Award No. DE-FG02-07ER46471; the Micro/Nanofabrication Facility; and the Laser and Spectroscopy Facility. I also gratefully acknowledge the use of the Turing cluster, maintained and operated by the Computation Science and Engineering Program at the University of Illinois.

3.7 Figures

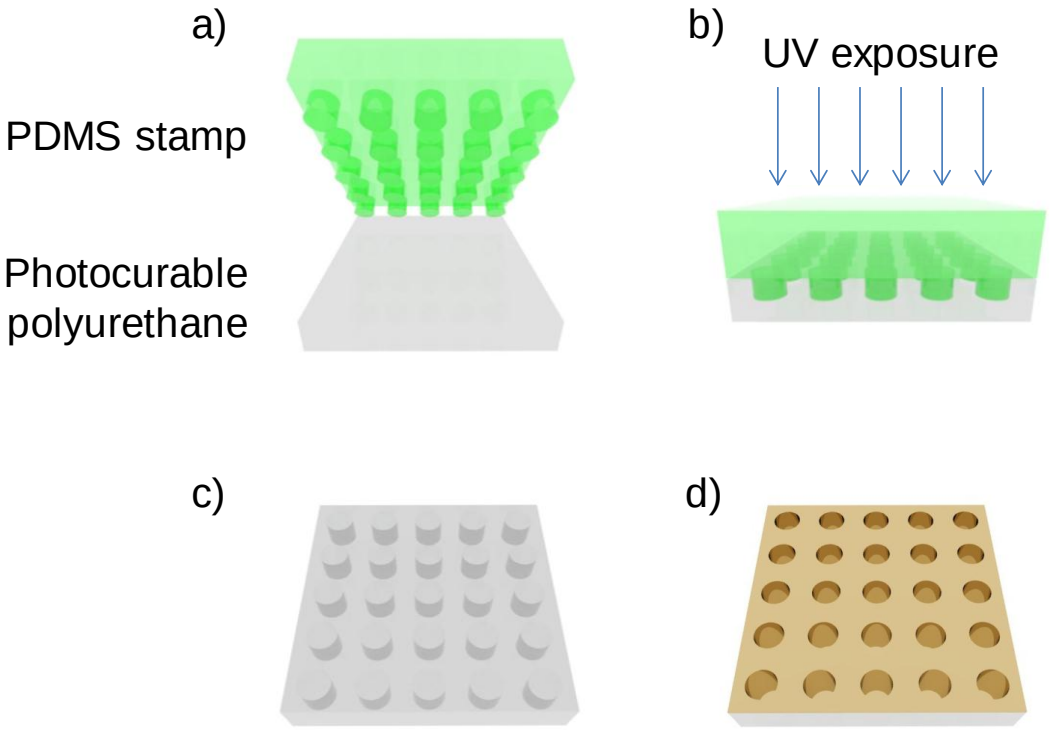

Figure 3.1: Schematic of the soft nanoimprint lithography process for fabrication of plasmonic crystals: a) A nanostructured PDMS stamp is originally cast from a square nanohole array master and used to imprint a photocurable polyurethane cast onto a glass slide. b) The stamp is pressed into the polyurethane, and the assembly is exposed to ultraviolet light to cure the polymer. c) The stamp is removed, leaving a replica of the square nanohole array in the polymer. d) An adhesion layer (TiO2) and a metal (Au) are sputter coated onto the patterned polymer surface to create the plasmonic crystal.

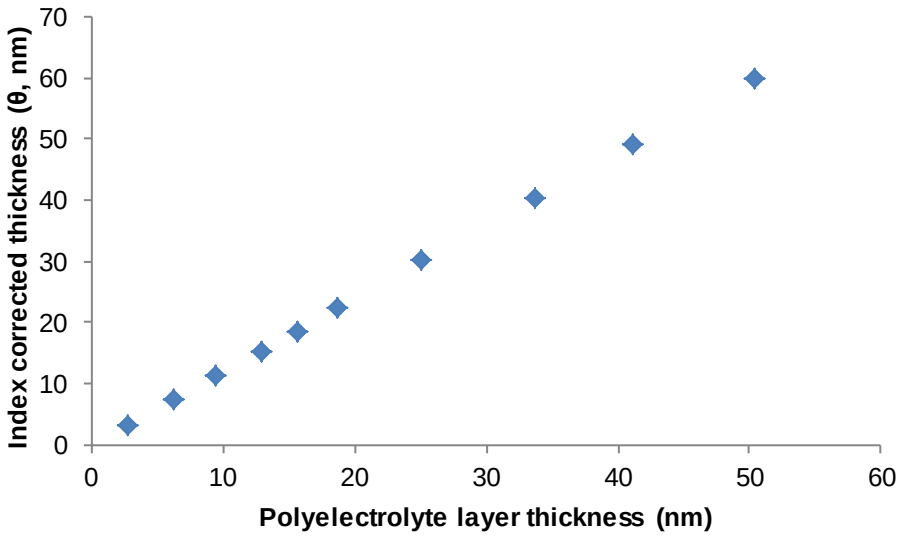

Figure 3.2 Correlation between ellipsometrically determined polyelectrolyte (n = 1.64) layer thicknesses and index corrected material (n = 1.50) thicknesses.

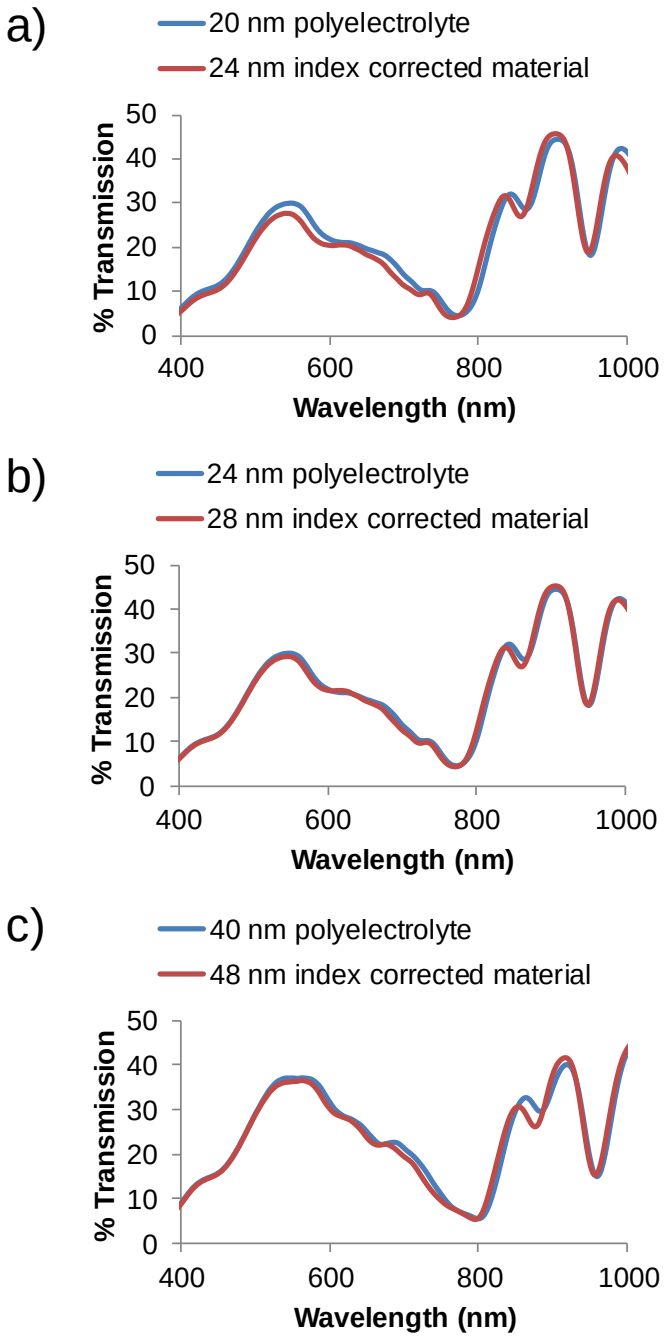

Figure 3.3 FDTD simulated transmission spectra for pairs of ellipsometrically equivalent polyelectrolyte and refractive index corrected thin films conformally covering a plasmonic crystal: a) 20 nm polyelectrolyte, 24 nm index corrected material; b) 24 nm polyelectrolyte, 28 nm index corrected material; c) 40 nm polyelectrolyte, 48 nm index corrected material.

a)

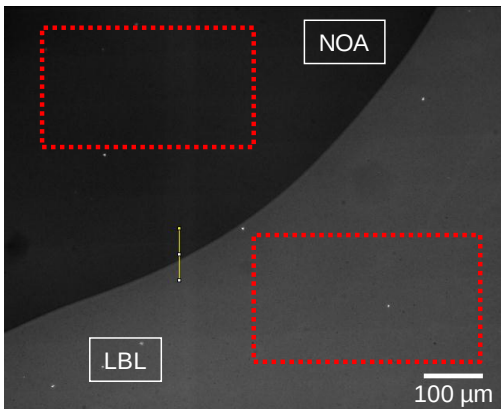

b)

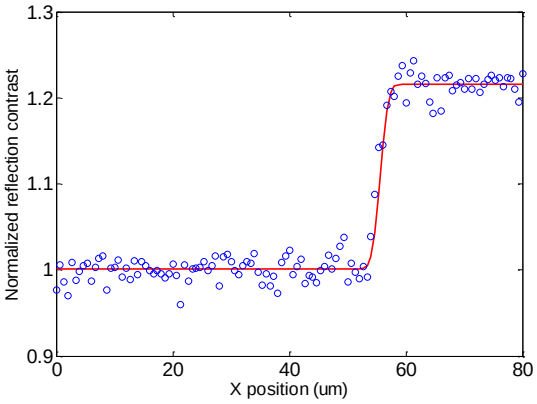

Figure 3.4 a) Example of a characteristic image of a polyelectrolyte layer-by-layer film deposited on a plasmonic crystal used for the calibration of reflection contrast. This image was acquired using a 500-550 nm bandpass filter. 'LBL' denotes region where polyelectrolyte films were grown, and 'NOA' denotes region where a drop of polyurethane was cured to block polyelectrolyte film deposition. Average pixel intensities were calculated in the regions marked with red boxes and used to determine the reflection contrast calibration. b) Normalized reflection contrast step edge profile (blue circles) along yellow line drawn in panel a with a fitted curve (red line) with a Gaussian width of 1.0 µm.

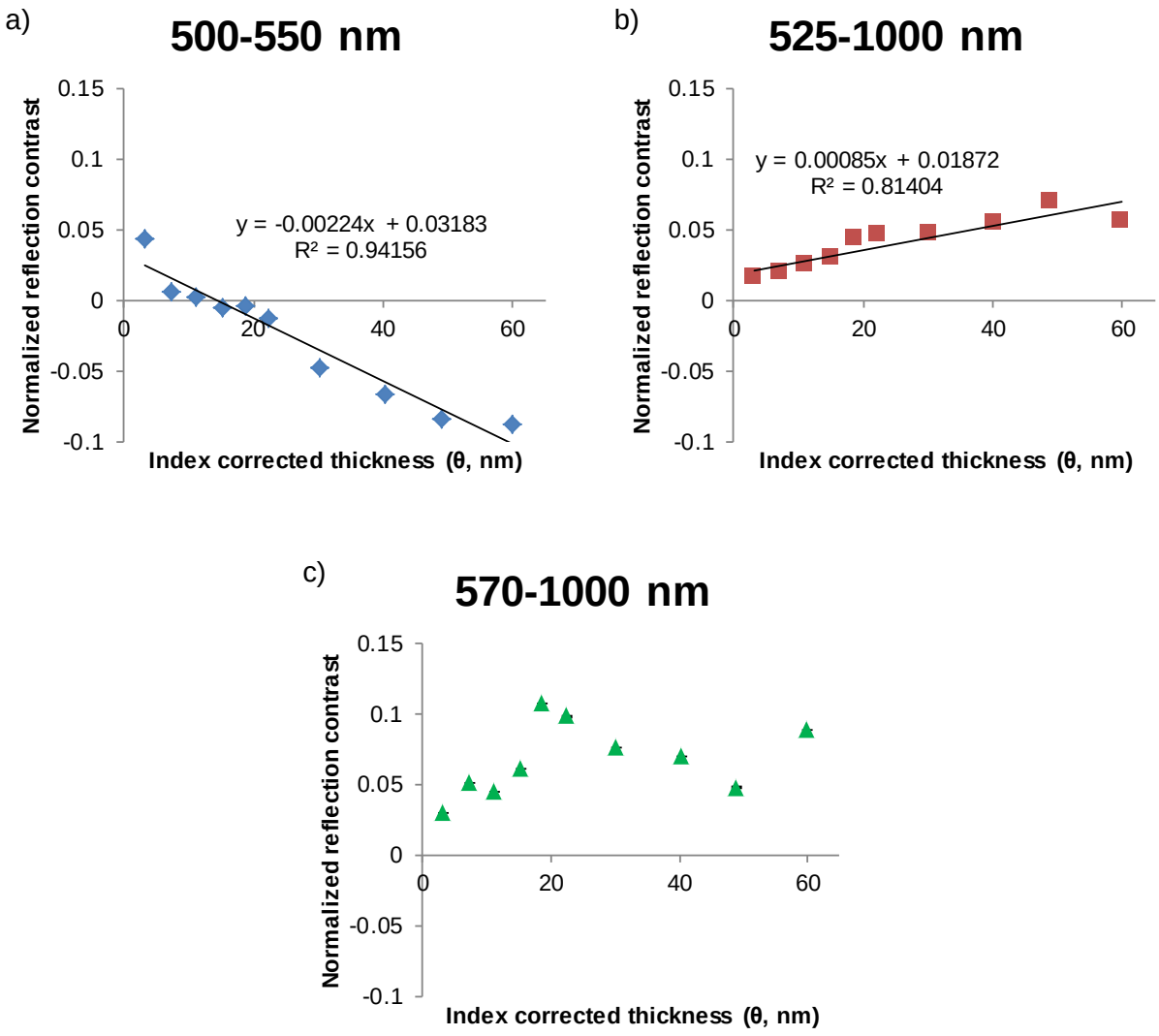

Figure 3.5 Calibration data for normalized reflection contrast as a function of adsorbed index corrected material thickness for images acquired using bandpass filters: a) 500-550 nm, b) 525-1000 nm, c) 570-1000 nm. Error bars calculated using a formal propagation of error are included on each plot but are of the order of the size of the data symbols, and linear regressions were calculated for the data in panels a and b.

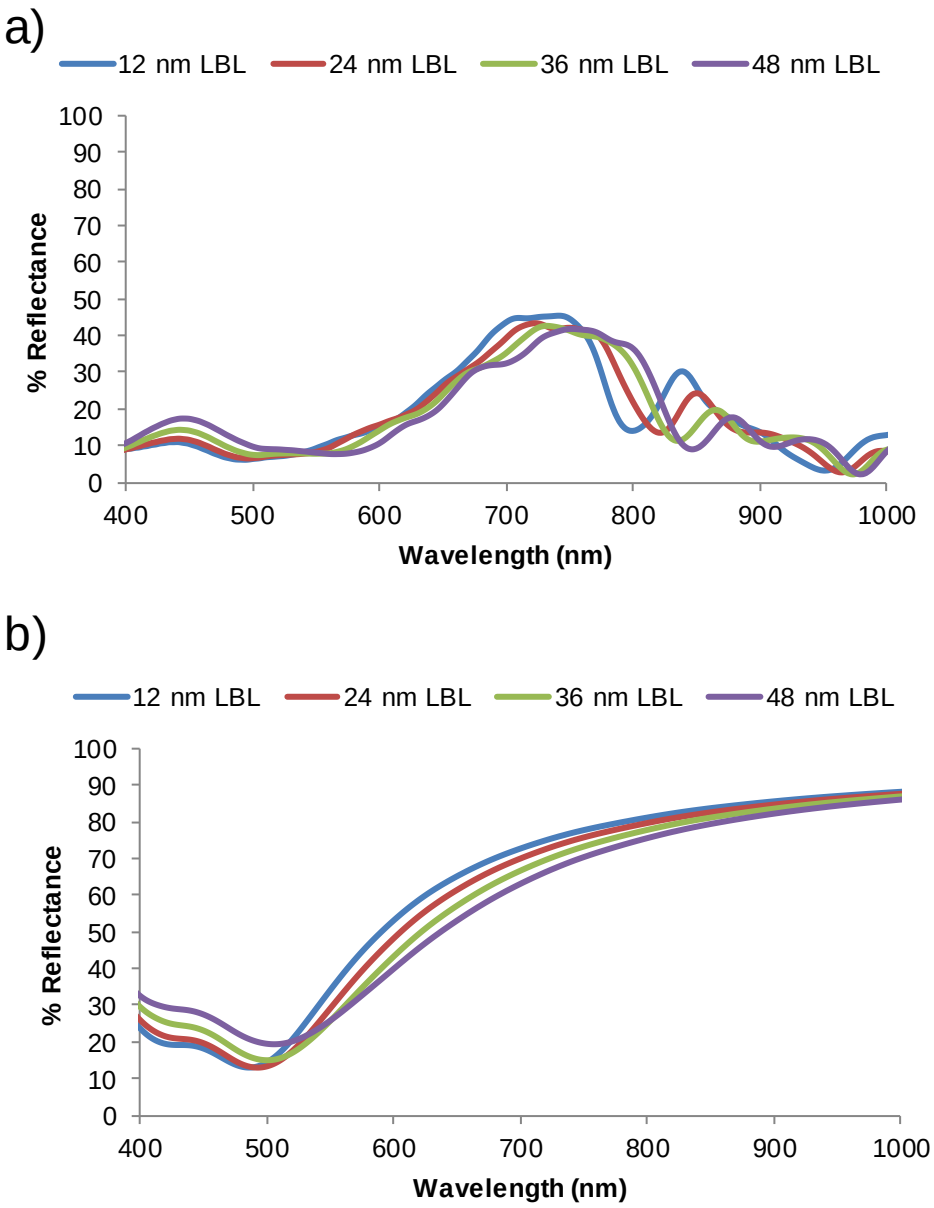

Figure 3.6 FDTD simulated reflection spectra for different polyelectrolyte layer thicknesses on a) nanostructured gold plasmonic crystal surface and b) flat gold surface. The reflection spectra in panel a clearly show more complex reflection characteristics than those observed on the flat gold surface.

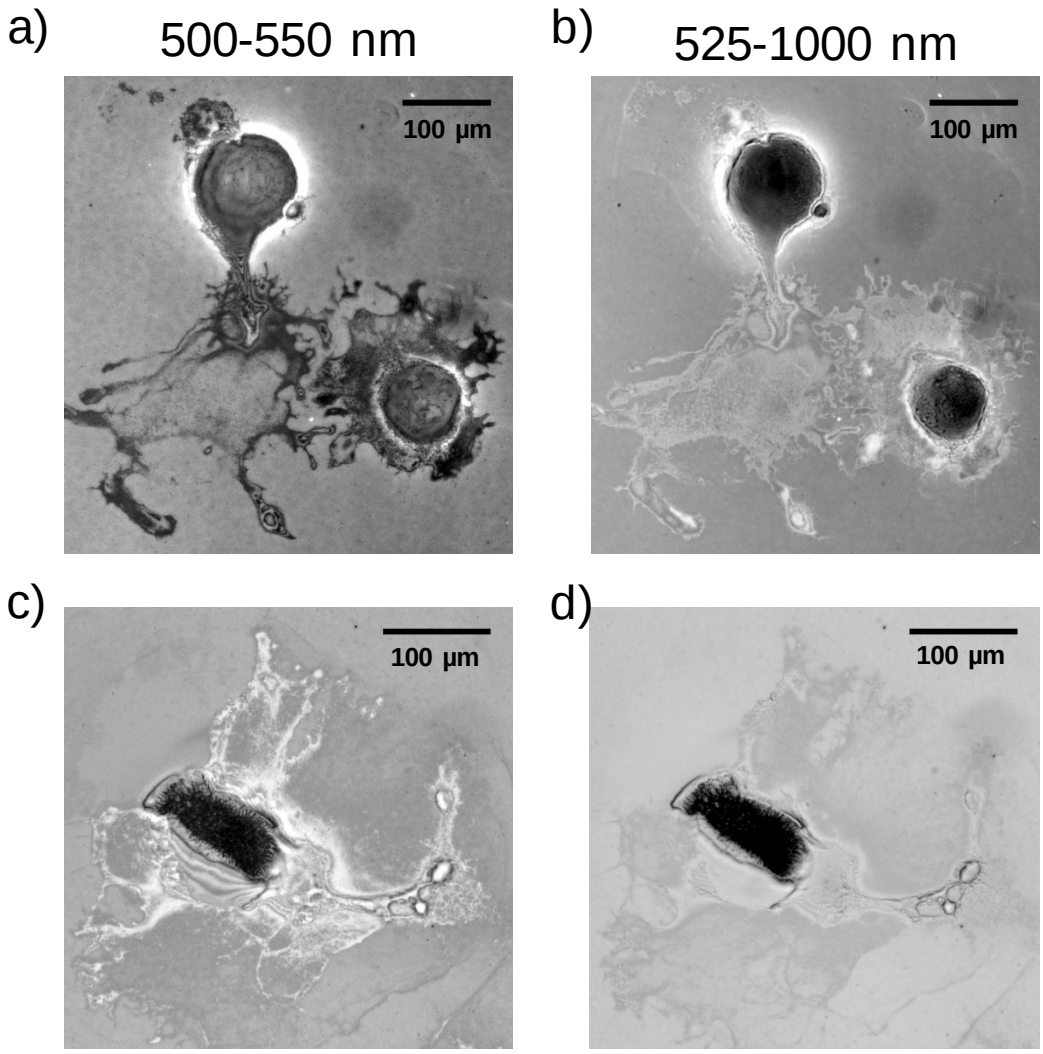

Figure 3.7 Reflection images of *Aplysia* pedal neurons cultured on a plasmonic crystal surface (a, b) and on flat gold (c, d). Images in panels a and c were acquired using a 500-550 nm bandpass filter, and images in panels b and d were acquired using a 525-1000 nm bandpass filter. Images of cells grown on plasmonic crystals (a,b) clearly show contrast inversion, where the thin cell regions in the lower left portion of the image are darker (a) or lighter (b) than the surrounding area, depending on the wavelength range. Images of cells on flat gold (c,d) do not show this inversion.

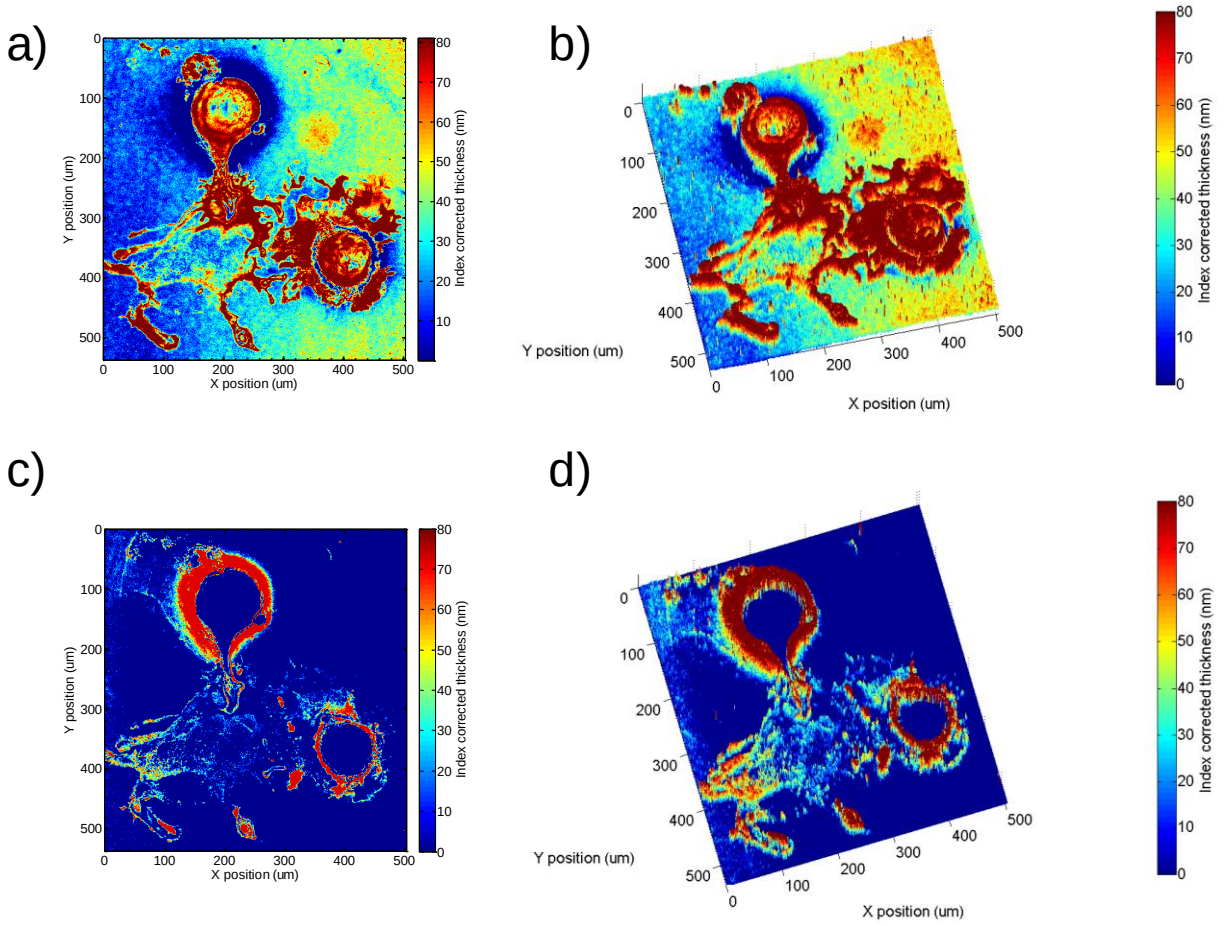

Figure 3.8 Index corrected thickness calibrations applied to reflection images of *Aplysia* pedal neurons cultured on a plasmonic crystal surface acquired using 500-550 nm (a, b) and 525-1000 nm (c, d) bandpass filters. Tilted 3D projections of index corrected thickness data are presented in panels b and d.

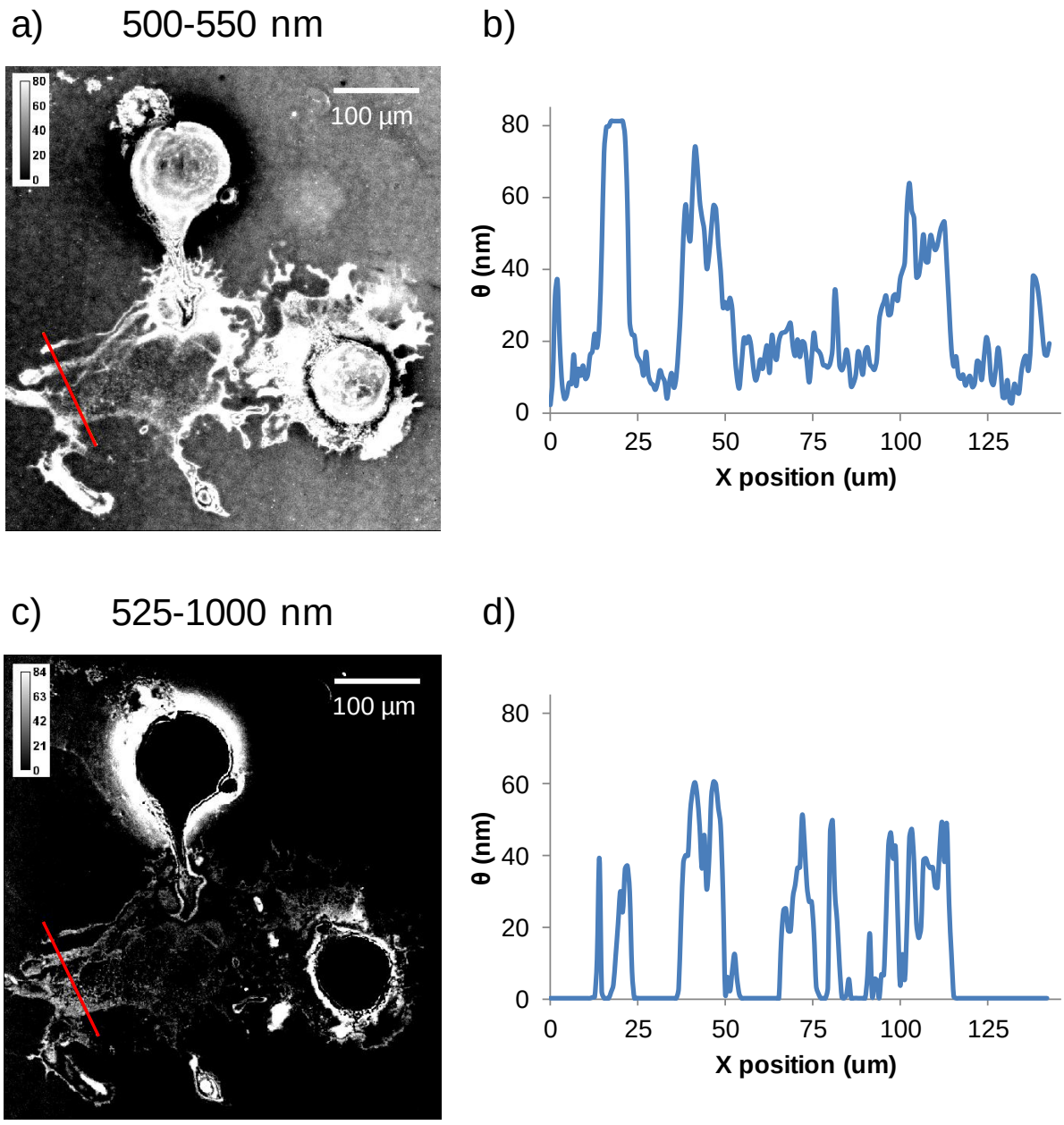

Figure 3.9 Index corrected thickness calibrations applied to reflection images of *Aplysia* pedal neurons cultured on a plasmonic crystal surface acquired using 500-550 nm (a, b) and 525-1000 nm (c, d) bandpass filters. Red lines in panels a and c denote image areas where the index corrected material thickness (θ) profiles in panels b and d were calculated.

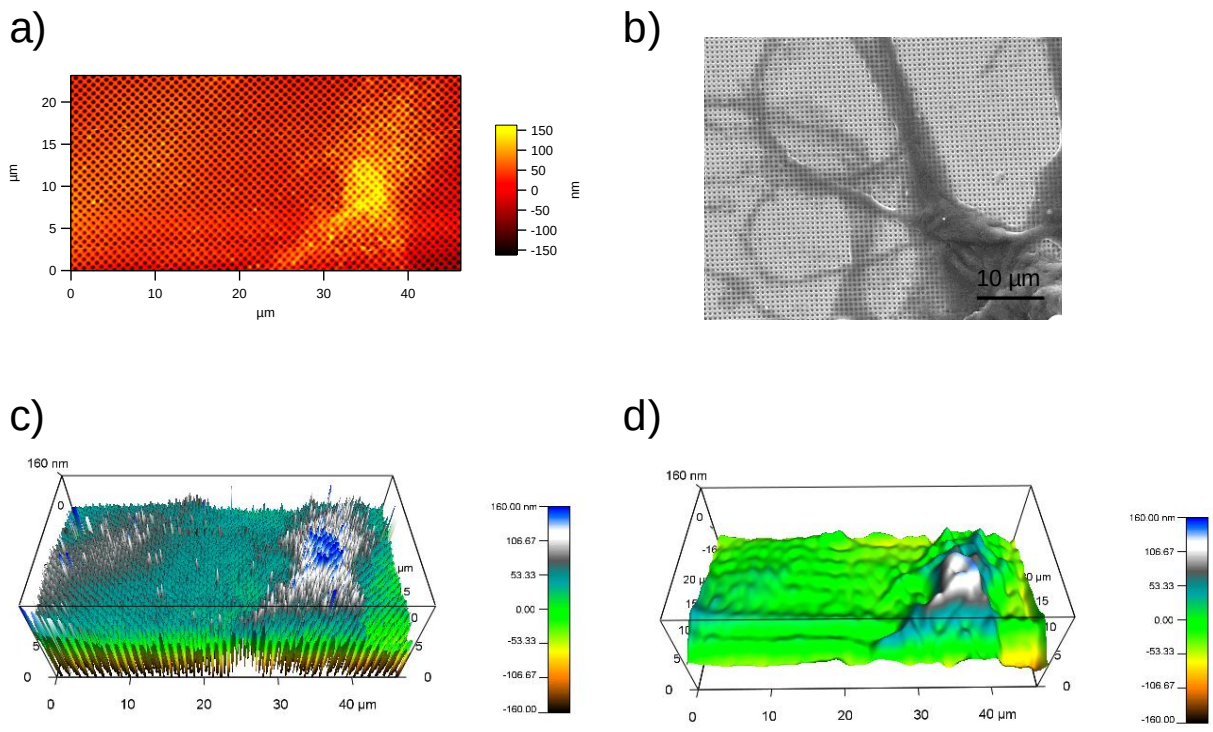

Figure 3.10 a) Atomic force microscopy measurements of an *Aplysia* pedal neuron cultured on a plasmonic crystal surface showing modulations on the surface due to the underlying plasmonic nanostructure. b) Scanning electron microscope image of a portion of an *Aplysia* pedal neuron cultured on a plasmonic crystal surface showing the nanostructured surface visible underneath the cell structures. c) 3D projection of the original AFM data shown in panel a prior to fast Fourier transform filtering. d) 3D projection of AFM data from panel a after fast Fourier transform filtering to remove plasmonic nanostructure contributions from data.

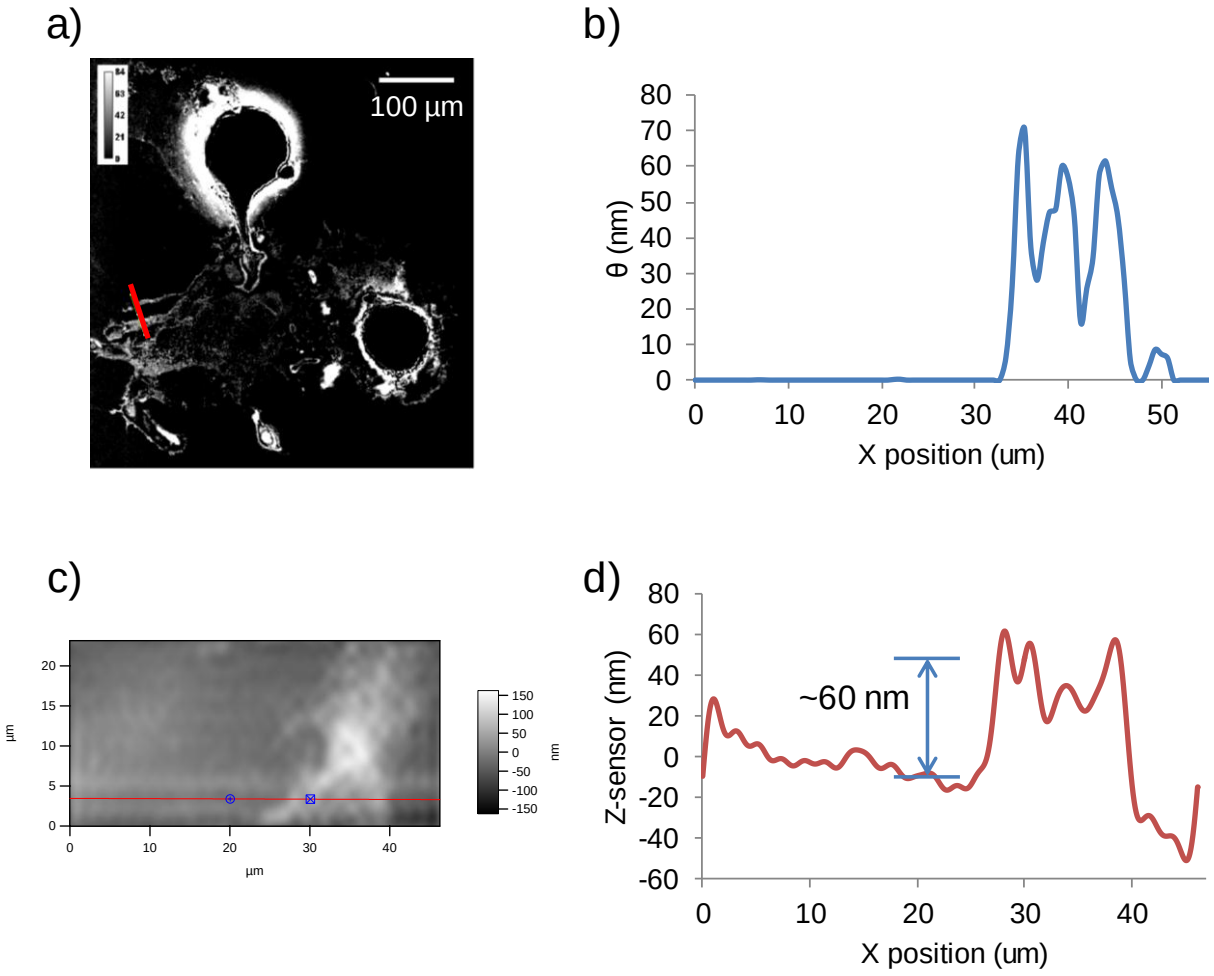

Figure 3.11 a) Reflection image (525-1000 nm bandpass filter) of *Aplysia* pedal neurons cultured on a plasmonic crystal surface with index corrected thickness calibrations applied. b) Height profile along the red line drawn on the image in panel a. c) FFT filtered AFM image of the *Aplysia* pedal neuron feature highlighted in panel a. d) Height profile along the red line drawn on the image in panel c. Feature height estimates are consistent between the reflection and AFM images.

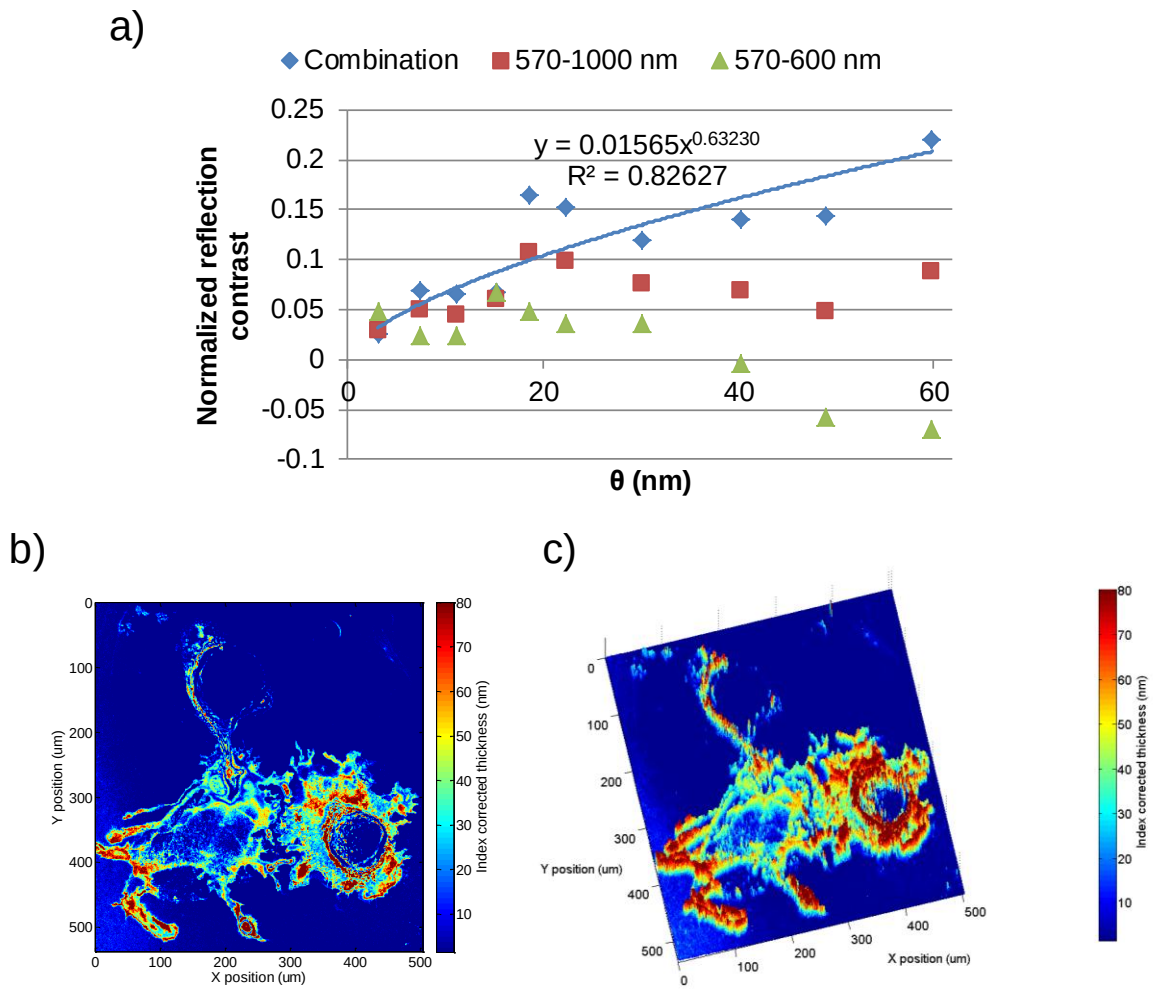

Figure 3.12 a) Normalized reflection contrast calibration curves as a function of index corrected material thickness for images acquired using bandpass filters: 570-600 nm (green triangles), 570-1000 nm (red squares) and after combination of these wavelength regions (570-600 nm combined with 570-1000 nm, blue diamonds). A power law regression was applied to the combination calibration curve. Error bars derived from formal propagations of error are included for the combination calibration curve only but are of the order of the size of the data symbols. b) Wavelength combined (570-600 nm and 570-1000 nm) reflection contrast calibration applied to combined wavelength image of *Aplysia* pedal neuron cultured on plasmonic crystal surface. c) Tilted 3D projection of index corrected thickness data presented in panel b.

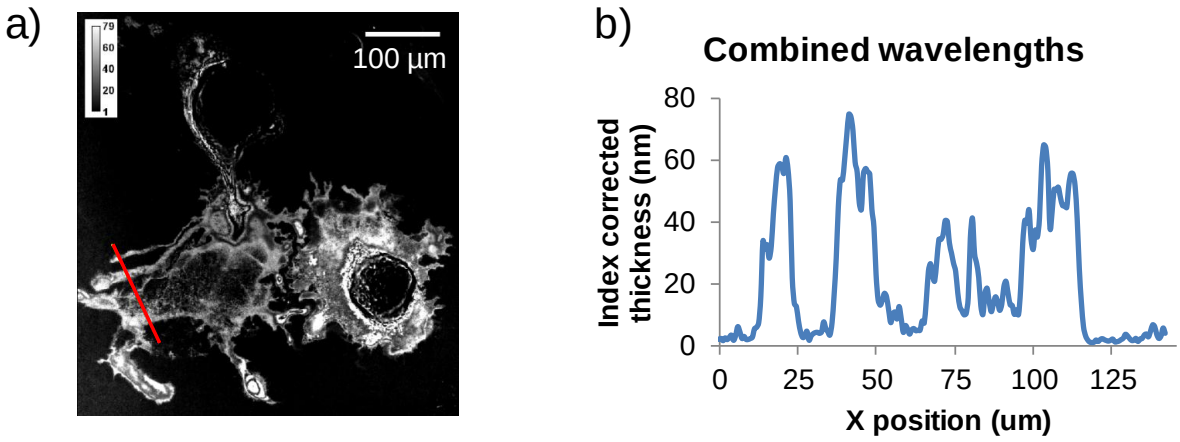

Figure 3.13 a) Wavelength combined (570-600 nm and 570-1000 nm) reflection contrast calibration applied to combined wavelength image of *Aplysia* pedal neuron cultured on a plasmonic crystal surface. b) Height profile along the red line drawn on the image in panel a.

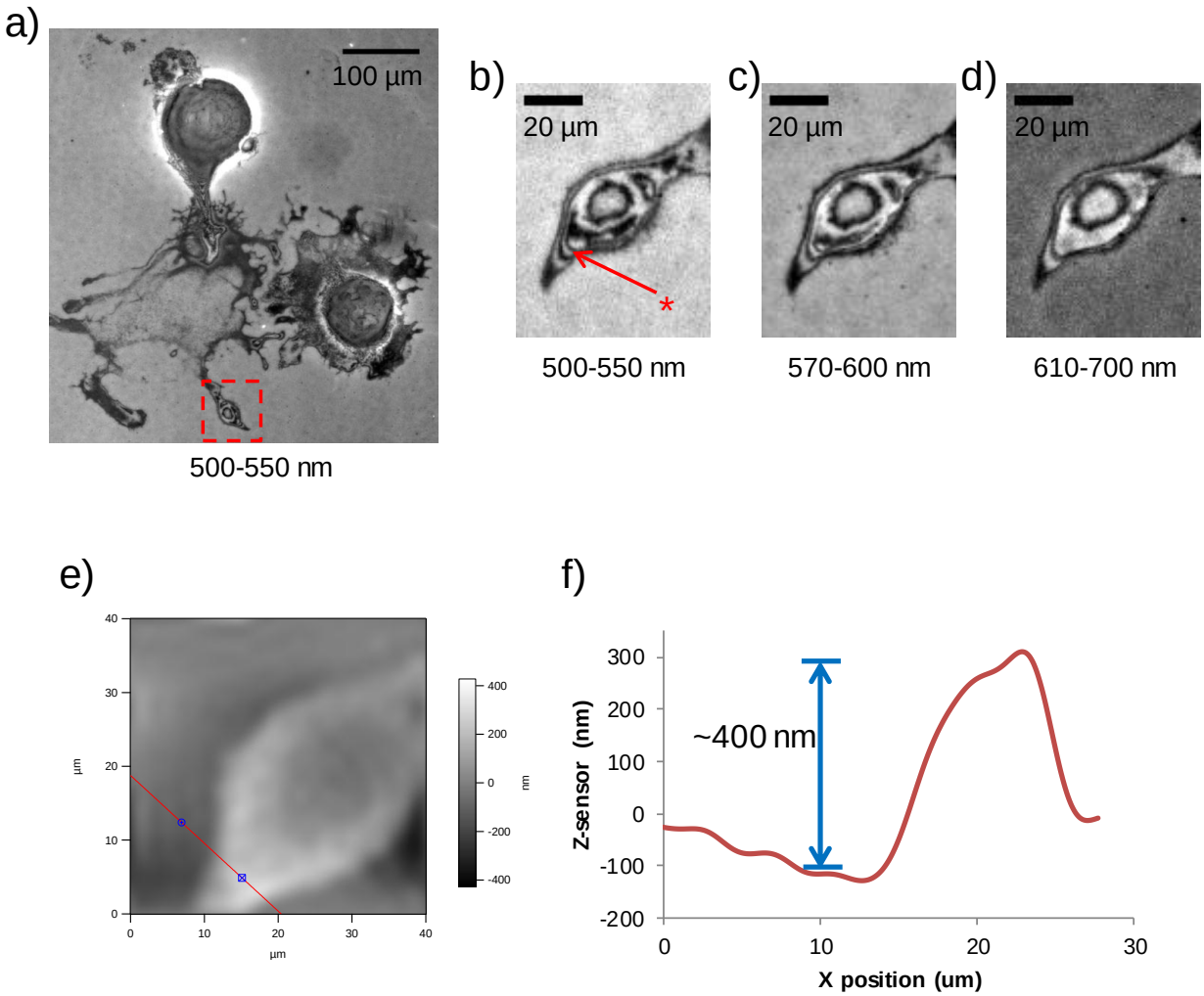

Figure 3.14 a) Reflection image of *Aplysia* pedal neurons cultured on a plasmonic crystal surface acquired using a 500-550 nm bandpass filter. b-d) Rotated and magnified images of the region in the red box in panel a acquired using b) 500-550 nm, c) 570-600 nm, and d) 610-700 nm bandpass filters. Based on thin film interference calculations, the region indicated by the red asterisk in panel b is ~330-400 nm thick. e) FFT filtered AFM image of *Aplysia* pedal neuron feature displayed in panels b-d. f) Height profile along red line drawn on the AFM image in panel e showing good correspondence with thin film interference estimates of structure thickness.

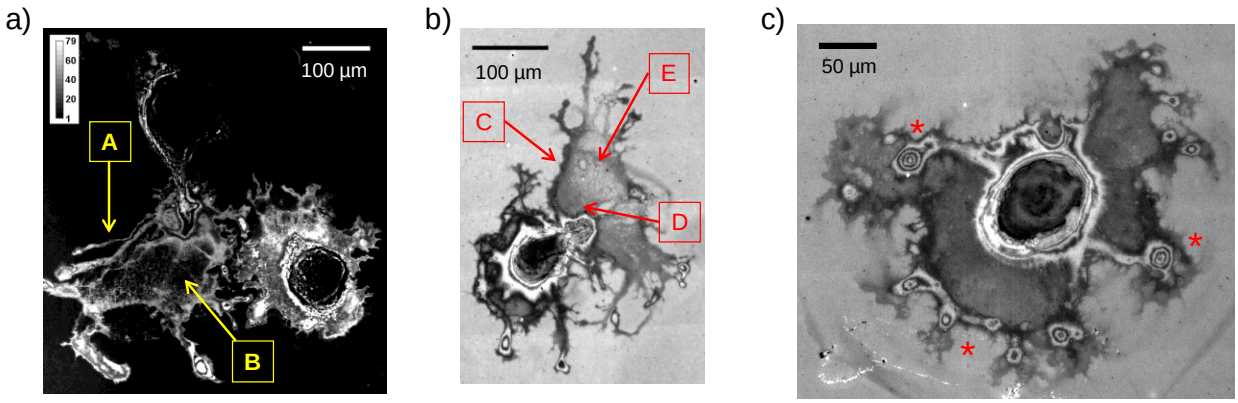

Figure 3.15 a) Thickness calibration applied to combined wavelength (570-600 nm and 570-1000 nm) image of *Aplysia* pedal neurons cultured on plasmonic crystal surface with a neurite ('A') and the remnants of the growth cone peripheral region ('B') indicated. b) Reflection image of an *Aplysia* pedal neuron cultured on a plasmonic crystal surface with a neurite ('C') and the remnants of the growth cone peripheral region ('D' and 'E') indicated. Image was acquired using a 500-550 nm bandpass filter. c) Reflection image of an *Aplysia* pedal neuron cultured on a plasmonic crystal surface acquired using a 500-550 nm bandpass filter. 'Bulls-eye' structures illustrating thin film interference areas potentially corresponding to the central region of the growth cone are denoted with red asterisks and are surrounded by thinner 'veils' corresponding to the peripheral region of the growth cone.

3.8 References

(1) Barry, R. A.; Shepherd, R. F.; Hanson, J. N.; Nuzzo, R. G.; Wiltzius, P.; Lewis, J. A. *Adv. Mater.* **2009**, *21*, 2407.

(2) Millet, L. J.; Stewart, M. E.; Sweedler, J. V.; Nuzzo, R. G.; Gillette, M. U. *Lab on a Chip* **2007**, *7*, 987.

(3) Millet, L. J.; Stewart, M. E.; Nuzzo, R. G.; Gillette, M. U. *Lab on a Chip* **2010**, *10*, 1525.

(4) Zhang, H.; Hanson Shepherd, J. N.; Nuzzo, R. G. *Soft Matter* **2010**, *6*, 2238.

(5) Hanson Shepherd, J. N.; Parker, S. T.; Shepherd, R. F.; Gillette, M. U.; Lewis, J. A.; Nuzzo, R. G. *Adv. Funct. Mater.* **2011**, *21*, 47.

(6) Hanson, J. N.; Motala, M. J.; Heien, M. L.; Gillette, M.; Sweedler, J.; Nuzzo, R. G. *Lab on a Chip* **2009**, *9*, 122.

(7) Corum, L. E.; Eichinger, C. D.; Hsiao, T. W.; Hlady, V. *Langmuir* **2011**, *27*, 8316.

(8) Barty, A.; Nugent, K. A.; Paganin, D.; Roberts, A. *Opt. Lett.* **1998**, *23*, 817.

(9) Allen, R. D.; Allen, N. S.; Travis, J. L. *Cell Motil. Cytoskeleton* **1981**, *1*, 291.

(10) Dodt, H. U.; Zieglgansberger, W. *Brain Res.* **1990**, *537*, 333.

(11) Curtis, A. S. G. *Eur. Cells Mater.* **2001**, *1*, 59.

(12) Pauletti, G.; Dandekar, S.; Rong, H. M.; Ramos, L.; Pong, H. J.; Seshadri, R.; Slamon, D. J. *J. Clin. Oncol.* **2000**, *18*, 3651.

(13) Axelrod, D. *Traffic* **2001**, *2*, 764.

(14) Bezzi, P.; Gundersen, V.; Galbete, J. L.; Seifert, G.; Steinhauser, C.; Pilati, E.; Volterra, A. *Nat. Neurosci.* **2004**, *7*, 613.

(15) Kuwamura, S.; Yamaguchi, I. *Appl. Optics* **1997**, *36*, 4473.

(16) Degroot, P.; Deck, L. *J. Mod. Optic.* **1995**, *42*, 389.

(17) Marquet, P.; Rappaz, B.; Magistretti, P. J.; Cuche, E.; Emery, Y.; Colomb, T.; Depeursinge, C. *Opt. Lett.* **2005**, *30*, 468.

(18) Rotsch, C.; Radmacher, M. *Biophys. J.* **2000**, *78*, 520.

(19) Radmacher, M.; Fritz, M.; Kacher, C. M.; Cleveland, J. P.; Hansma, P. K. *Biophys. J.* **1996**, *70*, 556.

(20) Curtis, M. W.; Russell, B. *Pflugers Arch.* **2011**, *462*, 105.

(21) Homola, J. *Chem. Rev.* **2008**, *108*, 462.

(22) Stewart, M. E.; Anderton, C. R.; Thompson, L. B.; Maria, J.; Gray, S. K.; Rogers, J. A.; Nuzzo, R. G. *Chem. Rev.* **2008**, *108*, 494.

(23) Stewart, M. E.; Mack, N. H.; Malyarchuk, V.; Soares, J. A. N. T.; Lee, T.-W.; Gray, S. K.; Nuzzo, R. G.; Rogers, J. A. *P. Nat. Acad. Sci. USA* **2006**, *103*, 17143.

(24) Jung, L. S.; Campbell, C. T.; Chinowsky, T. M.; Mar, M. N.; Yee, S. S. *Langmuir* **1998**, *14*, 5636.

(25) Homola, J.; Yee, S. S.; Gauglitz, G. *Sens. Actuator B-Chem.* **1999**, *54*, 3.

(26) Johnsson, B.; Lofas, S.; Lindquist, G. *Anal. Biochem.* **1991**, *198*, 268.

(27) Jonsson, U.; Fagerstam, L.; Ivarsson, B.; Johnsson, B.; Karlsson, R.; Lundh, K.; Lofas, S.; Persson, B.; Roos, H.; Ronnberg, I.; Sjolander, S.; Stenberg, E.; Stahlberg, R.; Urbaniczky, C.; Ostlin, H.; Malmqvist, M. *Biotechniques* **1991**, *11*, 620.

(28) Anker, J. N.; Hall, W. P.; Lyandres, O.; Shah, N. C.; Zhao, J.; Van Duyne, R. P. *Nat. Mater.* **2008**, *7*, 442.

(29) Jordan, C. E.; Frutos, A. G.; Thiel, A. J.; Corn, R. M. *Anal. Chem.* **1997**, *69*, 4939.

(30) Aldred, N.; Ekblad, T.; Andersson, O.; Liedberg, B.; Clare, A. S. *ACS Appl. Mater. Interfac.* **2011**, *3*, 2085.

(31) Moh, K. J.; Yuan, X. C.; Bu, J.; Zhu, S. W.; Gao, B. Z. *Opt. Express* **2008**, *16*, 20734.

(32) Argoul, F.; Monier, K.; Roland, T.; Elezgaray, J.; Berguiga, L. In *Biophotonics: Photonic Solutions for Better Health Care II*; 1 ed.; SPIE: Brussels, Belgium, 2010; Vol. 7715, p 771506.

(33) Jamil, M. M. A.; Sefat, F.; Khaghani, S. A.; Lobo, S. B.; Javid, F. A.; Youseffi, M.; Britland, S. T.; Liu, S. G.; See, C. W.; Somekh, M. G.; Denyer, M. C. T. In *4th Kuala Lumpur International Conference on Biomedical Engineering 2008* 2008, p 528.

(34) Lee, H. J.; Nedelkov, D.; Corn, R. M. *Anal. Chem.* **2006**, *78*, 6504.

(35) Malyarchuk, V.; Stewart, M. E.; Nuzzo, R. G.; Rogers, J. A. *Appl. Phys. Lett.* **2007**, *90*, 203113.

(36) Yao, J.; Stewart, M. E.; Maria, J.; Lee, T.-W.; Gray, S. K.; Rogers, J. A.; Nuzzo, R. G. *Angew. Chem. Int. Ed.* **2008**, *47*, 5013.

(37) Stewart, M. E.; Yao, J.; Maria, J.; Gray, S. K.; Rogers, J. A.; Nuzzo, R. G. *Anal. Chem.* **2009**, *81*, 5980.

(38) Truong, T. T.; Maria, J.; Yao, J.; Stewart, M. E.; Lee, T. W.; Gray, S. K.; Nuzzo, R. G.; Rogers, J. A. *Nanotechnology* **2009**, *20*, 434011.

(39) Maria, J.; Truong, T. T.; Yao, J.; Lee, T.-W.; Nuzzo, R. G.; Leyffer, S.; Gray, S. K.; Rogers, J. A. *J. Phys. Chem. C* **2009**, *113*, 10493.

(40) Yao, J.; Le, A.-P.; Schulmerich, M. V.; Maria, J.; Lee, T.-W.; Gray, S. K.; Bhargava, R.; Rogers, J. A.; Nuzzo, R. G. *ACS Nano* **2011**, *Published online*.

(41) Lovell, P.; Moroz, L. L. *Integr. Comp. Biol.* **2006**, *46*, 847.

(42) McPherson, D. R.; Blankenship, J. E. *J. Neurophysiol.* **1992**, *67*, 23.

(43) Steffensen, I.; Dulin, M. F.; Walters, E. T.; Morris, C. E. *J. Exp. Biol.* **1995**, *198*, 2067.

(44) Hua, F.; Sun, Y.; Gaur, A.; Meitl, M. A.; Bilhaut, L.; Rotkina, L.; Wang, J.; Geil, P.; Shim, M.; Rogers, J. A.; Shim, A. *Nano Lett.* **2004**, *4*, 2467.

(45) Caruso, F.; Niikura, K.; Furlong, D. N.; Okahata, Y. *Langmuir* **1997**, *13*, 3422.

(46) Vörös, J. *Biophys. J.* **2004**, *87*, 553.

(47) Benesch, J.; Askendal, A.; Tengvall, P. *J. Colloid Interfac. Sci.* **2002**, *249*, 84.

(48) Ye, X.; Xie, F.; Romanova, E. V.; Rubakhin, S. S.; Sweedler, J. V. *ACS Chem. Neurosci.* **2009**, *1*, 182.

(49) Wang, L. P.; Ota, N.; Romanova, E. V.; Sweedler, J. V. *J. Biol. Chem.* **2011**, *286*, 13765.

(50) Drezek, R.; Dunn, A.; Richards-Kortum, R. *Appl. Opt.* **1999**, *38*, 3651.

(51) *Sony ICX085AL 2/3-inch Progressive Scan CCD Image Sensor with Square Pixel for B/W Cameras*, Datasheet No. E95Z10C73; Sony Corp., http://www.alldatasheet.com/datasheet-pdf/pdf/47409/SONY/ICX085AL.html (accessed June 30, 2010).

(52) Forscher, P.; Kaczmarek, L.; Buchanan, J.; Smith, S. *J. Neurosci.* **1987**, *7*, 3600.

(53) Bamburg, J. R. *J. Histochem. Cytochem.* **2003**, *51*, 407.

(54) Burmeister, D.; Goldberg, D. *J. Neurosci.* **1988**, *8*, 3151.

(55) Kedem, O.; Vaskevich, A.; Rubinstein, I. *J. Phys. Chem. Lett.* **2011**, *2*, 1223.

CHAPTER 4

Future Research Directions for Nanostructured Plasmonic Crystal-Based Sensing and Imaging

The research directions explored in this dissertation and previously reported work demonstrate the versatility of these plasmonic crystal systems as a platform for surface-sensitive imaging and spectroscopy. In fact, the applications detailed in this present work provide starting points for a number of potential derivative projects, some of which are described in this chapter. The ideas proposed broaden the scope of prospective analytical applications by exploiting the advantages of these nanoimprinted plasmonic crystals which have been outlined previously: inexpensive, facile replication of plasmonic structures with nanometer-scale features; high fidelity replication of these plasmonic nanostructures over large areas; and good compatibility with computational simulations for device tuning and optimization.

4.1 Embedded Monitoring Applications for Nanostructured Optical Fiber Probes

Although the detection of adsorbed benzenethiol monolayers and aqueous Rhodamine solutions demonstrated the capacity of these nanostructured optical fibers to enhance Raman scattering in different sensing environments, other analytes are of more practical interest. For example, perchlorate, arsenate, and arsenite are groundwater pollutants of increasing concern, and demonstrations of their detection through SERS has been reported in the literature.[1-4] These nanopatterned optical fibers are particularly well-suited for field monitoring applications: The

small size and physical flexibility of the optical fiber allows them to be threaded into sampling locations that would not accommodate larger instruments, and the silica substrate's stability would allow them to remain in place for extended periods of time. Provided that power could be supplied to the excitation laser and detector, these fiber optic probes are highly amenable to unattended monitoring; the insertion of the probe tip into the body of water being sampled obviates the need for sample collection or preparation. The surfaces of these plasmonic crystals can be readily functionalized to enhance their sensitivity; for example, a cystamine layer can be adsorbed onto the nanostructured metal surface to electrostatically attract negatively charged ions (such as perchlorate, arsenate, and arsenite) to the probe surface, maximizing the achievable Raman scattering.[4]

The incorporation of plasmonic nanostructures on optical fibers also opens possibilities for their integration into a larger biological and chemical ecosystem. A natural extension of these SERS fiber probes would be to interface them with commercially available handheld Raman spectrometers,[5] realizing a truly field-portable analytical system capable of high performance detection. Alternatively, an array of optical fibers embedded in a cell culture plate could be used to monitor changes in the chemical expression of cultured cells tin response to external stimuli; simultaneously multiplexed SERS measurements of these systems could be performed in real time by interfacing the non-patterned fiber ends to a grating-coupled imaging device. Arrays of SERS fiber probes could also be distributed and embedded within environmental systems to provide time-resolved profiles of the migration of chemical species of interest.

4.2 Computational Electrodynamic Modeling of Plasmonic Crystals

The nanohole array structures of our plasmonic crystals support a number of propagating and localized surface plasmon modes, and while analytical expressions exist to describe the propagating surface plasmon polariton modes, a full analytical accounting of the complex optical response is nonexistent. In lieu of this formal description, we have relied on an implementation of the finite-difference time-domain method in order to computationally solve Maxwell's equations, calculating the propagation of electric and magnetic fields through representations of the plasmonic crystal structure.[6-11] This method has proven to be highly effective in replicating the optical properties of these plasmonic structures, and future iterations of plasmonic crystal design will require the theoretical guidance provided by these simulations.

A limitation of our existing FDTD implementation is that it does not account for optical contributions resulting from illumination of the plasmonic crystal at oblique (non-90°) angles, and this has become a greater impediment as the application space for these devices expands to systems which have inherent spreads in the illumination angles. Including this capability in our modeling would provide a more complete theoretical understanding of the plasmonic crystal behavior in the reflection microscopy and SERS fiber systems and could reveal the relative contributions associated with specific illumination angles. These angle-incident simulations could also be verified experimentally using techniques such as darkfield microscopy in which the illumination is explicitly oblique to the surface.

These computational simulations could be used to tune the optical response of the plasmonic crystal by modifying its design rules to maximize the normalized reflection contrast within particular wavelength ranges corresponding to specific bandpass filters available.

Alternatively, these simulations could identify specific wavelength ranges to target in order to achieve the highest contrast possible, and the incorporation of oblique illumination is crucial to adequately characterize the reflection imaging behavior. A particularly intriguing optimization direction would be to maximize the normalized reflection contrast within the wavelength ranges covered by the red, green, and blue imaging pixels of a color digital camera. By exploiting the rudimentary wavelength discrimination from the camera itself, it may be possible to capture multiple wavelength ranges simultaneously without the need for filter changes – the red, green, and blue channels in the images themselves would capture different wavelength-dependent optical responses in a form of hyperspectral imaging that does not require expensive filters or gratings. The individual channels could then be rationally combined, using knowledge of the wavelength-dependent optical response, to generate a composite image with increased contrast and sensitivity in a manner analogous to the methods developed in this work.

4.3 Simulation-Driven Plasmonic Crystal Design for SERS

The Raman scattering enhancement of a plasmonic substrate has been correlated with the wavelength of a supported localized surface plasmon mode, and a maximum enhancement is achieved when the wavelength of the localized surface plasmon falls halfway between the excitation wavelength and the absolute wavelength of the Raman scattered photon.[12,13] The presence of the LSPR mode halfway between the excitation and scattering wavelengths is believed to result in a moderate enhancement in the coupling of light into and out of the analyte. While the LSPR could be centered at one of the wavelengths (either the excitation or the scattering wavelength) to maximize the enhancement of that process, empirical results indicate

that this ultimately results in a lower overall Raman enhancement – a moderate enhancement of both processes is preferable to a large enhancement of only one.

While much of this work has been performed for nanoparticle-based systems, analogous behavior has been observed in plasmonic crystal systems where the transmission at this half-wavelength of merit is positively correlated with the relative Raman enhancement.[11,14,15] While nanoparticles can (generally) only support one LSPR mode, these plasmonic crystals can support several different plasmonic modes (both propagating and localized), and it would be advantageous to tune the optical response (and thus the Raman enhancement) by optimizing the design rules of the device to maximize this metric (the spectral transmission at this 'half-wavelength' of merit). Regardless of the fabrication method, physically producing specific nanoarchitectures can be time consuming and expensive, but computational simulations offer a route for predicting the optical properties (and thus indirectly predict the relative SERS enhancements) of the modified plasmonic crystals *in silico*, avoiding the costly nanofabrication of intermediate design iterations.

These simulations can also inform efforts to maximize SERS performance by illustrating the nature of the electric fields at both the excitation and the scattering wavelengths and revealing regions on the nanohole array where the electric field intensities are highest. It stands to reason that analytes present in areas of high electric field intensity for both processes will experience the greatest Raman enhancement, and this understanding can be exploited to design plasmonic crystal sensors such that the analytes are localized in the same regions as these electric field maxima.

For example, simulations suggest that the electric field intensities for spin-on-glass-based plasmonic crystals at both the excitation (785 nm) and scattering wavelengths (857 nm for the

benzenethiol scattering peak at ~1070 cm^{-1}) are localized around the rim of the nanohole, with little electric field intensity across the majority of the gold surface. (Depictions of these electric fields calculated using our FDTD method are presented in Figure 4.1a and Figure 4.1b.) Additionally, the product of these electric fields (displayed in Figure 4.1c) reveal that the regions of maximum overlap between these high electric field intensities are also localized around the nanohole rim. This modeling suggests that analyte molecules found in other areas of the plasmonic crystal are unlikely to experience large Raman enhancements. This finding could be verified experimentally by comparing the relative Raman scattering intensities for benzenethiol adsorbed on a plasmonic crystal as previously described and for benzenethiol adsorbed on a plasmonic crystal modified to prevent adsorption of the analyte in low-sensitivity areas; directional evaporation of a thin dielectric film (such as SiO_2) could block the gold surface while leaving the nanohole rim free for the adsorption of benzenethiol. Furthermore, this electric field localization could be exploited indirectly by first filling the nanoholes with silica nanospheres to which antibodies have been immobilized. These antibodies could effectively trap analytes near the nanohole rim (and the higher electric field intensities), resulting in increased Raman enhancement and sensitivity.

4.4 Live Cell Imaging on Plasmonic Crystals

The quantitation performance and image acquisition speed demonstrated in the cell imaging performed as a part of this dissertation strongly suggests an ability to perform similar imaging measurements on live cells. While additional efforts will be required in order to adapt this reflection imaging protocol for live cell imaging, the protocol itself would be expected to remain largely the same. The work performed in this dissertation utilized an upright optical

microscope with the plasmonic crystal surface turned upside-down in order to image the surface from the opposite side; this is clearly undesirable for imaging live cell cultures. Thus, an inverted microscope is needed, along with a camera and the ability to place bandpass filters in the optical train. Higher spatial resolution, accomplished by using a higher magnification objective, would be desirable to monitor the dynamics of cell growth at the periphery. These changes would necessitate new calibrations for polyelectrolyte layers (or other suitable thin films of controlled thickness) in water to better mimic the refractive index of the cell culture medium. The image analysis protocols themselves, however, would remain unchanged.

One area for concern is a marked drop in refractive index contrast when imaging live cells (surrounding $n \sim 1.3$) as compared to the fixed cell systems (surrounding $n \sim 1.0$) explored in this work. While the refractive index of hydrated cell materials are expected to be much closer to those of the aqueous surroundings, previous investigations of the refractive index sensitivity of transmission-based spectroscopic measurements demonstrate a sensitivity to refractive index changes on the order of 1×10^{-3} refractive index units,[6,9] which would be sufficient to differentiate the cell cytoplasm and membranes from the surrounding aqueous medium.

4.5 Label-free Chemical Imaging of Live Cells on Hydrogel-Modified Plasmonic Crystals

While the plasmonic reflection imaging technique demonstrated in this dissertation showed exceptional capabilities for quantitative thickness measurements on the plasmonic crystal surface, surface plasmon resonance methods in general are limited by their sensitivity only to refractive index – they provide no other chemically specific information, although secondary mechanisms for providing chemical selectivity or specificity (such as the inclusion of

antibodies or DNA aptamers) can be engineered into the sensor's design. An additional limitation encountered in the imaging of cultured cells is the extent to which the *Aplysia* neuron's outgrowth conformed to the nanohole relief structure – it is known that a certain level of control can be exerted over a neuron's outgrowth by the topography of the cultured surface.

A potential method for addressing both of these issues is to functionalize the plasmonic crystal surface with a pH-sensitive hydrogel. Such a functionalization was performed previously using these plasmonic crystal systems in order to measure pH changes in a bulk solution, and pH changes as small as 0.1 pH units could be readily detected.[16] The hydrogel itself could be used to infill the plasmonic nanoholes, effectively planarizing the surface and reducing its potential impact on the outgrowth behavior of the cultured cells. In addition, acrylic acid moieties could be incorporated into the hydrogel as in that previous work to render it sensitive to changes in the local pH. Changes of pH within the cultured cell's microenvironment would result in swelling or deswelling of the hydrogel in those same areas, and this swelling behavior would be detected as a change in reflection intensity relative to a reference image chosen from inside the image. This behavior could be observed in near real time thanks to the rapid imaging capabilities using these plasmonic crystals, and these observations would be possible without the need for external labels (such as fluorophores).

Extending this idea further, the pH sensitive hydrogel itself could be functionalized further with enzymes whose reactions result in a change in pH. For example, a redox hydrogel system sensitive to glutamate has been implemented for electrochemical studies of neurotransmitter secretion, and the glutamate oxidase and horseradish peroxidase enzymes incorporated as part of the hydrogel consume protons during the course of the reaction.[17,18] The secretion of glutamate could then be detected indirectly as a local change in pH (as protons are

consumed) with the associated swelling or deswelling of the hydrogel. The coupling of this enzyme augmented hydrogels to nanostructured plasmonic crystals could very well provide an inexpensive method for detailed, label-free chemical imaging of cellular secretion events across the entire cell.

4.6 Final Remarks

The work described in this dissertation has explored applications of nanostructured plasmonic crystals for surface-enhanced Raman spectroscopy as well as for surface plasmon resonance imaging, demonstrating the versatility of this single, common sensing platform. The underlying surface plasmon phenomena and their associated electric fields are associated with other surface-enhanced analytical methods, such as metal-enhanced fluorescence, surface-enhanced infrared absorption spectroscopy, and surface-enhanced mass spectrometry. The cost advantages and inherent tunability of these nanoimprinted plasmonic crystals make them well suited for incorporation throughout the broader landscape of surface-enhanced (and surface-sensitive) sensing.

The applications investigated in this dissertation and the research ideas proposed in this chapter are certainly not an exhaustive listing of the potential applications for plasmonic crystals, but they do seek to broaden and enhance the utility of these devices for high performance chemical sensing and imaging in directions which preserve the cost and fabrication advantages of soft nanoimprint lithography as a fabrication method. To this end, these research directions use basic laboratory instrumentation to perform analyses capable of performance on a par with alternate methods and instrumentation which would cost an order of magnitude higher. This

versatile sensing platform heralds a significant advance towards next-generation chemical sensing and imaging which is truly available to the masses.

4.7 Figures

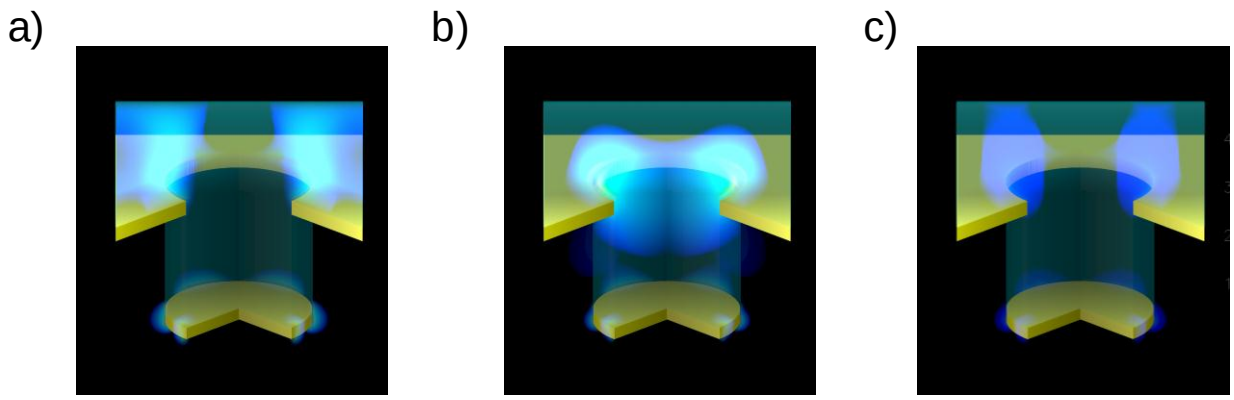

Figure 4.1 a) and b) Electric field distributions for a spin-on-glass based plasmonic crystal at the excitation wavelength (785 nm, panel a) and at the Raman scattered wavelength (857 nm for the benzenethiol Raman peak at ~1070 cm^{-1}, panel b). c) Resulting electric fields calculated by a point-by-point multiplication of the electric fields shown in panels a and b showing regions of maximum electric field intensity overlap localized around the nanohole edge.

4.8 References

(1) Han, M. J.; Hao, J. M.; Xu, Z. H.; Meng, X. G. *Anal. Chim. Acta* **2011**, *692*, 96.

(2) Xu, Z.; Hao, J.; Li, F.; Meng, X. *J. Colloid Interfac. Sci.* **2010**, *347*, 90.

(3) Gu, B.; Ruan, C.; Wang, W. *Appl. Spectrosc.* **2009**, *63*, 98.

(4) Ruan, C.; Wang, W.; Gu, B. *Anal. Chim. Acta* **2006**, *567*, 114.

(5) Lieber, C. A.; Mahadevan-Jansen, A. *Opt. Express* **2007**, *15*, 11874.

(6) Stewart, M. E.; Mack, N. H.; Malyarchuk, V.; Soares, J. A. N. T.; Lee, T.-W.; Gray, S. K.; Nuzzo, R. G.; Rogers, J. A. *P. Nat. Acad. Sci. USA* **2006**, *103*, 17143.

(7) Stewart, M. E.; Yao, J.; Maria, J.; Gray, S. K.; Rogers, J. A.; Nuzzo, R. G. *Anal. Chem.* **2009**, *81*, 5980.

(8) Truong, T. T.; Maria, J.; Yao, J.; Stewart, M. E.; Lee, T. W.; Gray, S. K.; Nuzzo, R. G.; Rogers, J. A. *Nanotechnology* **2009**, *20*, 434011.

(9) Yao, J.; Stewart, M. E.; Maria, J.; Lee, T.-W.; Gray, S. K.; Rogers, J. A.; Nuzzo, R. G. *Angew. Chem. Int. Ed.* **2008**, *47*, 5013.

(10) Maria, J.; Truong, T. T.; Yao, J.; Lee, T.-W.; Nuzzo, R. G.; Leyffer, S.; Gray, S. K.; Rogers, J. A. *J. Phys. Chem. C* **2009**, *113*, 10493.

(11) Yao, J.; Le, A.-P.; Schulmerich, M. V.; Maria, J.; Lee, T.-W.; Gray, S. K.; Bhargava, R.; Rogers, J. A.; Nuzzo, R. G. *ACS Nano* **2011**, *Published online*.

(12) McFarland, A. D.; Young, M. A.; Dieringer, J. A.; Van Duyne, R. P. *J. Phys. Chem. B* **2005**, *109*, 11279.

(13) Haynes, C. L.; Van Duyne, R. P. *J. Phys. Chem. B* **2003**, *107*, 7426.

(14) Baca, A. J.; Truong, T. T.; Cambrea, L. R.; Montgomery, J. M.; Gray, S. K.; Abdula, D.; Banks, T. R.; Yao, J.; Nuzzo, R. G.; Rogers, J. A. *Appl. Phys. Lett.* **2009**, *94*, 243109.

(15) Baca, A. J.; Montgomery, J. M.; Cambrea, L. R.; Moran, M.; Johnson, L.; Yacoub, J.; Truong, T. T. *J. Phys. Chem. C* **2011**, *115*, 7171.

(16) Mack, N. H.; Wackerly, J. W.; Malyarchuk, V.; Rogers, J. A.; Moore, J. S.; Nuzzo, R. G. *Nano Lett.* **2007**, *7*, 733.

(17) Oldenziel, W. H.; Dijkstra, G.; Cremers, T. I. F. H.; Westerink, B. H. C. *Anal. Chem.* **2006**, *78*, 3366.

(18) Belay, A.; Collins, A.; Ruzgas, T.; Kissinger, P. T.; Gorton, L.; Csoregi, E. *J. Pharm. Biomed. Anal.* **1999**, *19*, 93.

Author's Biography

An-Phong Le was born in Belleville, Illinois on April 27, 1982 and was raised in Waterloo, Illinois, graduating from Waterloo High School in 2000. He received his bachelor's degree in chemical engineering from the University of Illinois at Urbana-Champaign in 2004, and during his undergraduate studies, he completed summer internships at General Mills, Inc. in Minneapolis, Minnesota and at the Procter and Gamble Co. in Cincinnati, Ohio. He also worked as a teaching assistant during his junior and senior years for the accelerated general chemistry courses at the University of Illinois under Prof. Steven S. Zumdahl, Prof. Paul B. Kelter, and Dr. Donald J. DeCoste.

These teaching experiences led him to remain at the University of Illinois at Urbana-Champaign to pursue a Ph.D. specializing in analytical chemistry and chemical education. As part of his chemical education experiences, An-Phong was the course lecturer for one section of introductory chemistry and one section of general chemistry, course coordinator for the mainstream general chemistry laboratories, and chemistry lecturer for the Bridge-Transition Program. He also worked as a curriculum developer and research assistant for the Institute for Chemistry Literacy through Computational Science, a research program funded by the National Science Foundation to introduce high school chemistry teachers to computational tools which could be adapted for use in the classroom. Additionally, he surveyed general chemistry students with Dr. Donald DeCoste and Jordan Beck to track how students' conceptions of chemistry topics evolved as they completed additional formal coursework.

Under the guidance of Profs. Ralph Nuzzo and John Rogers, An-Phong explored analytical applications for a class of nanoimprinted plasmonic crystals. He adapted a soft

embossing method to pattern these plasmonic crystal surfaces onto the tips of multimode optical fibers for use as probes for surface-enhanced Raman scattering. He also developed imaging and analysis protocols to derive quantitative three-dimensional topography from reflection images of thin films and cellular outgrowths on plasmonic crystal surfaces.

After receiving his Ph.D. in 2011, An-Phong will join the faculty at Florida Southern College in Lakeland, Florida as an assistant professor of chemistry, pursuing research interests in chemical education and curriculum design, plasmonic sensing and imaging, and paper-based microfluidic devices for environmental sampling and monitoring.